Aus dem Institut für Prophylaxe und Epidemiologie
der Kreislaufkrankheiten (IPEK)
Klinik der Universität München
Direktor: Prof. Dr. Christian Weber

Role of the G protein-coupled receptor 55 in the pathogenesis of atherosclerosis

Dissertation
zum Erwerb des Doktorgrades der Medizin
an der Medizinischen Fakultät der
Ludwig-Maximilians-Universität zu München

vorgelegt von

Daniel Uwe Hering

aus Kronach

2023

Mit Genehmigung der Medizinischen Fakultät
der Universität München

Berichterstatter:	Prof. Dr. Sabine Steffens
Mitberichterstatter:	Prof. Dr. Jürgen Bernhagen
	Prof. Dr. M. Mederos y Schnitzler
	PD Dr. Andreas Herbst
Mitbetreuung durch den promovierten Mitarbeiter:	Dr. Raquel Guillamat-Prats (PhD)
Dekan:	Prof. Dr. Thomas Gudermann
Tag der mündlichen Prüfung:	04.05.2023

Eidesstattliche Versicherung

Hering, Daniel

Name, Vorname

Ich erkläre hiermit an Eides statt, dass ich die vorliegende Dissertation mit dem Titel:

Role of the G protein-coupled receptor 55 in the pathogenesis of atherosclerosis

selbstständig verfasst, mich außer der angegebenen keiner weiteren Hilfsmittel bedient, und alle Erkenntnisse, die aus dem Schrifttum ganz oder annähernd übernommen sind, als solche kenntlich gemacht und nach ihrer Herkunft unter Bezeichnung der Fundstelle einzeln nachgewiesen habe.

Ich erkläre des Weiteren, dass die hier vorgelegte Dissertation nicht in gleicher oder in ähnlicher Form bei einer anderen Stelle zur Erlangung eines akademischen Grades eingereicht wurde.

München, 15.05.2023

Ort, Datum

Daniel Hering

Unterschrift Doktorand

The results of this work were partly published in:

Raquel Guillamat-Prats, Daniel Hering, Abhishek Derle, Martina Rami, Carmen Härdtner, Donato Santovito, Petteri Rinne, Laura Bindila, Michael Hristov, Sabrina Pagano, Nicolas Vuilleumier, Sofie Schmid, Aleksandar Janjic, Wolfgang Enard, Christian Weber, Lars Maegdefessel, Alexander Faussner, Ingo Hilgendorf, Sabine Steffens. *GPR55 in B cells limits atherosclerosis development and regulates plasma cell maturation* Nature Cardiovascular Research 2022 Nov;1:1056-1071

Raquel Guillamat-Prats, Daniel Hering, Martina Rami, Carmen Härdtner, Donato Santovito, Petteri Rinne, Laura Bindila, Michael Hristov, Sabrina Pagano, Nicolas Vuilleumier, Sofie Schmid, Aleksandar Janjic, Wolfgang Enard, Christian Weber, Lars Maegdefessel, Alexander Faussner, Ingo Hilgendorf, Sabine Steffens. *GPR55 in B cells limits atherosclerosis development and regulates plasma cell maturation* (bioRxiv 2021.12.20.473518; doi: https://doi.org/10.1101/2021.12.20.473518, 2021)

The results of this work were presented at the following conferences:

Oral presentations

13.-14.09.2017	**4th Young DZHK Retreat**, Rostock-Warnemünde, Germany Title: Cannabinoid receptor GPR55 deficiency promotes atherosclerosis in mice

Poster presentations

10.-12.05.2018	Arteriosclerosis, Thrombosis, and Vascular Biology – **Vascular Discovery: From Genes to Medicine Scientific Sessions 2018**, San Francisco, USA Title: G protein Coupled Receptor 55 Deficiency Promotes Atherosclerosis and Inflammation in Mice
05.-08.05.2018	European Atherosclerosis Society – **EAS Congress 2018**, Lisbon, Portugal Title: G-Protein Coupled Receptor 55 Deficiency Promotes Atherosclerosis and Inflammation in Mice Presenter: Prof. Dr. rer. nat. Sabine Steffens
12.-14.10.2017	Deutsche Gesellschaft für Kardiologie – Herz- und Kreislaufforschung, **DGK Herztage**, Berlin, Germany Title: Cannabinoid receptor GPR55 deficiency promotes atherosclerosis in mice
03.07.2017	Munich Heart Alliance – **Summer Meeting 2017**, Bernried am Starnberger See, Germany Title: GPR55 deficiency promotes atherosclerosis development in mice

TABLE OF CONTENTS

LIST OF FIGURES

LIST OF TABLES

LIST OF ABBREVIATIONS

-/-	Homozygous gene knockout
1-SG	1-Stearoylglycerol
2-AG	2-Arachidonoylglycerol
Abca1	Murine ATP-binding cassette transporter A1 gene
Abcg1	Murine ATP-binding cassette G1 gene
ACS	Acute coronary syndrome
AF	AlexaFluor
AGPAT8	1-acylglycerol-3-phosphate acyltransferase 8
ALCAT1	Acyl-CoA:lysocardiolipin acyltransferase 1
ANOVA	Analysis of variance
APC	Allophycocyanin
APC/Cy7	Tandem dye allophycocyanin plus cyanine
Apoe	Apolipoprotein E
Arg1	Murine arginase 1 gene
ATF-2	Activating transcription factor 2
BAFF	B-cell activating factor
BCR	B-cell receptor
BKCa	Large-conductance Ca^{2+}- and voltage-gated big K^{+} channel
BMDM	Bone marrow-derived macrophages
BSA	Bovine serum albumin
BV	Brilliant Violet
cAMP	Cyclic adenosine monophosphate
CB1	Cannabinoid receptor 1
CB2	Cannabinoid receptor 2
CBD	Cannabidiol
CCL	Chemokine (C-C motif) ligand
CCR	Chemokine (C-C motif) receptor
CD	Cluster of differentiation
Cdc42	Cell division control protein 42 homolog
cDNA	Complementary DNA
Conc.	Concentration
CREB	cAMP responsive element binding protein 1
CVD	Cardiovascular disease
CX_3CR	Chemokine (C-X3-C motif) receptor
CXCL	Chemokine (C-X-C motif) ligand
CXCR	Chemokine (C-X-C motif) receptor
Cyp7a	Murine cytochrome P450 7A1 (cholesterol 7 alpha-hydroxylase) gene
DC	Dendritic cell
DDHD1	DDHD domain-containing protein 1
Dhcr7	Murine 7-Dehydrocholesterol reductase gene
DMEM	Dulbecco's modified eagle medium

DMSO	Dimethylsulfoxid
DNA	Deoxyribonucleic acid
EC	Endothelial cell
ECM	Extracellular matrix
EDTA	Ethylenediaminetetraacetic acid
ER	Endoplasmatic reticulum
ERK	Extracellular signal-regulated kinase
EST	Expressed Sequence Tags
ETV4	ETS variant transcription factor 4
FACS	Fluorescence-activated cell sorting
FBS	Fetal bovine serum
FITC	Fluorescein isothiocyanate
FO B cell	Follicular B cell
Fwd	Forward
Gapdh	Murine glyceraldehyde 3-phosphate dehydrogenase gene
gDNA	Genomic DNA
GDP	Guanosine diphosphate
GEF	Guanine-nucleotide exchange factor
GM-CSF	Granulocyte-macrophage colony-stimulating factor
GPCR	G protein-coupled receptor
GPI	Glycerophosphoinositol
GPR	G protein-coupled receptor
GTP	Guanosine triphosphate
HBSS	Hank's balanced salt solution
HDL	High density lipoprotein
HEK	Human embryonic kidney
HEPES	4-(2-hydroxyethyl)-1-piperazineethanesulfonic acid
HFD	High fat diet
Hmgcr	Murine 2-hydroxyl-3-methyl-glutaryl-coenzyme A reductase, HMG-CoA reductase gene
Hprt	Murine hypoxanthine-guanine phosphoribosyltransferase gene
HSC	Hematopoietic stem cell
ICAM1	Intracellular adhesion molecule 1
IEL	Internal elastic lamina
IFN-γ	Interferon gamma
Ig	Immunoglobulin
IL	Interleukin
Inos	Murine inducible nitric oxide synthase gene
IP_3	Inositol 1,4,5-triphosphate
IRA B cell	Innate response activator B cell
KCNK2/TREK-1	Potassium channel subfamily K member 2
KCNK4/TRAAK	Potassium channel subfamily K member 4
LDH	Lactate dehydrogenase

LDL	Low-density lipoprotein
Ldlr	Murine low-density lipoprotein receptor gene
LPA	Lysophosphatidic acid
LPI	Lysophosphatidylinositol
LPIAT1	LPI acyltransferase 1
Ly6C	Lymphocyte antigen 6 complex
MACS	Magnetic cell separation
MAPK	Mitogen-activated protein kinase
MBOAT7	Membrane-bound O-acyltransferase domain-containing 7
M-CSF	Macrophage colony-stimulating factor
MFI	Mean fluorescence intensity
MHC-I/II	Major histocompatibility complex I/II
MMP	Matrix metalloproteinase
MPO	Myeloperoxidase
mRNA	Messenger ribonucleic acid
MSC	Mesenchymal stem cell
MZ B cells	Marginal zone B cells
NET	Neutrophil extracellular trap
NFAT	Nuclear factor of activated T cells
NF-κB	Nuclear factor kappa-light-chain-enhancer of activated B cell
NGF	Nerve growth factor
NK cells	Natural killer cells
NKT cells	Natural killer T cells
ORO	Oil red O
OxLDL	Oxidized low-density lipoprotein
PA	Phosphatidic acid
PA-PLA1	Phosphatidic acid-preferring phospholipase A1
PB	Pacific Blue
PBS	Phosphate buffered saline
PCR	Polymerase chain reaction
pDC	Plasmacytoid dendritic cell
PE	Phycoerythrin
PE/Cy7	Tandem dye Phycoerythrin plus cyanine
PEA	Palmitoylethanolamide
PerCP	Peridinin chlorophyll
PI	Phosphatidylinositol
PLA	Phospholipase A
PLC	Phospholipase C
PLD	Phospholipase D
qPCR	Quantitative real-time polymerase chain reaction
Rac1	Ras-related C3 botulinum toxin substrate 1
Rev	Reverse
RhoA	Ras homolog family member A

ROCK	Rho-associated protein kinase
ROS	Reactive oxygen species
RPMI	Roswell Park Memorial Institute
RT	Reverse transcription
SEM	Standard error of the mean
SMC	Smooth muscle cell
SR-A1	Scavenger receptor class A type 1
SR-B1	Scavenger receptor class B type 1
T2DM	Type 2 diabetes mellitus
TAE	Tris-acetate-EDTA
TCR	T-cell receptor
TGF-β	Transforming growth factor β
$T_H1/2$	Type 1/2 T helper cell
TLR2	Toll-like receptor 2
TNF-α	Tumor necrosis factor α
T_{reg}	Regulatory T cell
TRPM8	Transient receptor potential cation channel subfamily M (melastatin) member 8
TRPV2	Transient receptor potential cation channel subfamily V member 2
VCAM1	Vascular adhesion molecule 1
VLDL	Very-low-density lipoprotein
VSMC	Vascular smooth muscle cells
WD	Western diet
WT	Wild type
γδ TCR	Gamma delta T-cell receptor
Δ^9-THC	Delta-9-tetrahydrocannabinol

1 SUMMARY

Atherosclerosis is a chronic inflammatory disease of the arterial wall and is the main pathophysiological mechanism for the development of cardiovascular diseases. These represent the leading cause of death worldwide. Atherosclerosis manifests clinically, for example, as heart attack, stroke or peripheral artery disease. Despite decades of research, treatment options for atherosclerosis are still limited. Therefore, new treatment and prevention strategies are urgently required. To develop these, it is crucial to analyze and understand the underlying pathophysiological processes of inflammatory cell functions involved in plaque development.

The G protein-coupled receptor 55 (GPR55) is expressed in numerous tissues and on immune cells such as monocytes, B cells, neutrophils and NK cells in humans and mice. Its endogenous ligand is the phospholipid lysophosphatidylinositol (LPI). So far, its role in the pathogenesis of atherosclerosis remains elusive.

This thesis aimed to investigate the role of GPR55 during the onset and progression of atherosclerosis in a mouse model. For this reason, mice with a global *Gpr55* knockout were crossed with atherosclerosis-prone apolipoprotein E-deficient (*Apoe*$^{-/-}$) mice to generate *Apoe*$^{-/-}$*Gpr55*$^{-/-}$ double knockout mice. The development of atherosclerotic lesions was induced by treatment with a high-fat and high-cholesterol diet (Western Diet, WD) and results were compared to *Apoe*$^{-/-}$ control animals. For this purpose, two different stages of the disease were selected. Mice were examined after 4 and 16 weeks of WD feeding, respectively.

Inducing hypercholesterolemia by feeding the WD activated the LPI/GPR55 axis in *Apoe*$^{-/-}$ mice during early atherogenesis and led to increased expression of a key enzyme of the LPI biosynthesis. Thus, regulation of GPR55 and its ligand LPI was shown during the formation of early atherosclerotic plaques. Based on these initial results, we speculated that GPR55 has its greatest impact during early atherogenesis.

Histological analyzes of the atherosclerotic plaques confirmed our assumptions. *Apoe*$^{-/-}$ mice lacking a functional GPR55 receptor showed larger aortic root plaques with a significantly higher ratio of macrophages than in the control animals. At the same time, the number of monocytes in the bone marrow of these animals was massively elevated compared to *Apoe*$^{-/-}$ controls. In addition, an increased uptake of oxidized LDL particles (oxLDL) by cultured bone marrow derived macrophages of *Apoe*$^{-/-}$*Gpr55*$^{-/-}$ animals could be demonstrated *in vitro*. During this stage of the disease we also found a substantially altered lipid metabolism in the liver. Gene expression of key enzymes required for cholesterol synthesis and cholesterol transport was significantly upregulated.

Differences in lesion composition were also observed at the later time of disease after 16 weeks of WD feeding. Atherosclerotic lesions in *Apoe*$^{-/-}$*Gpr55*$^{-/-}$ mice presented with features of more advanced plaques with higher collagen content and

larger necrotic cores. Analysis of female aortas illustrated a higher plaque burden in *Apoe*$^{-/-}$*Gpr55*$^{-/-}$ as well.

Different leukocyte subpopulations were affected by the complete loss of GPR55. The aortas of *Apoe*$^{-/-}$*Gpr55*$^{-/-}$ mice showed more lymphocytes and neutrophils during early atherosclerosis and upregulation of pro-inflammatory genes in the vessels harvested after 16 weeks of WD. This indicates an exacerbated inflammatory response in this tissue. Compared to the control group, there were also higher numbers of T and B cells in the blood of the female *Apoe*$^{-/-}$*Gpr55*$^{-/-}$ animals. Lymphoid tissues such as spleen and lymph nodes also contained more B and T cells than *Apoe*$^{-/-}$ controls in the later stages of the disease. However, we saw the most notable differences in B cells. In lymphatic tissues, the subpopulations were shifted towards proinflammatory marginal zones B2 cells and changes in the relative B1 populations were also observed. The *Gpr55* knockout led to an overproduction of mainly immunoglobulin G (IgG) antibodies. It appears that GPR55 affects both the adaptive immune system and parts of the innate immune response in the context of atherosclerosis, with a general anti-inflammatory effect on these cells.

This work describes a substantial influence of GPR55 on the development of atherosclerosis and the proatherosclerotic consequences of the *Gpr55* knockout. Overall, the receptor seems to play a protective role. The GPR55/LPI signaling cascade may play a central role in the regulation of various leukocytes involved in atherosclerosis. We could demonstrate an effect on neutrophils, monocytes, macrophages, T-cells, B-cells and antibodies in the serum. In the future, the function of GPR55 in different cell populations and the pharmacological manipulation of the receptor should be further investigated in order to possibly reduce the inflammatory processes associated with atherosclerosis.

2 ZUSAMMENFASSUNG

Atherosklerose ist eine chronisch entzündliche Erkrankung der Arterienwand. Vor allem aber ist sie der wichtigste pathophysiologische Mechanismus für die Entwicklung von Herz-Kreislauf-Erkrankungen, welche die weltweit häufigste Todesursache darstellen. Sie manifestiert sich beispielsweise in den Krankheitsbildern Herzinfarkt, Schlaganfall oder der peripheren arteriellen Verschlusskrankheit. Trotz jahrzehntelanger Forschung sind die Behandlungsmöglichkeiten der Atherosklerose noch immer begrenzt und neue Therapie- und Präventionsstrategien deshalb dringend erforderlich. Um diese zu entwickeln, ist es entscheidend, die zugrunde liegenden pathophysiologischen Prozesse der Entzündungszellen zu analysieren und zu verstehen, die an der Plaque-Entwicklung beteiligt sind.

Der G-Protein-gekoppelte Rezeptor 55 (GPR55) wird von zahlreichen Geweben und auf Immunzellen wie Monozyten, B-Zellen, Neutrophilen und NK-Zellen bei Menschen und Mäusen exprimiert. Sein natürlicher Ligand ist das Phospholipid Lysophosphatidylinositol (LPI). Bisher wurde seine Rolle in der Pathogenese der Atherosklerose kaum untersucht.

Das Ziel dieser Arbeit war es, den Einfluss von GPR55 auf die Entstehung atherosklerotischer Plaques in einem Mausmodell zu untersuchen. Aus diesem Grund wurden Mäuse mit einem globalen GPR55-Knockout mit atherskleroseempfindlichen Apolipoprotein E-defizienten (*Apoe*$^{-/-}$) Mäusen gekreuzt, um *Apoe*$^{-/-}$*Gpr55*$^{-/-}$ Doppel-Knockout-Mäuse zu erzeugen. Die Entwicklung atherosklerotischer Läsionen haben wir durch Behandlung mit einer fett- und cholesterinreichen Diät (Western Diet, WD) induziert und zu zwei verschiedenen Zeitpunkten, nach 4 beziehungsweise 16 Wochen WD-Fütterung, mit *Apoe*$^{-/-}$ Kontrolltieren verglichen.

Die durch Fütterung der WD verursachte Hypercholesterinämie aktivierte die LPI/GPR55-Achse in *Apoe*$^{-/-}$-Mäusen im frühen Stadium der Atherosklerose und führte ebenfalls zu einer vermehrten Expression eines Schlüsselenzyms der LPI-Biosynthese. Es konnte also eine Regulation von GPR55 und seinem Liganden LPI während der Entstehung früher atherosklerotischer Plaques beobachtet werden. Basierend auf diesen ersten Ergebnissen gelangten wir zu der Annahme, dass GPR55 seinen größten Einfluss im frühen Stadium der Atherogenese nimmt.

Histologische Analysen der atherosklerotischen Plaques bestätigten unsere Hypothese. *Apoe*$^{-/-}$ Mäuse ohne funktionsfähigen GPR55-Rezeptor zeigten größere atherosklerotische Läsionen in den Aortenwurzeln mit einem markant höheren Anteil an Makrophagen als bei den Kontrolltieren. Parallel dazu war der Anteil der Monozyten im Knochenmark dieser Tiere im Vergleich zu *Apoe*$^{-/-}$ Mäusen massiv erhöht. Darüber hinaus konnte eine vermehrte Aufnahme von oxidierten LDL-Partikeln (oxLDL) durch gezüchtete Makrophagen aus *Apoe*$^{-/-}$*Gpr55*$^{-/-}$ Tieren *in vitro* demonstriert werden. Während dieses Krankheitsstadiums stellten wir auch einen

substanziell veränderten Lipidmetabolismus in der Leber fest. Die Genexpression von Schlüsselenzymen der Cholesterinsynthese und des Cholesterintransports waren deutlich hochreguliert.

Zum späteren Zeitpunkt der Krankheit, nach 16 Wochen WD-Fütterung, wurden ebenfalls Unterschiede in der Läsionszusammensetzung beobachtet. Verglichen mit den *Apoe*$^{-/-}$ Tieren zeigten die atherosklerotischen Läsionen der *Apoe*$^{-/-}$*Gpr55*$^{-/-}$ Mäuse Merkmale weiter entwickelter Plaques mit höherem Kollagengehalt und größeren Nekrosezonen. Der histologische Vergleich von Aorten in Weibchen zeigte hierbei auch die aufgrund des *Gpr55*-Verlustes verursachte erhöhte Plaque-Last.

Verschiedene Leukozyten Subpopulationen wurden durch den kompletten Verlust von GPR55 beeinflusst. Die Aorten der *Apoe*$^{-/-}$*Gpr55*$^{-/-}$ Mäusen wiesen zum frühen Zeitpunkt mehr Lymphozyten und Neutrophile auf und zum späteren Zeitpunkt eine Hochregulation proinflammatorischer Gene. Dies werteten wir als Indiz für eine verstärkte inflammatorische Reaktion in diesem Gewebe. Im Vergleich zur Kontrollgruppe fanden sich auch vermehrte T- und B-Zellen im Blut der weiblichen *Apoe*$^{-/-}$*Gpr55*$^{-/-}$ Tiere. Lymphatische Gewebe wie Milz und Lymphkonten beinhalteten im fortgeschrittenerem Krankheitsstadium ebenfalls mehr B- und T Zellen als die *Apoe*$^{-/-}$ Kontrollen. Die bemerkenswertesten Unterschiede sahen wir jedoch bei B-Zellen. In lymphatischen Geweben waren die Subpopulationen hin zu proinflammatorischen Marginalzonen B2-Zellen verschoben und es ließen sich auch Veränderungen der relativen B1 Populationen feststellen. Der *Gpr55* Knockout führte zu einer Überproduktion vor allem von Immunglobulin G (IgG) Antikörpern. Es scheint, als beeinflusse GPR55 sowohl das spezifische Immunsystem als auch Teile der angeborenen Immunantwort im Kontext der Atherosklerose mit einem generell antiinflammatorischen Einfluss auf diese Zellen.

Diese Arbeit beschreibt den unverkennbaren Einfluss von GPR55 auf die Entstehung der Atherosklerose und die pro-atherosklerotischen Folgen des *Gpr55* Knockouts. Die GPR55/LPI Signalkaskade ist möglicherweise ein entscheidender Faktor in der Regulierung verschiedener bei der Atherosklerose beteiligter Leukozyten. Wir konnten einen Einfluss auf Neutrophile, Monozyten, Makrophagen, T-Zellen, B-Zellen und Antikörper im Serum demonstrieren. In der Zukunft sollte die Funktion von GPR55 in verschiedenen Zellpopulationen und die pharmakologische Beeinflussung des Rezeptors weiter untersucht werden, um möglicherweise die inflammatorischen Prozesse im Rahmen der Atherosklerose zu modifizieren.

3 INTRODUCTION

3.1 Cardiovascular diseases

Cardiovascular diseases (CVDs) are a collective term for disorders of the heart and blood vessels which include coronary heart disease, cerebrovascular disease, peripheral arterial disease, rheumatic heart disease and more. They are the leading cause of death worldwide and account for 31 % (approximately 17.9 million people) of all deaths, according to the World Health Organization[1]. Heart attack and stroke are the most common causes of death in CVD patients[2]. These disorders not only lead to death but are also associated with a considerable individual burden of disease along with a high burden on society, the economy, and the health care system. The most disability-adjusted life years (sum of years lost to a disease and years lived with the disease) lost to an illness are attributable to CVDs[2,3].

The most life-threatening complications are coronary artery disease and stroke, accounting for approximately 540000[4] and 440000[5] deaths per year in Europe, respectively. Myocardial infarction is usually caused by the occlusion of one or more coronary arteries, which limits the supply of oxygen to the myocardium, resulting in acute ischemic myocardial injury. An ischemic stroke is caused by a focal infarction in cerebral, spinal, or retinal vessels, which may lead to neurological dysfunction. In most cases, atherosclerosis is the underlying cause of these events[6]. Behavioral risk factors are of great significance for CVD development and are often underestimated by the individual and, therefore, untreated for several decades. Consequently, primary prevention strategies are fundamental to reducing the incidence of CVDs[7,8].

3.2 Atherosclerosis

Atherosclerosis is a multifactorial, progressive, and chronic inflammatory disease of large and medium-sized arteries. It is induced by the accumulation of lipids and subendothelial plaque formation[9,10]. This condition usually goes unnoticed during plaque development. Most often, symptoms will not appear until triggered by complications caused by atherosclerotic lesions. The plaques can obstruct the arterial lumen and thereby limit blood flow. Acute events such as plaque rupture or erosion lead to thrombus formation, which causes ischemia. Risk factors are divided into modifiable and nonmodifiable factors. The modifiable factors can be treated medically or through lifestyle changes and include dyslipidemia, hypertension, insulin resistance, diabetes, smoking, obesity, lack of physical activity and an unhealthy diet. Instead, age, male sex and genetic factors leading to an impaired lipid metabolism cannot be modified[7].

3.2.1 Pathogenesis of atherosclerosis

Healthy arteries consist of three distinct layers. The outermost layer is the tunica adventitia, composed of collagen fibers and elastic connective tissue embedding the vessel in the surrounding tissue. The tunica media is the broadest layer, formed by circumferential smooth muscle cells (SMCs), elastic fibers and connective tissue. The tunica intima is the innermost layer, always in contact with the blood flow, lined with endothelium and subendothelial connective tissue (Figure 1A). The arterial endothelium is responsible for vascular tone and permeability, prevention of thrombosis and maintenance of vessel integrity – all tightly regulated processes[11]. Atherosclerotic lesion development begins at places where the endothelial integrity is disrupted, and thus losing its important barrier properties. This pathophysiological process is multifactorial, involving mechanical and molecular stimuli. It results in a dysfunctional endothelium with structural alterations susceptible to atherosclerotic lesion development.

Atherosclerotic plaques form at predilection sites of low or oscillatory endothelial shear stress, near branch points, bifurcations and along inner curvatures[12]. The vessels most commonly affected are the abdominal aorta, coronary arteries, iliofemoral arteries, and carotid bifurcation. Low endothelial shear stress triggers intracellular cascades via mechanoreceptors that result in the upregulation of pro-atherogenic genes and the suppression of atheroprotective genes in endothelial cells (ECs). This process involves a network of different signaling pathways to provoke the upregulation of the expression of adhesion molecules, chemokines, and proinflammatory cytokines[13]. A dysfunctional endothelial barrier has increased permeability for apolipoprotein B-100 containing lipoproteins like low-density lipoprotein (LDL) which can bind to positively charged proteoglycans in the intima[14].

Proinflammatory stimuli induce the expression of adhesion molecules on ECs, which enhances leukocyte adhesion and penetration, and leads to local inflammation. An increase in EC turnover, as well as increased permeability for plasma molecules, contributes to changes in EC morphology[13]. These endothelial remodeling processes facilitate the response of the endothelium to coexisting risk factors such as dyslipidemia, hypertension, diabetes mellitus, and smoking. These changes lead to the initiation or progression of atherosclerotic lesions.

Attracted by adhesion molecules, the majority of cells recruited to the subendothelial space are monocytes, but lymphocytes and neutrophils are accumulating in the intima as well[6].

Monocytes are the most important cell type during atherogenesis. Upon recruitment to the intima, they differentiate into macrophages in response to growth factors produced by ECs and other cell types. LDL particles accumulated in the intima are modified by myeloperoxidase (MPO), lipoxygenase and reactive oxygen species (ROS), which results in the formation of oxidized LDL (oxLDL) particles, adding to EC activation[6]. Macrophages engulf oxLDL through scavenger receptors like cluster of

differentiation 36 (CD36) or scavenger receptor (SR) A1 and become foam cells – named after their microscopic appearance[15]. Foam cells themselves present antigens and attract other circulating leukocytes and secrete various cytokines and chemokines. This process fuels the ongoing and non-resolving inflammation in the vessel wall (Figure 1B).

Over time, the plaque becomes more and more complex and develops into an advanced atherosclerotic lesion. A characteristic process is the migration and proliferation of SMCs within the plaque. They are recruited from the media in response to a variety of mediators and inflammatory stimuli secreted by ECs and macrophages[10]. In the lesion, SMCs proliferate and produce extracellular matrix (ECM) components like collagen and elastin to stabilize the plaque and form a fibrous cap to cover it. This process is controlled by various cytokines, chemokines, and proteases. Transforming growth factor β (TGF-β) stimulates collagen synthesis and fibroblast differentiation, with interferon-γ (IFN-γ) counteracting this[6]. Matrix metalloproteinases (MMP) are released by mast cells, macrophages, SMCs and ECs and degrade collagen, a process which results in thinning of the fibrous cap, increasing its vulnerability to rupture[16]. Foam cells are trapped in the nascent plaque and will eventually become apoptotic. Clearance of apoptotic and necrotic cells is insufficient, resulting in an area within the plaque called the necrotic core that is composed of apoptotic and necrotic cells, cell debris, cholesterol crystals and other extracellular material[17] (Figure 1C).

An advanced plaque contains a necrotic core covered by a fibrous cap. The fibrous cap plays a pivotal role in plaque stability and its strength is determined by the collagen synthesized by SMCs. When a plaque is mechanically ruptured, material with highly thrombogenic properties is exposed to the circulation. This may cause thrombus formation, occlusion of an artery and subsequent ischemia (Figure 1D). Vulnerable plaques prone to rupture have large necrotic cores, an abundance of inflammatory cells, and a thin fibrous cap with a comparatively low content of collagen, SMCs, and ECM[18].

Several mechanisms weaken the atherosclerotic plaque. Usually, a combination of fibrous cap thinning and expansion of the necrotic core increases the risk of plaque rupture. Inflammatory mediators secreted by macrophages and cytotoxic lymphocytes, as well as granule proteins of mast cells and neutrophils, induce SMC apoptosis. The inflammatory environment of the plaque reduces collagen production and promotes collagen degradation via MMPs. This leads to a reduction in collagen and ECM content[19]. Necrotic core expansion occurs due to macrophage and SMC apoptosis in the advanced lesions, which cannot be cleared effectively through efferocytosis.

Intraplaque neoangiogenesis is triggered by different growth factors in the lesion and opens a new portal of entry for inflammatory leukocytes and thus contributes to plaque weakening (Figure 1C)[19].

A comparatively new pathophysiological concept behind plaque-caused thrombosis is plaque erosion. Compared to lesions vulnerable to rupture, lesions predisposed to superficial erosion feature fewer inflammatory cells and foam cells. Instead, they are characterized by a thick fibrous cap and a disrupted endothelial layer and contain neutrophil extracellular traps (NETs)[20]. New diagnostic methods such as intravascular optical coherence tomography might be a valuable tool to gain more insights into the morphology of plaque erosion[21].

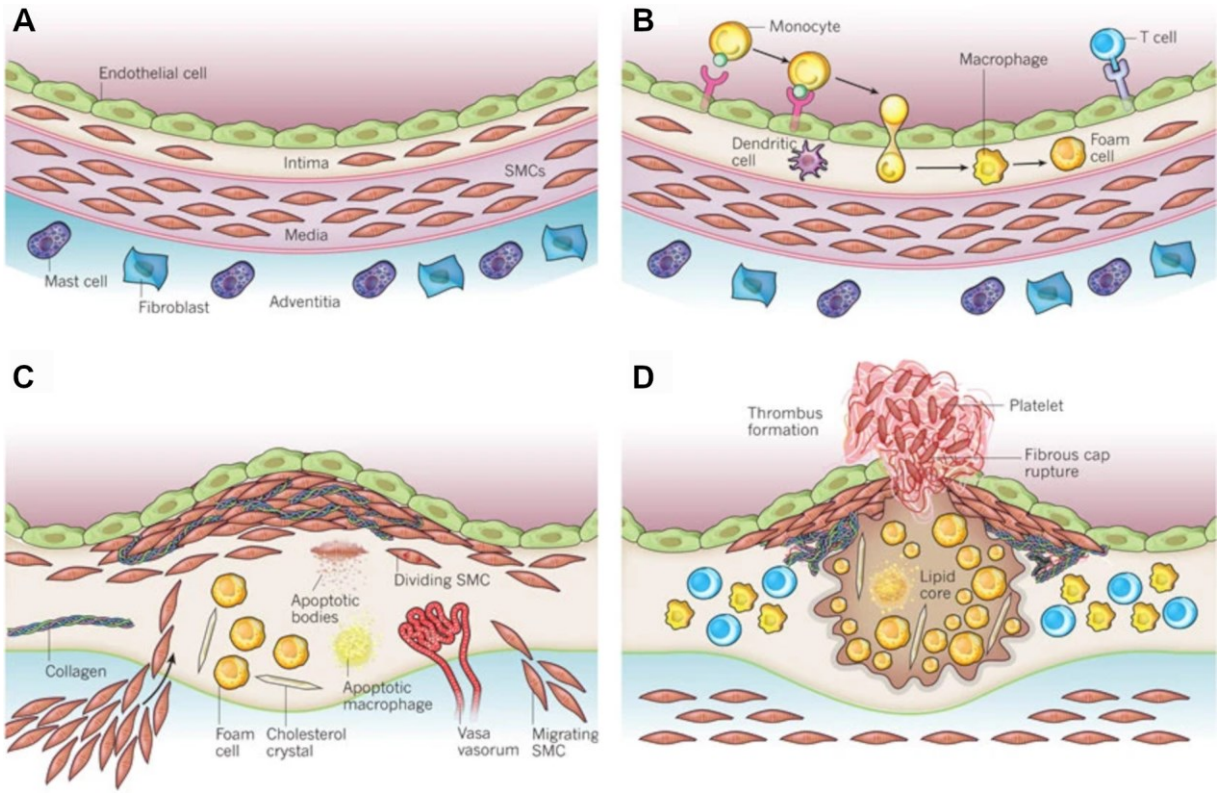

Figure 1: The pathogenesis of atherosclerosis.
The development of an atherosclerotic lesion from the healthy artery to a thrombotic lesion is shown. (**A**) A healthy artery comprises three distinct layers. The tunica intima, lined with endothelium, is in direct contact with the bloodstream. In humans, this layer already contains smooth muscle cells (SMCs). The tunica media is the broadest layer, comprised of SMCs and extracellular matrix (ECM) that enables contractility and ensures the stability of the vessel. The outer layer of the artery, tunica adventitia, anchors the vessel in its surroundings. It contains microvessels, lymphatic vessels and nerve endings. (**B**) A dysfunctional endothelial barrier increases the susceptibility to adhesion and migration of leukocytes into the intima. Particularly monocytes contribute to lesion development. They differentiate into macrophages and take up lipids to become foam cells. (**C**) The more advanced a lesion becomes, the more complex its composition becomes. SMCs are recruited from the media and produce collagen and ECM proteins to strengthen the structure of the lesion and prevent rupture. A necrotic core forms as a result of insufficient clearance of apoptotic cells. Intraplaque neovascularisation allows for leukocytes to enter the lesion via vasa vasorum. (**D**) After the rupture of the fibrous cap, thrombosis is the most feared complication of an atherosclerotic lesion. Highly pro-coagulative components of the inside of the plaque get in contact with the bloodstream and cause thrombus formation. This can occlude the artery and cause ischemia. (Copied from Libby et al.[10])

3.2.2 Immune cells and their role in atherosclerosis

Over the past years, the molecular mechanisms that drive plaque development have become better understood. It has emerged that the disease is not solely based on lipid accumulation, but that immune cells and inflammation contribute significantly[14,22,23].

3.2.2.1 Neutrophils

Neutrophils are short-lived granulocytes and often the first responders to an inflammatory event. They are part of the innate immune system and the most common white blood cells in humans. Neutrophils play a vital role in acute inflammation because of their ability to migrate to the site of inflammation in response to chemotaxis within minutes. Activated neutrophils phagocytize and kill pathogens through various mechanisms. They release granules containing a multitude of cytotoxic proteins and produce ROS and NETs[24]. Neutrophils have a circulating lifespan of fewer than 24 hours. When active in the interstitium, they live for a maximum of three days before undergoing apoptosis.

Due to their rapid turnover, constant reproduction from hematopoietic stem cells (HSCs) in the bone marrow is necessary. Granulopoiesis and the release of neutrophils into the circulation are controlled by chemokines, adhesion molecules and growth factors[25]. Extramedullary neutrophil production in the spleen is possible under conditions of metabolic stress and malignant or chronic diseases such as atherosclerosis.

Circulating neutrophil counts correlate positively with a higher risk of cardiovascular events in humans, as well as early atherosclerotic lesion size in the Western diet (WD) treated *Apoe*$^{-/-}$ mice.[25,26]. Experiments with neutropenia in mice during the first 4 weeks of atherogenesis showed reduced lesion size, whereas neutrophilia enhanced atherosclerosis[26]. Neutrophils influence all stages of lesion development[27]. In early atherogenesis, they are recruited to the endothelium by chemokines like chemokine (C-X-C motif) ligand 1 (CXCL1) and activation of chemokine (C-X-C motif) receptor 2 (CXCR2), but also via chemokine (C-C motif) ligand 5 (CCL5), released by activated platelets. Neutrophils facilitate the recruitment of monocytes to the atherosclerotic lesion by increasing the expression of adhesion molecules in ECs and by secreting chemotactic proteins[26]. They add to the processes that disrupt the endothelial barrier and thus increase the adhesion and transmigration of immune cells and LDL particles to the intima[27]. MPO released by neutrophils catalyzes the oxidation of LDL to oxLDL, which contributes to foam cell formation. Proteins secreted by neutrophils impact macrophages towards a more proinflammatory phenotype (Figure 2A). But not only early lesion development is affected by neutrophils. They accumulate in the shoulder regions of fully developed plaques and the number of neutrophils is higher in unstable lesions that are more prone to rupture.

By secreting histone H4-rich NETs, neutrophils have cytotoxic effects on SMCs[28], which ultimately leads to thinning of the fibrous cap (Figure 2B).

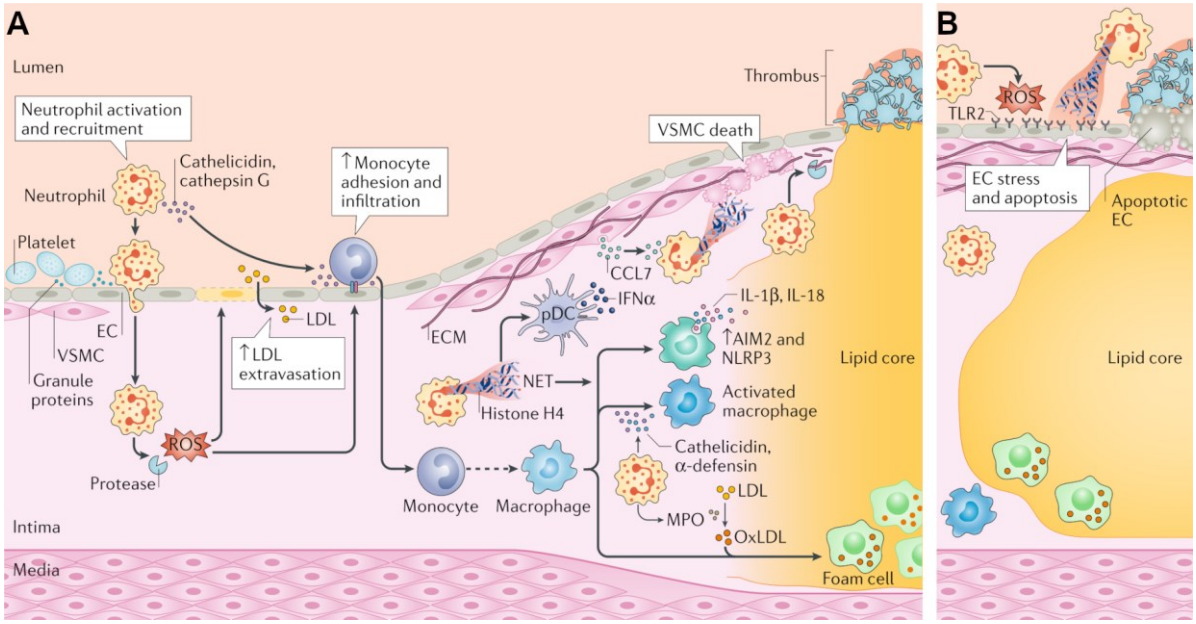

Figure 2: The role of neutrophils in atheroprogression.
(**A**) The schematic illustrates the contribution of neutrophils to atherogenesis, showing early lesion development in the left part and plaque progression to the right. Neutrophils can be activated and recruited to the endothelium by CCL5 released by platelets. When activated, neutrophils secrete granule proteins like cathelicidin and cathepsin G to facilitate monocyte recruitment to the lesion. Secreted proteases and reactive oxygen species (ROS) promote endothelial cell (EC) dysfunction and dysfunction of the extracellular matrix (ECM) underneath. This further increases the ability of leukocytes and low-density lipoprotein (LDL) particles to infiltrate the intima. Macrophages respond to neutrophil-derived proteins and develop a more proinflammatory phenotype, which stimulates them to secrete inflammatory cytokines. Myeloperoxidase (MPO) catalyzes the oxidation of LDL particles and promotes foam cell formation. Neutrophil extracellular traps (NETs) influence different mechanisms and cell types. They can activate plasmacytoid dendritic cells (pDCs) and macrophages to release cytokines and interferons. In advanced plaques, NETs induce vascular smooth muscle cell (VSMC) death through the cytotoxic properties of histone H4 and ECM degradation, thus thinning the fibrous cap and resulting in plaque destabilization. (**B**) Neutrophils are involved in EC desquamation. EC and apoptosis are, among other things, triggered by NET release and involve toll-like receptor 2 (TLR2) activation. (Adapted from Silvestre-Roig et al.[19])

3.2.2.2 Monocytes and macrophages

Monocytes are generally regarded as the most important cell type and the main driver in the development of an atherosclerotic lesion. They give rise to macrophages, the most abundant cell type in the plaque, and play a key role in every stage of lesion development[29]. Monocytes originate from a common myeloid progenitor in the bone marrow in a process called myelopoiesis and are released into the bloodstream when fully matured[30]. The spleen is a reservoir for monocytes that can be rapidly mobilized and contribute to an increase in the number of circulating Ly6C^{high} monocytes in the context of atherosclerosis[31].

Monocytes are divided into subgroups, identified by their surface markers. In mice, classical monocytes are defined as Ly6C^{high}CCR2^{high}CX$_3$CR1^{low}, intermediate monocytes as Ly6C^{int}CCR2^{-}CX$_3$CR1^{high} and nonclassical monocytes as Ly6C^{low}CCR2^{-}CX$_3$CR1^{high}. This corresponds to CD14^{++}CD16^{-}, CD14^{++}CD16^{+} and CD14^{+}CD16^{++} monocytes in humans, respectively[32,33].

The classical monocyte subsets act proinflammatory and are able to infiltrate damaged tissues, whereas the nonclassical monocytes have an anti-inflammatory role and patrol along the endothelium during homeostasis[34]. Hypercholesterolemia in mice[35] and humans[36] is associated with increased proinflammatory properties of circulating monocytes.

During the initiation of an atherosclerotic lesion, monocytes infiltrate the subendothelial space in response to the accumulation of ApoB-containing lipoproteins in a multistep process (Figure 3). Lipoproteins retained on subendothelial proteins activate ECs to express a variety of adhesion molecules that interact with receptors on the monocytes and lead to their migration into the endothelium. Selectins like P-selectin are responsible for leukocyte tethering and initiate the rolling of the monocytes along the endothelium. Subsequent integrin activation, most notably the interaction of intracellular adhesion molecule 1 (ICAM1) and vascular cell adhesion molecule 1 (VCAM1) on ECs and very late antigen-4 (VLA4) and lymphocyte function-associated antigen-1 (LFA1) on the monocytes, enables adhesion to the endothelium. This process is followed by the transmigration of the monocytes into the subendothelial space along a chemotactic gradient of EC-secreted chemoattractants[37,38].

Lesional monocytes develop into resident macrophages upon stimulation with macrophage colony-stimulating factor (M-CSF) and granulocyte-macrophage colony-stimulating factor (GM-CSF) secreted by ECs. The main macrophage phenotypes are proinflammatory “M1-type” and anti-inflammatory “M2-type” macrophages. This is a simplified representation, mainly based on *in vitro* data, of a wide range of macrophage subpopulations in the plaque. Each of them exerts different roles in atherogenesis and inflammation. The differentiation of monocytes into these subtypes depends on the exposure to different cytokines. Cytokines released by T_H1 cells (tumor necrosis factor α (TNF-α), IFN-γ and IL-2) stimulate M1 polarization, while T_H2-derived cytokines (IL-4, IL-10 and IL-13) stimulate M2 polarization. “M1-type” macrophages produce proinflammatory cytokines and fuel the inflammatory response. “M2-type” macrophages secrete anti-inflammatory mediators, have a reparative phenotype and reduce inflammation[39,40].

In mice, early lesion development is shaped by “M2-type” macrophages, whereas advanced lesions feature more “M1-type” macrophages. This development is reversed during plaque regression. In humans, “M1-type” macrophage markers are increased in vulnerable plaques and they accumulate in rupture-prone shoulder regions[41].

Monocytes are continuously recruited to the atherosclerotic lesions from the circulation. However, murine studies revealed that a substantial number of tissue-resident macrophages contribute to macrophage turnover in the plaque as well[42,43]. Once recruited to the endothelium and differentiated into macrophages, resident macrophages proliferate and increase the numbers of macrophages in the plaque[44].

A range of different mechanisms facilitates the uptake of modified lipoproteins by plaque-resident macrophages. Unlike the LDL receptor, the activity of scavenger receptors like SR-A1 and CD36 is not inhibited by an increase in intracellular cholesterol content. They enable the uptake of excess amounts of lipoproteins into the macrophages to become foam cells (Figure 3)[6]. Pinocytosis and efferocytosis of lipids add to that process[45,46]. Internalized lipoproteins are hydrolyzed and re-esterified to different cholesteryl fatty acid esters and receptor-mediated efflux of cholesterol is possible. Reverse cholesterol transport is mediated by ATP-binding cassette A1 (ABCA1), ATP-binding cassette G1 (ABCG1) and SR-B1 to circulating ApoA1 or high density lipoprotein (HDL) molecules[29].

Macrophages modulate the development of an atherosclerotic lesion by secreting a wide range of cytokines and chemokines[47]. They stimulate SMC migration and proliferation, enhance plaque development through increased recruitment of leukocytes to the lesion and participate in plaque rupture and thrombosis[14].

Lipid-loaden foam cells show impaired migratory capacity and become trapped in the atherosclerotic plaques. Subsequent macrophage death occurs through a combination of different mechanisms that have been found *in vitro* and *in vivo* (Figure 3). Apoptotic foam cells cannot be sufficiently cleared, because of defective efferocytotic capabilities of phagocytes in the plaque. This results in the formation of a necrotic core in the advanced atherosclerotic lesion[17].

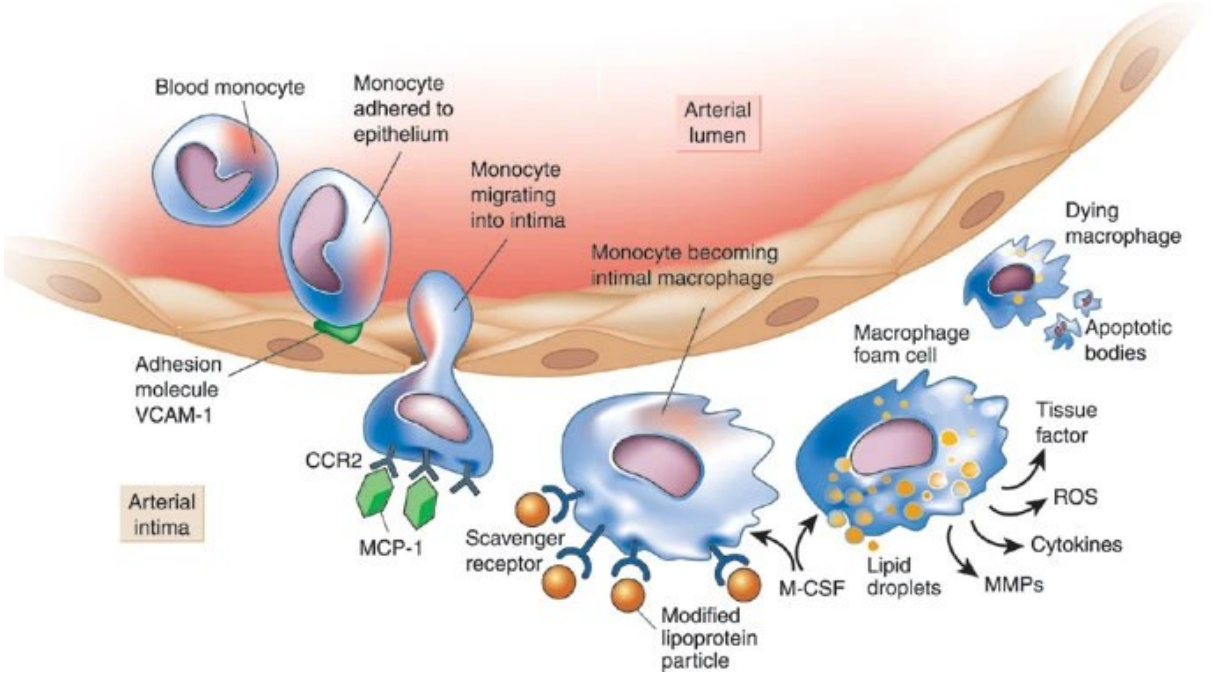

Figure 3: The role of monocytes and macrophages in atherogenesis.
This figure illustrates the recruitment of monocytes to the atherosclerotic plaque, their development into foam cells and the pathophysiological functions of these cells. Activated endothelial cells express adhesion molecules (e.g. vascular adhesion molecule 1, VCAM-1) that facilitate the adhesion and subsequent entry of monocytes into the endothelium. Once recruited to the nascent plaque, growth factors (e.g. macrophage colony-stimulating factor, M-CSF) foster the differentiation of monocytes into macrophages. They can take up modified lipoproteins that have accumulated in the endothelium via scavenger receptors and convert into foam cells packed with lipid droplets in the cytoplasm. Foam cells are critically involved in the inflammatory process within the atherosclerotic lesion. They secrete a plethora of chemokines and cytokines, as well as matrix metalloproteinases (MMPs) and reactive oxygen species (ROS) that promote a non-resolving inflammation. Apoptotic macrophages that are not sufficiently cleared build the necrotic core of an atheroma. (Copied from Libby et al.[22])

3.2.2.3 Natural killer cells

Natural killer (NK) cells are lymphocytes of the innate immune system and play a central role in the immune reaction to viral infections, tumor formation and in regulating immune responses. They protect the body with their ability to lyse virally infected cells and tumor cells without prior antigen sensitization.

The activation of NK cells is unique in comparison to other immune cells. Usually, the cell surface protein major histocompatibility complex I (MHC-I) presents cytosolic peptides on most nucleated cells. When these peptides are recognized as “foreign,” cytotoxic T cells are activated. However, NK cells are activated by the absence of MHC-I, and these cells are identified as targets for NK cell-mediated cell lysis when they would otherwise be under the radar of cytotoxic T cells. They are also activated by a range of different cytokines released by other leukocytes. NK cells have cytoplasmatic granules containing perforin and granzymes, which on release can induce apoptosis or cell lysis to target cells. By secreting many different chemokines and cytokines like TNF-α, IFN-γ, or IL-10, NK cells help to shape the whole immune response to an inflammatory stimulus[48].

Although few in number, NK cells can be found in human and murine atherosclerotic lesions[49,50]. Early studies proposed a pro-atherogenic role by increasing the size of necrotic cores, possibly through cytotoxic mechanisms dependent on perforin and granzyme B secretion[49,51]. These results were controversial because of a lack of specific mouse models. The methods used to induce genetic NK cell deficiency or NK cell depletion in mice had off-target effects on other immune cells[52].

Nour-Eldine et al. used several new approaches to study the effects of NK cell deficiency and NK cell hyperactivation on atherosclerotic lesion development in mice[53]. They observed no effect on natural atherogenesis attributable to NK cells. Lesion size and cellular composition did not differ from the control group at early as well as later stages of atherogenesis. Additionally, they used a model of chronic viral infection, representing a condition of NK cell activation. NK cell-deficient mice had significantly smaller lesions with reduced macrophage content compared to the control group. This suggests a pro-atherogenic role for NK cells in selective conditions when they are systemically activated. With new mouse models of NK cell depletion and NK cell hyperactivation, the study by Nour-Eldine et al. provides revised insight into the role of NK cells in atherosclerosis.

3.2.2.4 T lymphocytes

T cells are part of the adaptive immune system and are named after the thymus where they develop. They originate from HSCs in the bone marrow and migrate into the thymus at the stage of common lymphoid progenitor cells. During maturation in the thymus, a stringent selection process ensures that only those T cells survive that recognize MHC complexes and at the same time, do not bind to endogenous peptides. This leads to self-tolerance as well as specific antigen detection properties that can quickly adapt to new pathogens. A key feature of adaptive immunity is the recognition of a large number of different molecular structures. In T cells this is possible through the T-cell receptor (TCR), which is generated by germ-line rearrangement. Different T cell subsets with individual characteristics evolve in the thymus. All T cells express CD3 as a surface marker and are divided into subgroups. The main subset is the $CD4^+$ T helper cell (T_H), further divided into T_H1 and T_H2 cells. T helper cells modulate the activity of other immune cells through the secretion of cytokines. T_H1 cells increase cell-mediated immune responses of macrophages, $CD8^+$ T cells and B cells via IFN-γ and IL-2 secretion. T_H2 cells stimulate a humoral immune response. Another major subpopulation is the cytotoxic $CD8^+$ T cell. These cells are activated by antigens presented by MHC-I and protect against virus-infected and abnormal cells. They secrete the cytokines TNF-α and IFN-γ and induce cytotoxicity through the release of cytotoxic granules containing perforin and granzymes and induce apoptosis via surface receptor interactions. Besides these main subsets, there are a variety of other T cells with specific functions, such as memory T cells, regulatory T cells (T_{reg}), natural killer T cells (NKT), and γδ T cells[54].

T cells are the second most abundant leukocyte subset in atherosclerotic plaques. They contribute to atherosclerotic lesion development by secreting various cytokines and chemokines that directly modulate the behavior of other leukocytes. T_H1 $CD4^+$ cells are polarized towards a proinflammatory phenotype and are the most frequently found T cells in the lesion. They produce IFN-γ and TNF-α, which leads to macrophage polarization towards the proinflammatory “M1 type”. Less frequently found T_H2 cells counteract this by stimulating macrophages towards the “M2 phenotype”[55]. T_H1 cells are considered proatherogenic. Reducing the function of T_H1 cells in different ways leads to reduced atherosclerosis in mice, indicating a proatherogenic role for T_H1 $CD4^+$ cells[56,57]. T_H2 cells are regarded as primarily atheroprotective. However, the experimental data are contradictory[58]. T_{reg}s and their secreted cytokines TGF-β and IL-10 are essential for the resolution of an inflammatory response and reducing plaque burden in mice[59,60]. $CD8^+$ T cells are found in atherosclerotic plaques, but their role is not easily assessed. Studies show that $CD8^+$ T cells exacerbate atherosclerosis by secreting proinflammatory cytokines and inducing apoptosis of macrophages, SMCs, and ECs. In contrast, other researchers demonstrated atheroprotective effects by reducing the number of antigen-presenting cells in the plaque[55].

3.2.2.5 B lymphocytes

B cells are lymphocytes of the adaptive immune arm and are responsible for antibody-mediated humoral immunity. Immature B cells migrate from the bone marrow to secondary lymphoid organs in the periphery and complete the final stages of maturation there. Similar to the TCR, each B cell establishes a unique B-cell receptor (BCR) through somatic recombination, which controls the activity of the B cell. Mature B cells are heterogenous and consist of several subpopulations with different surface markers, tissue localizations, antibody profiles and unique characteristics and functions. The main subsets are B1 cells, divided into B1a and B1b, and B2 cells, separated as follicular (FO) and marginal zone (MZ) B2 cells[61].

B1 cells primarily originate from fetal liver HSCs and reside in peripheral tissues, where they are able to self-renew. They are mainly present in the pleural and peritoneal cavities, but a small population is found in the spleen as well. In contrast to B1b cells, B1a cells express the surface marker CD5. B1 cells produce the majority of IgM antibodies[62].

B2 cells have a shorter lifespan and need to be constantly renewed from hematopoietic precursor cells in the bone marrow. B2 FO cells circulate between secondary lymphoid organs via blood and lymph vessels and react to T cell-dependent antigens. Upon antigen activation, they differentiate into plasma cells to produce large amounts of antibodies or become memory B cells. Memory B cells are quicker to respond to an antigen if a secondary immune response occurs. B2 MZ cells reside in the spleen and other lymphoid tissues without the ability to circulate

between them. They are in the first line of defense against antigens in the circulation through their location in the spleen[62].

The first studies on B cells in the context of atherosclerosis suggested an overall atheroprotective role[57]. Elimination of B cells by splenectomy increased atherosclerotic plaque formation and adoptive transfer of B cells of older *Apoe*$^{-/-}$ mice reduced disease severity in young *Apoe*$^{-/-}$ animals[63]. LDL receptor-knockout mice (*Ldlr*$^{-/-}$) with B cell-deficient bone marrow[64] as well as *Ldlr*$^{-/-}$ mice unable to secrete IgM showed an increase in lesion size[65]. Other groups, however, reported that B cells aggravated atherosclerosis. B cell depletion using anti CD20 antibody and experiments in *Apoe*$^{-/-}$ mice lacking the receptor for B-cell activating factor (BAFF), a factor necessary for B cell maturation and survival, resulted in attenuated atherosclerosis[57]. The investigation of specific B cell populations revealed that different types of B cells contribute to atherogenesis in a subset-dependent manner (Figure 4).

B1a cells secrete natural IgMs, which inhibit the uptake of oxLDL by macrophages and thus attenuate foam cell formation, which results in an overall reduction in foam cell-secreted cytokines. These IgM antibodies also help with apoptotic cell clearance[66]. Rosenfeld et al. demonstrated an atheroprotective role for B1b cells as well. They secrete IgM antibodies against oxidation-specific epitopes that can be found on oxLDL and apoptotic cells. However, the effect is not as impactful as the atheroprotective role of B1a cells[67].

Immunoglobulin G (IgG) antibodies against oxLDL-activated macrophages result in a proinflammatory response, but the experimental data available is conflicting[68]. Experimental studies deciphering the role of B2 cells in atherosclerosis have so far provided inconclusive results. The ratio of FO B2 to MZ B2 cells is shifted towards B2 MZ cells in atherosclerosis[69]. MZ B2 cells were shown to inhibit the response of pro-atherogenic follicular T helper cells to hypercholesterolemia and thereby act atheroprotective[70]. FO B2 cells, however, promote the inflammatory response of T_H1 cells by differentiating into plasma cells and producing IgGs[71].

Another B cell subset – the innate response activator (IRA) B cell – is a source for GM-CSF. GM-CSF leads to the generation of dendritic cells (DC) in the lesion, which consecutively increases the amount of proatherogenic T_H1 cells. Atherosclerotic mice depleted in GM-CSF secreting IRA B cells had reduced atherosclerotic plaque burden as well as a decrease in T_H1 cells. These results suggest a proatherogenic role of IRA B cells due to their impact on DCs via GM-CSF[72].

The complex nature of B cell functions and interactions results in both atheroprotective and proatherogenic roles.

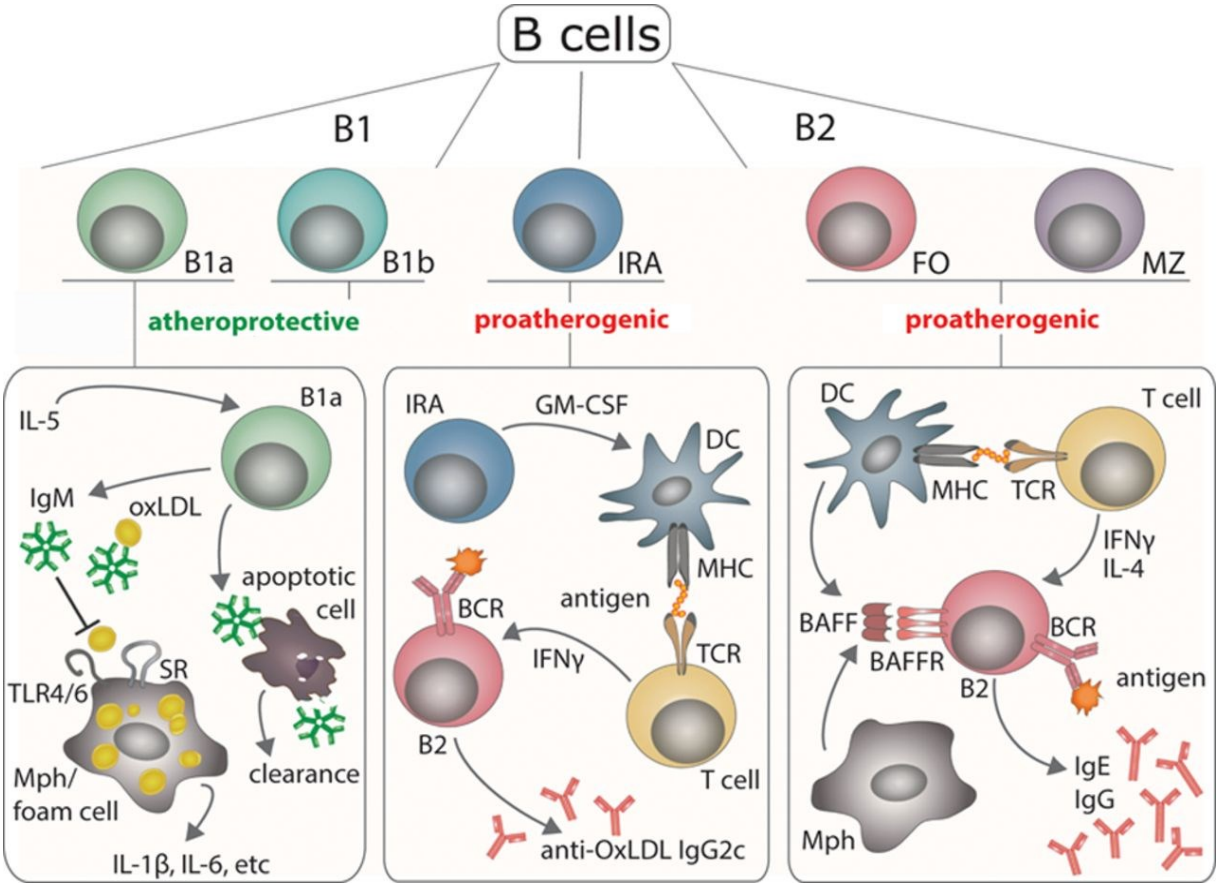

Figure 4: The role of B cell subsets in atherosclerosis.
B cells are divided into subsets according to activation, localization, surface marker and immune function. The main subpopulations are B1 and B2 cells. The B1 lineage includes B1a and B1b cells. B1a cells secrete immunoglobulin M (IgM) antibodies targeted towards oxidized low-density lipoprotein (oxLDL) particles, which reduces foam cell formation. IgM is also capable of apoptotic cell clearance. The activity of B1a cells is enhanced by interleukin 5 (IL-5). B1b cells also secrete IgM aimed at oxidation-specific epitopes and reduce atherosclerotic plaque burden. Innate response activator (IRA) B cells secrete granulocyte-macrophage colony-stimulating factor (GM-CSF) which activates dendritic cells (DC) and increases the amount of proatherogenic T cells. B2 cells, comprised of follicular (FO) and marginal zone (MZ) B2 cells, reside in secondary lymphoid organs, mainly the spleen. Studies indicate a proatherogenic role of B2 cells. DCs and T cells activate B2 cells to secrete antibodies and B cell-activating factor (BAFF) is essential for the survival and maturation of B2 cells. (Adapted from Tsiantoulas et al.[61])

3.2.3 Mouse models of atherosclerosis

A variety of animal models have been established to study atherosclerosis, including large animal models such as pigs, rabbits, and non-human primates, as well as the predominantly used mouse models. Ideally, an animal model would come as close as possible to human anatomy and pathophysiology so that results could be applied to patient treatment. However, none of the existing models are optimal for mimicking atherogenesis in humans. Nevertheless, they provide valuable tools for expanding knowledge about this chronic disease[73]. Mice are the most commonly used laboratory animals in preclinical cardiovascular research. Mouse breeding is well established, they can be maintained at a reasonable cost, their reproduction rate is rapid and genetic manipulation is available for an abundance of cell types and genes

as well as regulatory non-coding RNAs[74]. This enables time- and cost-efficient research. Wild type (WT) mice have a significantly different lipid profile compared to humans and typically do not develop atherosclerosis. In mice, circulating cholesterol is primarily carried in HDL. The pro-atherogenic lipoproteins LDL and very-low-density lipoprotein (VLDL) play a minor role, which is why genetic modification of the murine lipid metabolism is required[74]. The two most widely used models are based on the genetic ablation of either apolipoprotein E (*Apoe*) or the low-density lipoprotein receptor (*Ldlr*). The glycoprotein Apoe is a structural component of all lipoprotein particles except LDL, mediating the uptake of lipoproteins into the liver by the LDL receptor and the LDL receptor-related protein[75]. The first *Apoe* knockout (*Apoe*$^{-/-}$) mouse line was developed in 1992[76,77]. The clearance of plasma lipoproteins is severely impaired in these mice, increasing plasma cholesterol levels significantly in comparison to WT mice. This results in hypercholesterolemia with the accumulation of mainly VLDL and chylomicron remnants when fed a chow diet and is enhanced when fed a high fat (21 %) and high cholesterol (0.2 – 1.3 %) diet, referred to as Western diet (WD). These mice show a rapid development of atherosclerotic plaques[78]. Despite its role in lipoprotein clearance, Apoe is also involved in dietary absorption and biliary excretion of cholesterol[79], macrophage biology[80], adipose tissue biology and immune function[81], potentially influencing lesion development.

The second most common model is the LDL receptor-knockout mouse (*Ldlr*$^{-/-}$), in which LDL receptor-mediated clearance of lipoproteins is blocked[82]. The atherosclerotic lesion phenotype is comparable to the *Apoe*$^{-/-}$ mouse model, although less pronounced since mice only develop plaques when fed with WD. The advantages over the *Apoe*$^{-/-}$ model is that the LDL receptor has no function outside of lipoprotein clearing and that the lipoprotein profile of *Ldlr*$^{-/-}$ mice is more similar to that of humans[83].

Some notable differences between human and murine atherosclerotic lesions must be considered when studying murine data[84]. Plaques in mice progress within a few weeks, while it takes decades for atherosclerotic lesions to develop in humans. Atherosclerosis manifests at different predilection sites in both species. In mice, the aortic root, the aortic arch, the brachiocephalic trunk, and branch points of the aorta are most frequently affected[85]. In contrast to human atherosclerosis, the coronary arteries are usually lesion-free and plaque rupture and thrombosis are rare[86]. With the traditional mouse models, researchers can study lesion development but due to differences in lesion morphology, plaque rupture does usually not occur in mice[19]. In summary, animal models of atherosclerosis are invaluable for basic cardiovascular research. They help us understand the mechanisms underlying atherosclerosis better and thus enable new treatment strategies.

3.3 G protein-coupled receptors

With over 1000 different genes, G protein-coupled receptors (GPCRs) represent the largest and most diverse family of receptors for a variety of stimuli. These transmembrane proteins can be activated by hormones, biogenic amines, neurotransmitters, chemokines and metabolites such as amino acids, fatty acids and many more. They are ubiquitously expressed and the most common target of therapeutic drugs, so knowledge about GPCRs is crucial for modern medicine[87]. GPCRs are classified based on sequence homologies in class A (rhodopsin-like), class B (secretin-like), class C (glutamate-like), adhesion family and frizzled family[88]. They all share a common structure that has been conserved during eukaryote evolution. Seven transmembrane helices, connected by three intra- and three extracellular loops, are located within a cell's plasma membrane. In principle, the binding of an external signaling molecule to the outside loops causes a conformational shift of the GPCR, which triggers an interaction between the receptor and a guanine nucleotide-binding protein (G protein) located inside the cell.

There are two classes of G proteins, the heterotrimeric G protein complex consisting of three subunits (α, β, and γ) and the family of monomeric small GTPases, which are equal to the α subunit but are able to function independently. Both can be further divided into subfamilies based on the structure of the α subunit. One GPCR can bind to more than one G protein subfamily. In the inactive state, guanosine diphosphate (GDP) is bound to the G protein. Following activation, GDP is exchanged for guanosine triphosphate (GTP) through guanine-nucleotide exchange factor (GEF) activity, the G protein detaches from the GPCR, and the α, β and γ subunits can trigger an intracellular signaling cascade. The transformation back into the resting state is accomplished when GTP is hydrolyzed to GDP by the GTPase-activating protein and the G protein subunits form a heterotrimer again[89] (Figure 5). GPCR signaling is highly complex, well-regulated, and essential to all physiological and pathophysiological processes in eukaryotes. Not yet fully characterized GPCRs are called orphan receptors. They offer tremendous possibilities, providing novel therapeutic targets and access to currently unknown signal transduction pathways.

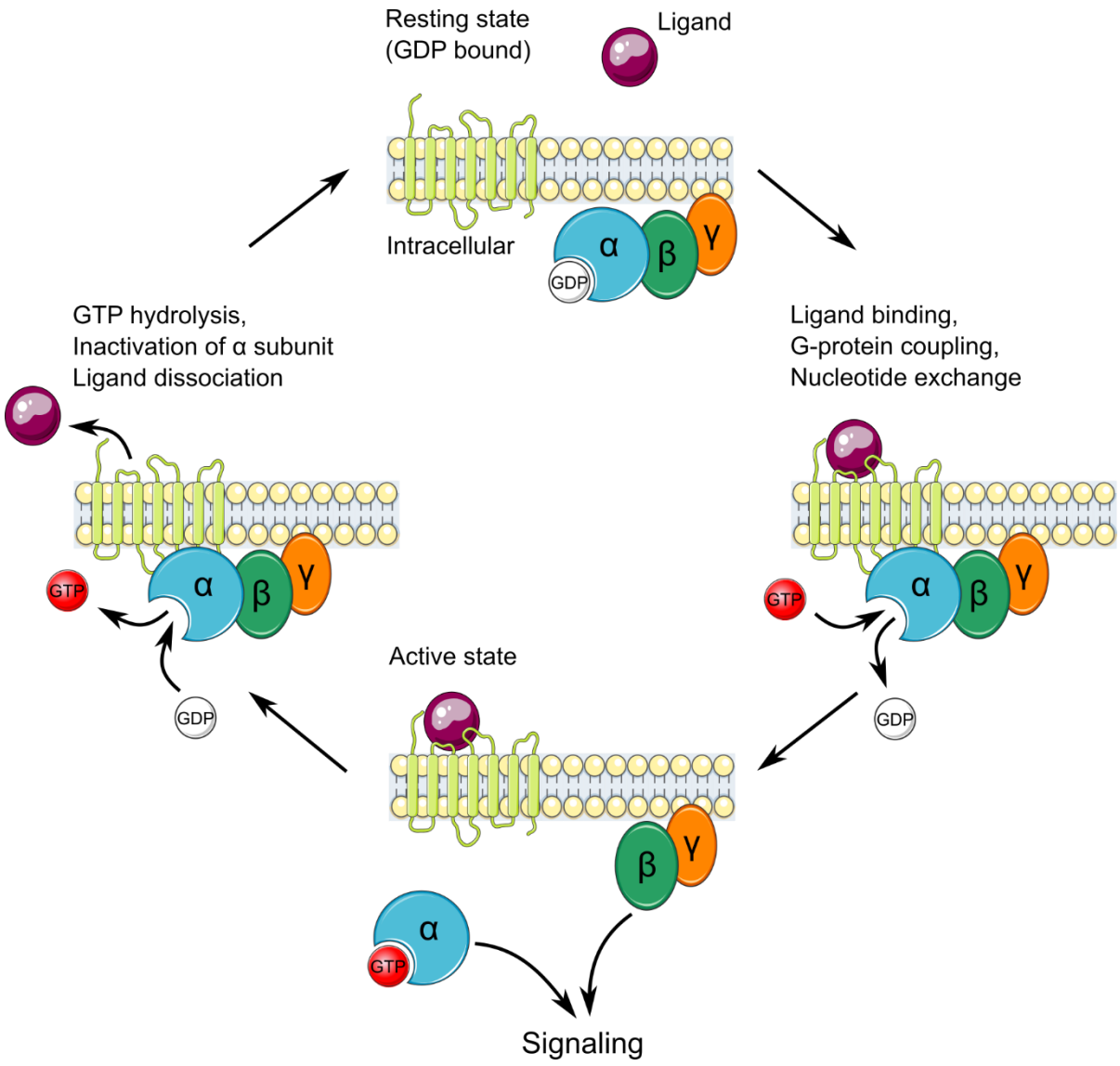

Figure 5: Common G protein-coupled receptor (GPCR) activation cycle.
When in a resting state, guanosine diphosphate (GDP) is bound to the G protein's α-subunit. Ligand binding triggers a conformation change that facilitates the exchange of GDP for guanosine triphosphate (GTP) through guanine-nucleotide exchange factor (GEF) activity. The G_{α} subunit bound to GDP dissociates from the $G_{\beta\gamma}$ dimer and the GPCR is achieved when GTP is hydrolyzed to GDP by the G_{α} subunit, which then is able to reassociate with the G protein and $G_{\beta\gamma}$.

3.3.1 Discovery of the G protein-coupled receptor 55

The orphan G protein-coupled receptor 55 (GPR55) was first discovered and successfully cloned by Sawzdargo et al. in 1999 through in silico patent research[90]. They obtained data from the Expressed Sequence Tags (EST) databank maintained by the National Center for Biotechnology Information (NCBI). ESTs are short messenger ribonucleic acid (mRNA) sequences – usually below 1000 base pairs – from a specific tissue and published for public usage. GPCRs share a characteristic and conserved amino acid motif of the seven transmembrane domains. The authors were able to identify the previously unknown human gene *Gpr55* using the Basic Local Alignment Search Tool[91] on the data received from the EST databank.

Fluorescence in situ hybridization analysis revealed its location on chromosome 2q37 in humans (GenBank Accession number: NM_005683)[90] and the mouse orthologue on chromosome 1 (GenBank Accession number: NM_001033290). It encodes a 319 amino acid protein and a 327 amino acid protein, respectively[92]. Murine *Gpr55* shares 78 % sequence identity compared to the human gene. The exact sequence of the human gene varies between different authors. A possible explanation for this are polymorphisms or errors during cloning or sequencing[93].

3.3.1.1 GPR55 classification

Two patents revealed interactions between GPR55 and cannabinoid receptor ligands[94,95] and Ryberg et al. were among the first to propose GPR55 as a new member of the cannabinoid receptor family[93]. They used human embryonic kidney 293 (HEK293) cells transfected with human *GPR55* and a radioligand binding assay to observe interactions of the synthetic cannabinoids CP55940 and O-1602, the endogenous endocannabinoids Anandamide, Noladin ether, 2-arachidonoylglycerol (2-AG), virodhamine, palmitoylethanolamide (PEA), oleoylethanolamide and plant-derived cannabinoids Δ^9-tetrahydrocannabinol (Δ^9-THC), cannabinol, cannabidiol (CBD) and other compounds with GPR55. They were able to demonstrate specific and potent binding affinities to the receptor for most of these substances and showed that CBD could antagonize O-1602 activation[93]. However, classifying GPR55 as a new cannabinoid receptor remains controversial. GPR55 belongs to the class A (rhodopsin-like) family of GPCRs. It lacks the typical binding pocket of the traditional cannabinoid receptors CB1 and CB2 and shares low sequence homology with these 2 receptors of only 13.5 % and 14.4 %, respectively[96,97]. According to the amino acid sequence, GPR55 is more closely related to the receptors GPR35, P2Y5, GPR23/P2Y9, CCR9 and others, sharing 36 %, 31 %, 30 % and 29 % sequence identity, respectively[98].

3.3.1.2 The endogenous ligand lysophosphatidylinositol

In 2007 Oka et al. used transfected HEK293 cells overexpressing GPR55 to identify potent agonists for this receptor. They tested a variety of cannabinoid receptor ligands and lysolipids. As a result, the lipid mediator L-α-lysophosphatidylinositol (LPI) – first described in 1962[99] – was identified as the endogenous and most potent ligand of GPR55[100]. A study detailing the GPR55 binding site shows a selective interaction of the negatively charged head group of LPI with a positively charged residue near the receptor's extracellular loop 2 and the molecule's tail reaching into the transmembrane helices[101]. Taking this and the phylogenetic differences to the classical cannabinoid receptors into account, GPR55 is rather referred to as cannabinoid sensitive receptor instead of being a new member of this family.

Phospholipids are the most abundant component of cell membranes, forming lipid bilayers due to their amphiphilic characteristic. They usually consist of two hydrophobic fatty acid chains and a hydrophilic head containing a negatively charged phosphate group[89]. Phosphatidylinositol (PI) belongs to the class of phosphatidylglycerides and plays a key role in signaling pathways as a bioactive lipid[102]. Phospholipase A1 (PLA1)[103] and phospholipase A2 (PLA2)[104,105] act on the same precursor 1-stearoyl-2-arachidonoyl PI to produce two LPI isomers – 2-arachidonoyl LPI and 1-stearoyl LPI, respectively[106] (Figure 6).

Intracellular PLA1 (also known as DDHD1/phosphatidic acid (PA)-PLA1) is responsible for 2-arachidonoyl LPI formation and is highly coexpressed with GPR55 in the brain. Phospholipase D (PLD) together with PA is needed to regulate the PI-PLA1 activity of DDHD1[106,107] (Figure 6). LPI is released from the cell by the ATP-binding cassette transporter C1. This mechanism was demonstrated *in vitro* using a human prostate cancer cell line[105]. Among different fatty acid species of LPI, 2-arachidonoyl LPI has the highest biological activity on GPR55-expressing HEK293 cells, leading to the assumption that this is the most potent natural ligand for GPR55[108].

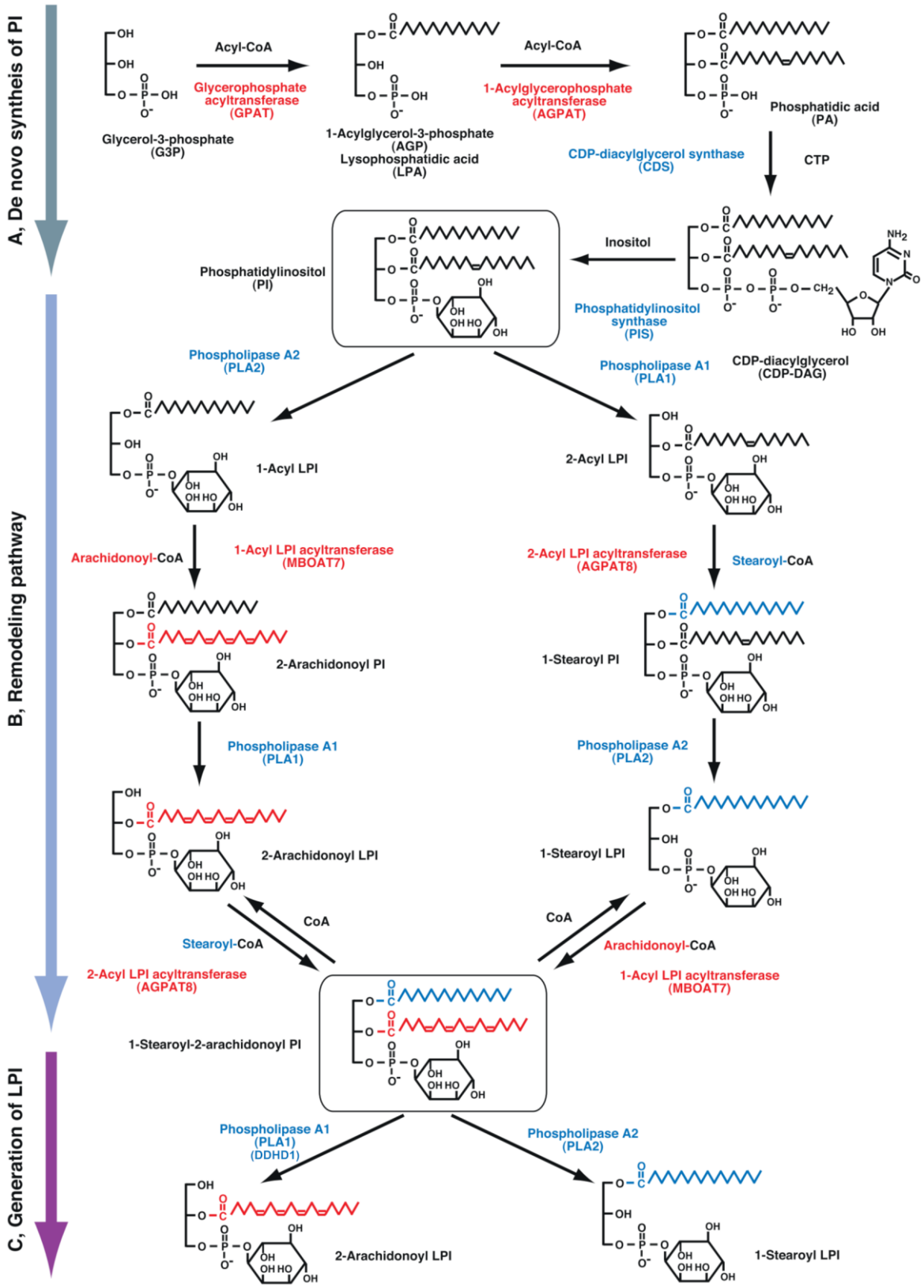

Figure 6: Lysophosphatidylinositol (LPI) synthesis. This chart summarizes the generation of LPI from its precursor molecules. (**A**) Phosphatidic acid (PA) is generated by adding two fatty acids to glycerol-3-phosphate. Incorporating cytidine triphosphate (CTP) and exchanging it for inositol results in the production of phosphatidylinositol (PI). (**B**) Remodeling and integration of different fatty acids into PI leads to the production of the 1-stearoyl-2-arachidonoyl PI. (**C**) From there, the biosynthesis of two different LPI species occurs through DDHD1/PLA1 and PLA2 activity. (Adapted from Yamashita et al.[106])

In order to shut down LPI activity and the subsequent GPR55 signaling cascade, multiple degradation pathways are known so far. Lysophospholipase A (lyso-PLA) deacylates LPI into glycero-PI (GPI) and fatty acids[109]. Another metabolic pathway involves lysophospholipase C (lyso-PLC) activity, which transforms 2-arachidonoyl LPI into the cannabinoid receptor CB1 and CB2 agonist 2-AG, thereby linking GPR55 and endocannabinoid signaling pathways[110,111]. LPI released into the plasma can be converted to lysophosphatidic acid (LPA) such as 2-arachidonoyl LPI, which is further converted to the GPR35 agonist 2-arachidonoyl LPA[112]. Another enzyme that is able to convert LPI to LPA is lysophospholipase D (lyso-PLD/autotaxin), the predominant enzyme-producing LPA[113,114]. These findings link GPR55, GPR35, CB1 and CB2 via the possible interconversions of their lipid messengers. LPI can enter the PI cycle again through the activity of LPI acyltransferases 1 (LPIAT1/MBOAT7) and 1-acylglycerol-3-phosphate acyltransferase 8 (AGPAT8/ALCAT1) (Figure 7)[102,106].

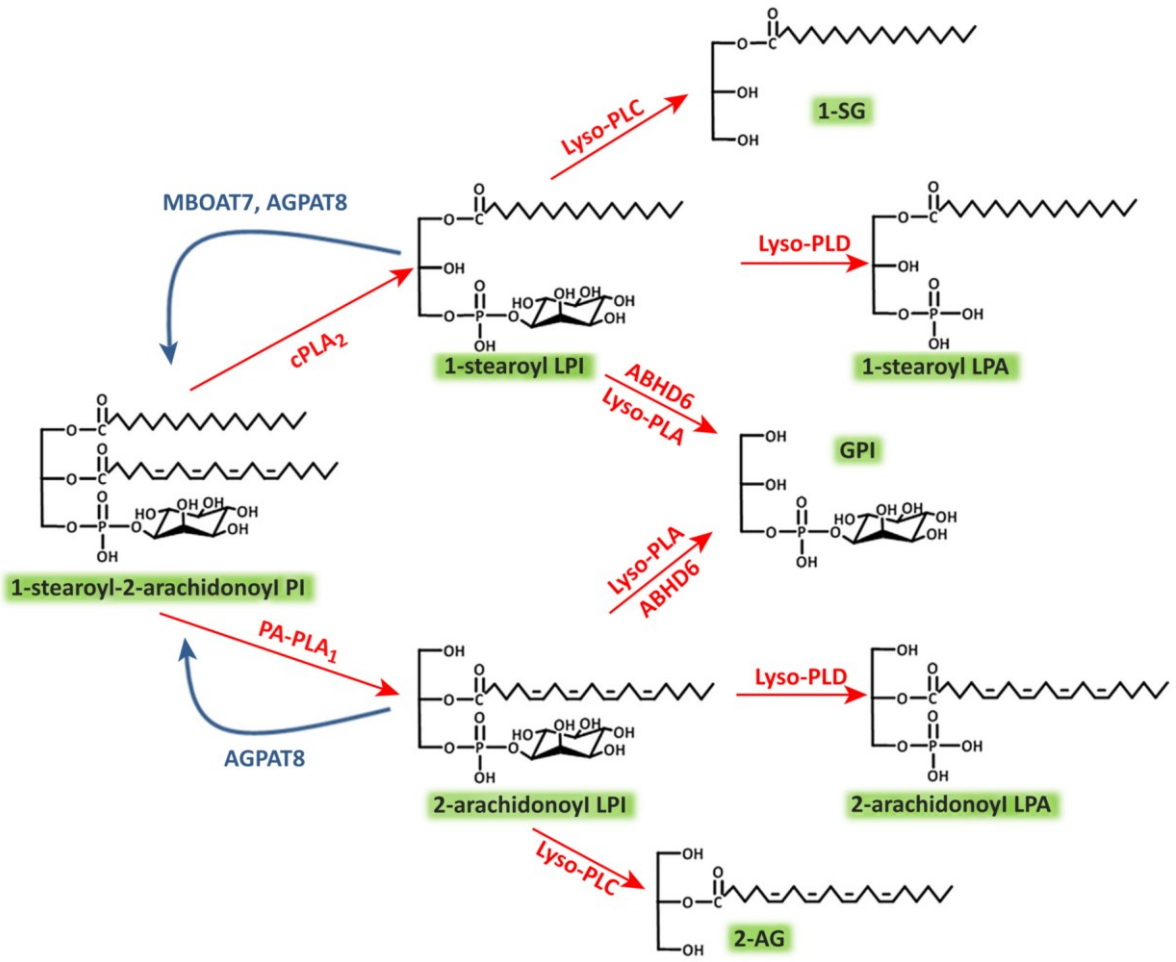

Figure 7: Degradation of lysophosphatidylinositol (LPI).
Different LPI species are released from cell membranes by phospholipase A_2 ($cPLA_2$) and phospholipase A_1 ($PA\text{-}PLA_1$) activity on phosphatidylinositol (PI), forming 1-acyl LPI or 2-acyl LPI, respectively. LPIs can be further metabolized by lysophospholipases A, C and D (Lyso-PLA, Lyso-PLC, Lyso-PLD), resulting in glycerophosphoinositol (GPI), acylglycerols (e.g. 2-AG, 1-SG) and lysophosphatidic acid (LPA). Acyltransferase MBOAT7 and AGPAT8 can reacylate LPI to the parent PI species. (Copied from Alhouayek et al.[102])

When assessing the effects of LPI, non-receptor and receptor-mediated activities can be distinguished. Having a more cone-like shape due to a large head and just one fatty acid, LPI alters the cell membrane by creating a more positive curvature and thus modifies its physical properties[115]. In this way, a multitude of ion channels at the plasma and mitochondrial membrane are influenced[116,117]. The addition of LPI to plasma membranes can affect clathrin-dependent endocytosis by reducing the number of invaginated clathrin-coated pits and reducing overall endocytosis[118]. Besides its effects on GPR55, LPI has been reported to activate a variety of other receptors such as the large-conductance calcium-activated K^+ channels (BKCa)[119], two-pore domain K^+ channels TREK-1 and KCNK4/TRAAK[120], transient receptor potential cation channels TRPV2[121] and TRPM8[122]. These and possibly other not-yet described targets of LPI could be responsible for some of the LPI-mediated effects.

3.3.1.3 GPR55 expression

The measurement of GPR55 at the mRNA or protein level in murine and human tissues revealed a broad expression throughout the whole body. High GPR55 expression was shown in the central nervous system, especially in mouse striatum, caudate nucleus, putamen, hippocampus, frontal cortex, hypothalamus, cerebellum, brain stem, and microglia[90,93,123,124]. The receptor was present in similar regions of rat brains and periaqueductal gray neurons[90,125,126]. Studies in human brain sections showed high expression levels in the basal ganglia, nucleus accumbens, hypothalamus, and hippocampus while the lowest expression levels were recognized in the cerebellum[90,97]. *Gpr55* is also expressed across all segments of the gastrointestinal tract. Murine esophagus, stomach, ileum, jejunum, and colon samples demonstrated *Gpr55* expression[93] and it was specifically found in myenteric neurons in the ileum and colon[127,128]. Studies on rat and human samples affirmed intestine-wide expression and showed its expression in the myenteric plexus as well[128,129]. Pancreatic tissue analysis revealed a rather β-cell-specific protein expression of GPR55 in rodent islets of Langerhans[130], whereas human probes indicate equal expressions in α- and β-cells[131]. Furthermore, *Gpr55* was detected in the adrenal glands, pituitary gland, bone marrow, spleen, adipose tissue, and liver across different species[90,93,97,130] and human visceral and subcutaneous adipose tissue, with increasing levels in obesity and type 2 diabetes mellitus (T2DM)[97,132]. *Gpr55* is highly expressed in lymphoid organs such as the spleen and thymus[133]. Looking at isolated blood cells, the receptor is expressed on neutrophils[134], monocytes, NK cells[135], and platelets[97]. Additionally, the Immunological Genome Project database lists the expression of *Gpr55* in many different leukocytes, with high expression values in B cells and their precursors[136]. In addition, GPR55 expression was confirmed at the mRNA level in human and mouse osteoblasts, osteoclasts, and osteoclast precursors with increasing levels during maturation[137]. *Gpr55* is also detectable in tissues of the cardiovascular system. The receptor was found on human ECs[138] and a fluorescent GPR55 agonist study indicated expression in vascular smooth muscle cells and found that *Gpr55* was expressed in all layers of the mouse

mesenteric artery[139]. *Gpr55* was also validated in rodent heart tissue[140] and isolated cardiomyocytes[141]. Several human tumor cell lines and tissue samples derived from glioblastoma[142], astrocytoma[142], breast[142,143], cervix[142], ovary, prostate[105], lymphoblastoid cells[133,142], liver, pancreas[142] and bile duct[144] express GPR55. In some cases, receptor expression correlates positively with tumor aggressiveness and higher expression in glioblastoma patients was associated with worse survival[142].

3.3.1.4 GPR55 signaling

Over the years, researchers were able to demonstrate GPR55 activation and unveil downstream signaling with a vast array of assays in different cell types, using a range of ligands. Although this led to some conflicting reports about its pharmacology and stimulated debate about its classification as a cannabinoid receptor, the downstream signaling cascade followed by GPR55 activation is well described (Figure 8). HEK293 cells overexpressing human GPR55 are the most frequent model employed in these studies. $G_{\alpha 13}$ coupling was reported after agonist activity at GPR55 accompanied by the activation of the small GTPases Ras homolog family member A (RhoA), Cell division control protein 42 homolog (Cdc42) and Ras-related C3 botulinum toxin substrate 1 (Rac1)[93]. Henstridge et al. and others were able to confirm $G_{\alpha 13}$ coupling and saw an oscillatory Ca^{2+} release following RhoA and subsequent Rho-associated protein kinase (ROCK) activation, which ultimately led to activation of the transcription factor nuclear factor of activated T cells (NFAT)[145]. Another group demonstrated PLCβ activation via $G_{\alpha q}$ coupling and a Ca^{2+} release from the endoplasmatic reticulum (ER), which was mediated by inositol 1,4,5-triphosphate (IP_3) sensitive channels. This Ca^{2+} release required $G_{\alpha 12}$ coupling with a subsequent RhoA activation and an intact actin cytoskeleton[125]. Upon stimulation with LPI, internalization of the receptor[145] and downregulation controlled by GPCR-associated sorting protein-1 was detected[146]. A wide variety of *in vitro* models using HEK293 cells overexpressing GPR55[100,133,147,148], osteoclasts[137], and different cancer cell lines[105,142,148] identified extracellular signal-regulated kinase 1/2 (ERK1/2) phosphorylation as a main cellular target of GPR55. Upon activation, the ERK cascade leads to the phosphorylation of a wide variety of proteins and transcription factors, impacting many different cellular processes. LPI also induced a time- and concentration-dependent phosphorylation of p38 mitogen-activated protein kinase (MAPK) and triggered downstream phosphorylation of activating transcription factor 2 (ATF-2) in HEK293 cells overexpressing GPR55 as well as IM-9 lymphoblastoid cells naturally expressing the receptor[133]. Again, this was only possible through RhoA/ROCK pathway activation but independent of ERK. In summary, GPR55 couples to $G_{\alpha 12/13}$ and $G_{\alpha q,}$ which results in the activation of RhoA, ROCK, ERK1/2, p38 MAPK, and PLC. This leads to an IP_3-mediated Ca^{2+} release from the ER, inducing transcription factors like NFAT, nuclear factor kappa-light-chain enhancer of activated B cell (NF-κB), ETS variant transcription factor 4 (ETV4), cyclic adenosine monophosphate (cAMP) responsive element-binding protein 1 (CREB), and ATF-2. Differences in the activation patterns depend on the specific agonist binding to

GPR55. These pathways are involved in the regulation of a variety of cellular functions like innate and adaptive immune response, neuronal plasticity, embryogenesis, cell transformation, cell differentiation, and cell survival with deregulated cascades associated with tumorigenesis.

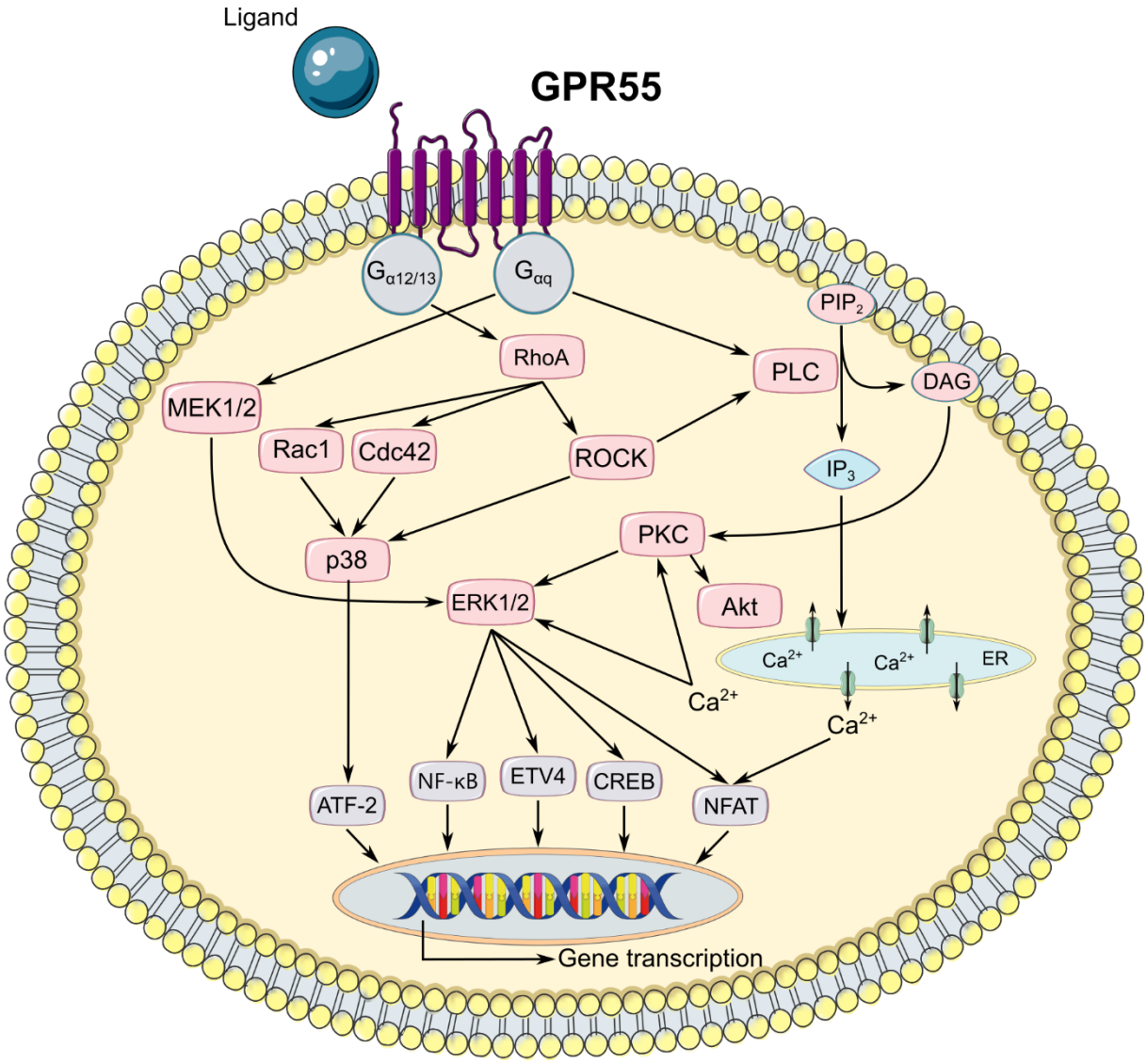

Figure 8: Postulated intracellular signaling pathway of GPR55.
This schematic illustrates downstream pathways following GPR55 activation by an agonist such as lysophosphatidylinositol (LPI). $G_{\alpha 13}$ activation triggers Ras homolog family member A / Rho-associated protein kinase (RhoA/ROCK) dependent release of Ca^{2+} from the endoplasmatic reticulum (ER). This leads to extracellular signal-reduced kinase (ERK) 1/2 phosphorylation with subsequent activation of transcription factors (ATF-2, NF-κB, ETV4, CREB, and NFAT) and thus changes in gene transcription. ROCK causes p38 mitogen-activated protein kinase (MAPK) phosphorylation, which also results in transcription factor activation. $G_{\alpha q}$ coupling leads to phospholipase C (PLC) mediated inositol triphosphate (IP_3) generation, enabling the release of Ca^{2+} from the ER, leading to ERK1/2 phosphorylation.

3.3.2 Role of GPR55 in physiology and pathophysiology

Due to its wide expression within the body, GPR55 has drawn a lot of attention in recent years. An increasing number of studies have been published, focusing on its role in physiology and disease. This chapter summarizes the main functions of GPR55 that have been explored so far (Figure 9).

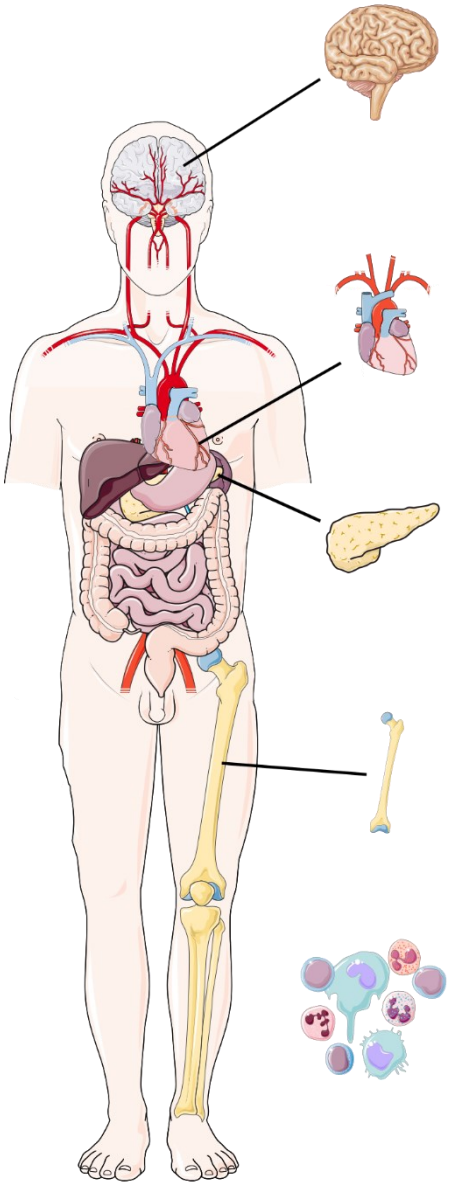

Nervous system

- Antinociceptive effects in inflammatory and mechanical pain *(Staton et al., 2008[149]; Schuelert et al., 2011[150])*
- Pronociceptive in PAG neurons *(Deliu et al., 2015[126])*
- GPR55 polymorphism linked with anorexia nervosa *(Ishiguro et al., 2011[151])*
- Impaired movement coordination in *Gpr55*$^{-/-}$ mice *(Wu et al., 2013[123])*

Cardiovascular system

- Cardiomyopathy in *Gpr55*$^{-/-}$ mice *(Walsh et al., 2014[140])*
- Unstable atherosclerotic plaques due to antagonist treatment *(Montecucco et al., 2016[152])*
- Infarct size increase upon GPR55 activation *(Robertson-Gray et al., 2019[153])*
- Impaired left ventricular remodeling after myocardial infarction in *Gpr55*$^{-/-}$ mice *(Puhl et al., 2021[154])*

Metabolism

- Increase in insulin secretion *(Romero-Zerbo et al., 2011[130]; McKillop et al., 2013[155])*
- Association with obesity *(Moreno-Navarrete et al., 2012[132])*
- Role in energy homeostasis, adiposity and insulin resistance *(Meadows et al., 2016[156])*

Bone

- Stimulation of osteoclast polarization and bone resorption *(Whyte et al., 2009[137])*

Cancer

- Procancerogenic role in various cancer types *(Andradas et al., 2011[142]; Piñeiro et al., 2011[105]; Pérez-Gómez et al., 2013[157])*

Inflammation

- Regulation of neutrophil migration and function *(Balenga et al., 2011[134])*
- Proinflammatory role in neutrophils, monocytes and NK cells *(Chiurchiù et al., 2015[135])*
- Increase in inflammation and lipid accumulation in foam cells *(Lanuti et al., 2015[158])*
- Reduced severity of experimental intestinal inflammation *(Stančić et al., 2015[159])*
- GPR55 activation inhibits intraepithelial lymphocyte migration, antagonism protects from intestinal damage *(Sumida et al., 2017[160])*

Figure 9: Overview of GPR55 in physiology and pathophysiology.
Studies demonstrated the importance of GPR55 in various physiological and pathophysiological functions, summarized in this chart.

3.3.2.1 GPR55 plays a role in metabolism and type 2 diabetes mellitus

Long before GPR55 was identified as the specific receptor for LPI, Metz et al. suggested that LPI and other lysophospholipids might be involved in mechanisms regulating metabolism and insulin release[161]. Isolated rat islets of Langerhans were stimulated with LPI to release insulin in a dose-dependent, saturable and reversible manner, which did not affect the overall function of the islets. This was accompanied by the mobilization of Ca^{2+} [161,162]. More recent studies confirmed high β-cell-specific expression of *Gpr55* in rodent islets of Langerhans and substantiated the metabolic role of GPR55 *in vivo*. Activation of GPR55 increased insulin levels and glucose tolerance in WT but not *Gpr55*$^{-/-}$ animals[130,155]. Treatment of an insulin-secreting cell line and isolated mouse islets with a range of GPR55 agonists enhanced insulin release as well as intracellular Ca^{2+} concentration and cAMP release, which was blunted by the antagonist CBD[155]. McCloskey et al. further addressed the question of whether GPR55 can be considered an anti-diabetic target[163]. After demonstrating that synthetic (abnormal cannabidiol, AM251, O-1602) and endogenous (Oleoylethanolamine, PEA) GPR55 ligands stimulated insulin secretion in human and rodent WT β-cells, a rodent *Gpr55*$^{-/-}$ β-cell line was generated using CRISPR/Cas9 gene editing. The insulinotropic effect of various ligands was markedly reduced when treating the *Gpr55*$^{-/-}$ cell line. Treating a diabetic mouse on a high fat diet (HFD) with abnormal cannabidiol confirmed glucose-lowering and insulin-releasing effects *in vivo*[163]. These results emphasize the importance of GPR55 in β-cells and its ability to improve glucose homeostasis via insulin secretion[130,163].

In agreement with the above-mentioned studies, Meadows et al. observed enhanced insulin resistance, increased body weight and fat mass in *Gpr55*$^{-/-}$ mice, which the authors linked to a decrease in physical activity[156]. Another recent study confirmed these findings. They detected a similar increase in body mass, as well as a reduction of physical activity, combined with impaired insulin sensitivity in *Gpr55*$^{-/-}$ animals[164]. *In vivo* and *in vitro* experiments in metabolically active tissues (liver, skeletal muscle, adipose tissue and cell lines derived from these tissues) showed impaired insulin signaling when *Gpr55* was knocked out. In a variety of settings, GPR55 activation led to enhanced insulin signaling, whereas antagonist treatment or genetic knockout resulted in dysfunctional signaling and an increase in the expression of lipogenic proteins[164].

In humans, *GPR55* mRNA expression was elevated in subcutaneous and visceral adipose tissue of obese subjects and even higher in patients with T2DM compared to lean controls[132]. Moreno-Navarrete et al. found that *Gpr55* expression also positively correlated with body mass index in both sexes and with body weight and fat mass in women. Plasma LPI levels in women increased with obesity and positively correlated with body weight, fat mass, and blood LDL. *In vitro* experiments conducted with human visceral adipose tissue explants support the regulatory effects of the LPI/GPR55 system. LPI increased *GPR55* mRNA levels and triggered the expression of genes promoting fat deposition and adipocyte differentiation[132]. However, *Gpr55* mRNA and protein levels were decreased in obese rodent animal models. This is in

contrast to findings in human tissues, which indicate a different regulation of the receptor in rodents[132].

Ibernon et al. analyzed the regulation of *Gpr55* mRNA expression in rat WAT and measured the amount of circulating LPI in various metabolic conditions. They tested for nutritional status, age, gender, sex hormone levels, pregnancy, and pituitary function. All these parameters were correlated with the LPI/GPR55 system, and thus, GPR55 might be a potential target for future treatment strategies in metabolic disorders[165].

3.3.2.2 GPR55 regulates osteoclast function

Gpr55 is expressed in both human and murine osteoblasts and osteoclasts with increasing mRNA levels during osteoclast differentiation. Upon GPR55 activation, *in vitro* formation of murine osteoclasts was inhibited and the resorptive activity of human and murine osteoclasts increased. These effects were diminished by CBD and absent in *Gpr55*$^{-/-}$ cells. Treatment with CBD alone resulted in overall less polarization and resorption in cultured osteoclasts. Besides, male *Gpr55*$^{-/-}$ mice developed an increased bone volume accompanied by more but functionally impaired osteoclasts[137]. CBD was also important for the migration to sites of bone remodeling and osteogenic differentiation of human mesenchymal stem cells (MSCs) via activation of CB2 receptor and inhibition of GPR55 – an effect mediated via p42/44 MAPK activation. Activation of GPR55 reduced the CBD-induced effects, whereas the GPR55 antagonist O-1918 could enhance p42/44 MAPK activation and MSC migration[166]. GPR55 seems to play an essential role in both osteoclastogenesis and regulation of their resorptive activity.

3.3.2.3 GPR55 modifies nociception

As mentioned above, GPR55 is expressed in the central nervous system and has been shown to modulate nociception. *Gpr55*$^{-/-}$ mice exhibited significantly less hyperalgesia compared to the WT control group in a model for inflammatory mechanical hyperalgesia in mice. In addition, a partial sciatic nerve ligation model for neuropathic pain demonstrated the total absence of hyperalgesia in the *Gpr55*$^{-/-}$ animals[149]. Breen et al. showed that the GPR55 agonist O-1602 aggravated neuropathic pain[167]. Contradictory to these results, data of another group indicated no differences between *Gpr55*$^{-/-}$ and WT mice in a similar experimental setting[168]. The hot-plate test revealed a reduced withdrawal latency in female but not in male *Gpr55*$^{-/-}$ mice compared to WT[123,149]. Injecting LPI in the periaqueductal grey region reduced the paw withdrawal latency in rats. Injection of the GPR55 antagonist mL193 counteracted these observations, promoting a pain-intensifying action of GPR55[126]. In this case, GPR55 activation amplified the animal's reaction to pain, whereas another group pointed out that O-1602 treatment reduced pain in a rat model for

acute joint inflammation in a GPR55-dependent mechanism[150]. Injecting LPI into mice paws resulted in mechanical hyperalgesia. This effect as well as long-term hyperalgesia were more pronounced in WT animals than *Gpr55*$^{-/-}$. In a soft tissue tumor model for induced cancer pain, *Gpr55*$^{-/-}$ mice exhibited a reduced pain response to the tumor mass in comparison to WT littermates. LPI seemed to facilitate its pro-nociceptive actions via $G_{\alpha 13}$ and subsequent ERK1/2 activation, which was not solely dependent on GPR55 signaling[169]. These findings advocate that LPI and GPR55 signaling is involved in nociception and might be a possible target for novel analgesic treatment strategies. However, in some cases, studies report inconsistent effects. This could be due to the experimental models used. In addition, the unspecific binding properties of the ligands used in these studies make it difficult to determine GPR55-specific effects.

3.3.2.4 GPR55 plays a role in inflammation

As mentioned above, GPR55 is expressed on a range of immune cells and its mRNA expression can be modulated by inflammatory stimuli[124,129,135]. A mouse model of induced colitis suggested proinflammatory properties of activated GPR55, since colitis was milder in *Gpr55*$^{-/-}$ animals[127,159]. Treatment with a GPR55 antagonist led to reduced disease severity scores and lowered the number of proinflammatory cytokines in the tissue due to reduced lymphocyte and macrophage infiltration in the colon[159]. GPR55 deficiency reduced indomethacin-induced intestinal damage, possibly by a regulatory function on intraepithelial lymphocytes. Treating GPR55-overexpressing lymphocytes with LPI resulted in inhibition of their migration towards a chemoattractant[160]. *In vitro* experiments with LPS-activated monocytes and activated NK cells support the proposed proinflammatory nature of GPR55. Treatment with O-1602 triggered interleukin-12 (IL-12) and TNF-α production in monocytes and increased cytokine production and cytotoxicity in NK cells[135]. Stimulation of foam cells with O-1602 also favored a proinflammatory cytokine profile with increased TNF-α and reduced anti-inflammatory interleukin-10 (IL-10) mRNA expression compared to untreated cells[158]. McHugh et al. postulated the existence of a non-CB1 and non-CB2 receptor, possibly GPR55, susceptible to various cannabinoid ligands that contributes to the potent inhibitory properties of cannabinoid ligands on human neutrophil migration[170]. The addition of CID16020046 to a naturally GPR55 expressing mouse macrophage cell line (J774A.1) and isolated human neutrophils markedly reduced cell migration in both cell types towards chemoattractants[159]. Furthermore, this reduced the expression of CD11b in macrophages. Balenga et al. found that activation of GPR55 increased human neutrophil migration while limiting degranulation and a CB2 receptor-mediated respiratory burst[134]. These findings suggest a complex interaction between CB2 receptor and GPR55 in neutrophil regulation[134]. Mast cells challenged with an inflammatory agent produce nerve growth factor (NGF), a neurotrophin also involved in inflammatory processes. The production of NGF was blunted by PEA in a GPR55-dependent mechanism[171].

3.3.2.5 GPR55 activation is associated with cancerogenic effects

GPR55 and its endogenous ligand LPI have also been extensively studied in oncology. As mentioned before, a variety of human cancer cell lines express *Gpr55* mRNA. LPI showed potent mitogenic activity in *in vitro* models. Ras-transformed thyroid cells had increased PLA2 activity leading to increased LPI production, which stimulated cell proliferation[172–174]. Plasma LPI levels were higher in patients with ovarian cancer[175], suggesting – together with other lysophospholipids – that it is a potential biomarker in this disease[176]. *In vitro* experiments revealed a proliferative role of LPI and GPR55 in ovarian and prostate cancer cells[105]. Intracellularly synthesized LPI was released into the medium and induced cell proliferation via GPR55. Downregulation of LPI synthesizing and releasing enzymes or direct downregulation of GPR55 inhibited cell proliferation, which could not be restored by the addition of extracellular LPI, indicating that enhanced cell proliferation is directly caused by LPI/GPR55 interaction[105]. Andradas et al. illustrated a correlation between GPR55 expression and tumor aggressiveness in different human cancer samples[142]. When *Gpr55* was knocked down, tumor cell viability was impaired. Instead, overexpression resulted in better cell viability in glioma and pancreatic adenocarcinoma cell lines[142]. Another study found improved migration of breast cancer cells when GPR55 was overexpressed[143]. A study in mice showed better resistance of *Gpr55*$^{-/-}$ mice in a model of chemically induced skin tumors compared to WT control animals. The authors also confirmed enhanced expression of GPR55 in malignant cells compared to normal skin[157]. Overall, this information demonstrates the carcinogenic role of GPR55.

3.3.2.6 GPR55 in cardiovascular disease and atherosclerosis

Since GPR55 is involved in inflammatory processes and is expressed in arteries[138,139] and a variety of immune cells[134–136], it might be involved in the chronic inflammatory process during atherosclerosis. Accumulation of oxLDL in the endothelium is one of the key mechanisms driving atherogenesis[6]. *In vitro* experiments revealed upregulation of GPR55 expression in foam cells compared to macrophages and an increase in intracellular lipid content when treated with GPR55 agonists. Protein expression of the scavenger receptors CD36 and SR-B1 was increased in oxLDL-treated foam cells and raised even further by simultaneous activation of GPR55 with O-1602. Additionally, this treatment elicited a proinflammatory phenotype with an increase in IL-12 and TNF-α and a decrease in IL-10 cytokine levels combined with down-regulation of the cholesterol transporters ABCA1 and ABCG1. Most of these findings are likely due to GPR55 activity since CBD treatment counteracted the majority of these effects[158].

Antagonizing GPR55 by chronic intraperitoneal injection of CID1602004 in an *Apoe*$^{-/-}$ mouse model failed to affect overall plaque burden but led to a more unstable plaque phenotype with increased MMP-9 and reduced collagen content. Notable effects were elevated levels of circulating and aortic chemokines responsible for neutrophil

recruitment as well as enhanced neutrophil degranulation[152]. Another group performed a similar experiment, using a two-fold higher dose of CID1602004 and a more extended treatment period. They showed a reduction in aortic root plaque burden due to the antagonist treatment[177].

Also, the effects of PEA treatment in the *Apoe*$^{-/-}$ mouse model during early and advanced stages of atherosclerosis were studied. PEA acts via Peroxisome proliferator-activated receptor α or GPR55 with mainly anti-inflammatory effects[93,178]. In the early stage, PEA reduced plaque formation. In the advanced stages, PEA-treated mice displayed higher intra-plaque macrophage content with more collagen and smaller necrotic core size, thus developing more stable plaques. PEA treatment resulted in an anti-inflammatory phenotype. The assessment of mRNA expression levels of inflammatory markers in aortic tissue showed significant decreases compared to vehicle-treated mice. Stimulating bone marrow-derived macrophages (BMDM) obtained from WT animals with PEA led to enhanced expression of proto-oncogene Myeloid-epithelial-reproductive tyrosine kinase (MerTK), a protein involved in macrophage efferocytosis, and increased phagocytotic activity. This effect was absent in *Gpr55*$^{-/-}$ cells, clearly indicating a GPR55-mediated effect of PEA[178]. Pharmacological activation of GPR55 using O-1602 induced *Mac1* overexpression and resulted in better monocyte adhesion in an *in vitro* assay[177].

GPR55 is expressed in cardiomyocytes and a study on cardiac function demonstrated severe adverse ventricular remodeling and systolic dysfunction in aged *Gpr55*$^{-/-}$ mice. In particular, 32 weeks old *Gpr55*$^{-/-}$ mice showed cardiomyopathy with attenuated ventricular contractility due to thinned ventricles with fewer cardiomyocytes and an increase in collagen deposition[140]. A previous study conducted in our lab explored the role of GPR55 in myocardial infarction following permanent LAD ligation in a mouse model. The colleagues illustrated the impact of GPR55 in cardiomyocyte morphology and signaling. They observed an altered inflammatory response after myocardial infarction, ultimately leading to impaired left ventricular remodeling in global *Gpr55*$^{-/-}$ mice[154]. In a mouse model of global ischemia and subsequent reperfusion, LPI treatment increased infarct size in WT mice in a GPR55-dependent manner via RhoA, ROCK, and p38 MAPK activation. This effect on infarct size was absent in *Gpr55*$^{-/-}$ mice. This suggests that elevated LPI levels could lead to worse outcomes in patients with acute coronary syndrome (ACS)[153]. In an *in vivo* ischemia/reperfusion model in rats, treatment with the GPR55 antagonist CBD resulted in cardioprotective effects through reduced arrhythmias and reduced infarct sizes[179]. In rats subjected to asphyxia-induced cardiac arrest, LPI levels were found to be increased in the heart, brain, liver and kidney[180]. In support of potential relevance for LPI-GPR55 signaling in human pathophysiology, LPI release by platelets was increased in the coronary arteries of patients with ACS[181].

3.4 Aim of the study

Atherosclerosis and related acute cardiovascular diseases are the leading cause of death worldwide. A better understanding of the disease and underlying inflammatory signaling pathways may help identify future treatment strategies. GPR55 signaling is involved in a variety of physiological and pathophysiological conditions, particularly those connected to cardiovascular risk factors such as obesity and metabolic syndrome. GPR55 modifies the behavior of leukocytes in inflammatory conditions and *in vitro* studies hint toward an influence on foam cell functions in atherosclerosis. Whether GPR55 directly modulates the pathogenesis of atherosclerosis and by which precise cellular mechanisms is still largely unknown.

This thesis aimed to study the role of GPR55 in atherosclerosis. Therefore, the *Apoe*$^{-/-}$ model of atherosclerosis was crossed with mice globally lacking *Gpr55*. The resulting *Apoe*$^{-/-}$*Gpr55*$^{-/-}$ double knockout mice were used to study atherosclerotic plaque development and metabolic and inflammatory changes compared to *Apoe*$^{-/-}$ controls. These experiments will help to shed light on the role of GPR55 in the pathophysiology of atherosclerosis and may provide the basis for further studies to dissect the cell-specific effects of GPR55 signaling in immune cells, adipose tissue, and the liver.

4 MATERIALS AND METHODS

4.1 Materials

4.1.1 Consumables

Table 1: Consumables

Material	Company
1.3 mL EDTA micro tubes	Sarstedt AG & Co, Nümbrecht, Germany
12-well polystyrene microplate	Corning Inc., NY, USA
8-well PCR Tube Strips 0.2 mL with Domed Cap Strips	NIPPON Genetics EUROPE GmbH, Düren, Germany
50 µm cell strainer	Sysmex K.K., Kobe, Japan
70-µm cell strainer	Corning Inc., Corning, NY, USA
96-well black clear bottom microplate	PerkinElmer Inc., Waltham, MA, USA
96-well half area flat bottom microplate	Corning Inc., Corning, NY, USA
96-well white clear bottom microplate	PerkinElmer Inc., Waltham, MA, USA
Falcon® 5 mL Round Bottom Polystyrene Test Tube	Corning Inc., Corning, NY, USA
Falcon® 5 mL Round Bottom Polystyrene Test Tube, with Cell Strainer Snap	Corning Inc., Corning, NY, USA
Microlance needles (23 G, 30 G)	BD Bioscience, San Jose, CA, USA
PAP-Pen	Kisker Biotech GmbH & Co. KG, Steinfurt, Germany
Qiagen TissueLyser steel beads	Qiagen, Hilden, Germany
Rotatable cell scraper (20 mm)	TPP Techno Plastic Products AG, Trasadingen, Switzerland
Safety scalpel	B. Braun AG, Puchheim, Germany
Semi-skirted 96-well qPCR plates	VWR International, Radnor, USA
Superfrost Plus microscope slides	Menzel-Gläser GmbH, Braunschweig, Germany
TipOne® Pipette Tips (10 µL, 200 µL, 1000 µL)	Starlab International GmbH, Hamburg, Germany
Tissue-Tek cryomold	Sakura Finetek Germany GmbH, Staufen, Germany
Western diet TD.88137 (21 % fat, 0.21 % cholesterol)	Ssniff Spezialdiäten GmBH, Soest, Germany
White adhesive bottom seal	PerkinElmer Inc., Waltham, MA, USA

4.1.2 Equipment

Table 2: Equipment

Equipment	Company
7900 HT Fast Real-Time PCR System	Applied Biosystems, Foster City, CA, USA
Analytical Balance Talent TE124S	Sartorius AG, Göttingen, Germany
Autoclave LTA 400	Zirbus technology GmbH, Bad Grund, Germany
Balance SE 203 LR	VWR International, Radnor, PA, USA
Centrifuge 5418 R	Eppendorf AG, Hamburg, Germany
Centrifuge 5810 R	Eppendorf AG, Hamburg, Germany
CO_2 Incubator CB 160	BINDER GmbH, Tuttlingen, Germany
Cryotome CM3050S	Leica Biosystems, Wetzlar, Germany
FACS Aria III Cell Sorter	BD Bioscience, San Jose, CA, USA
FACS Canto II Flow Cytometer	BD Bioscience, San Jose, CA, USA
Hood HERAsafe	Heraeus, Hanau, Germany
Infinite F200 Pro	Tecan Trading AG, Männedorf, Swizerland
Laboratory pH Meter 766	Knick GmbH, Berlin, Germany
LEICA DM6000	Leica Biosystems, Wetzlar, Germany
LEICA DMi1	Leica Biosystems, Wetzlar, Germany
LEICA DMLB	Leica Biosystems, Wetzlar, Germany
LEICA DMRBE	Leica Biosystems, Wetzlar, Germany
LifeSep Magnetic Plate Holder 96F	Sigma-Aldrich Chemie GmbH, Munich, Germany
LSR Fortessa Flow Cytometer	BD Bioscience, San Jose, CA, USA
Luminex MAGPIX Instrument	Luminex, Austin, TX, USA
Megafuge 1.0 R	Heraeus, Hanau, Germany
Nanodrop ND1000 Peqlab	VWR International, Radnor, PA, USA
Olympus BX51	Olympus Corporation, Tokyo, Japan
PCR Plate Spinners	VWR International, Radnor, PA, USA
PCR Thermocycler Biometra Tpersonal	Biometra GmbH, Göttingen, Germany
Primus 25 advanced Thermocycler	Peqlab Biotechnologie GmbH, Erlangen, Germany
Safire II microplate reader	Tecan Trading AG, Männedorf, Swizerland
Scil Vet ABC Hematology Analyzer	Scil Animal Care Company, Gurnee, IL, USA
The Scepter™ 2.0 Handheld Automated Cell Counter	Merck Millipore, Billerica, MA, USA
Thermomixer F1.5	Eppendorf AG, Hamburg, Germany
TissueLyser LT	Qiagen, Hilden, Germany
Water Purification System Milli-Q	Merck Millipore, Billerica, MA, USA

4.1.3 Software

Table 3: Software

Software	Company
BD FACSDiva software	BD Bioscience, San Jose, CA, USA
FlowJo v10.3	Tree Star, Inc., OR, USA
GraphPad Prism 8.00	GraphPad Software Inc, San Diego, CA, USA
LAS V4.3	Leica Biosystems, Wetzlar, Germany
ProcartaPlex Analyst 1.0	Thermo Fisher Scientific, Waltham, MA, USA
SDS2.4 Software	Applied Biosystems, Foster City, CA, USA
xPONENT Software	Luminex, Austin, TX, USA
AutoStitch	Matthew Brown, David Lowe, University of British Columbia, Vancouver, Canada
Microsoft Excel 2016	Microsoft Corporation, Redmond, WA, USA

4.1.4 Kits

Table 4: Kits

Kit	Company
Antibody Isotyping 7-Plex Mouse ProcartaPlex™ Panel 1	Thermo Fisher Scientific, Waltham, MA, USA
CD3ε MicroBead Kit, mouse	Miltenyi Biotec GmbH, Bergisch Gladbach, Germany
CD19 MicroBeads, mouse	Miltenyi Biotec GmbH, Bergisch Gladbach, Germany
Cholesterol CHOD-PAP kit with Calibrator	Roche, Basel, Switzerland
Cytotoxicity Detection Kit (LDH)	Roche, Basel, Switzerland
ReliaPrep™ gDNA Tissue Miniprep System	Promega Corporation, Madison, WI, USA
GoTaq® qPCR Master Mix	Promega Corporation, Madison, WI, USA
KAPA PROBE FAST Universal qPCR kit	Peqlab Biotechnologie GmbH, Erlangen, Germany
NK Cell Isolation Kit II, mouse	Miltenyi Biotec GmbH, Bergisch Gladbach, Germany
peqGOLD Total RNA kit	Peqlab Biotechnologie GmbH, Erlangen, Germany
PrimeScript RT Reagent kit	Takara Bio Inc., Kusatsu, Japan

4.1.5 Chemicals and reagents

Table 5: Chemicals and reagents

Reagent	Company
1 kb Plus DNA ladder	Thermo Fisher Scientific, Waltham, MA, USA
2-Methylbutane	Sigma-Aldrich Chemie GmbH, Munich, Germany
2-Propanol	Sigma-Aldrich Chemie GmbH, Munich, Germany
Acetic acid 99-100 %	Merck KgaA, Darmstadt, Germany
Agarose	Sigma-Aldrich Chemie GmbH, Munich, Germany
Albumin	Carl Roth GmbH + Co. KG, Karlsruhe, Germany
Ampicillin	Sigma-Aldrich Chemie GmbH, Munich, Germany
Aniline Blue diammonium salt	Sigma-Aldrich Chemie GmbH, Munich, Germany
Aqua ad injectabilia	B. Braun AG, Puchheim, Germany
Biebrich scarlet-acid fuchsin solution	Sigma-Aldrich Chemie GmbH, Munich, Germany
Bouin's solution	Sigma-Aldrich Chemie GmbH, Munich, Germany
Citric acid	Merck KGaA, Darmstadt, Germany
Collagenase I	Sigma-Aldrich Chemie GmbH, Munich, Germany
Collagenase IX	Sigma-Aldrich Chemie GmbH, Munich, Germany
CountBright absolute counting beads	Thermo Fisher Scientific, Waltham, MA, USA
Deoxyribonuclease	Roche, Basel, Switzerland
Dimethylsulfoxid (DMSO)	Carl Roth GmbH + Co. KG, Karlsruhe, Germany
Dulbecco's modified eagle medium (DMEM)	Thermo Fisher Scientific, Waltham, MA, USA
Ethylenediaminetetraacetic acid (EDTA)	Sigma-Aldrich Chemie GmbH, Munich, Germany
Entellan	Sigma-Aldrich Chemie GmbH, Munich, Germany
Ethanol 99 %	Klinikum der Universität München, Munich, Germany
Ethanol 99 % (absolute)	VWR International, Radnor, PA, USA
Ethidium bromide	Sigma-Aldrich Chemie GmbH, Munich, Germany
Fetal bovine serum (FBS)	Sigma-Aldrich Chemie GmbH, Munich, Germany
Gelatine from porcine skin	Sigma-Aldrich Chemie GmbH, Munich, Germany
Glycerine	Carl Roth GmbH + Co. KG, Karlsruhe, Germany
Hank's balanced salt solution (HBSS) with Ca^{2+}/Mg^{2+} (10x)	Thermo Fisher Scientific, Waltham, MA, USA
Hematoxylin solution according to Mayer	Sigma-Aldrich Chemie GmbH, Munich, Germany
4-(2-hydroxyethyl)-1-piperazineethanesulfonic acid (HEPES) solution 1 M	Sigma-Aldrich Chemie GmbH, Munich, Germany
Hoechst 33342	Thermo Fisher Scientific, Waltham, MA, USA
Human Dil High Oxidized Low Density Lipoprotein	KALEN Biomedical, LLC, Germantown, MD, USA

Hyaluronidase I	Sigma-Aldrich Chemie GmbH, Munich, Germany
Immu-Mount	Thermo Fisher Scientific, Waltham, MA, USA
Ketamine	WDT eG, Garbsen, Germany
L-Glutamine	Thermo Fisher Scientific, Waltham, MA, USA
Non-Essential Amino Acids Solution	Thermo Fisher Scientific, Waltham, MA, USA
Nuclease-free water	Promega Corporation, Madison, WI, USA
Oil Red O	Sigma-Aldrich Chemie GmbH, Munich, Germany
Paraformaldehyde	Merck KgaA, Darmstadt, Germany
Phosphate buffered saline (PBS) Dulbecco	Biochrom GmbH, Berlin, Germany
Penicillin-Streptomycin	Sigma-Aldrich Chemie GmbH, Munich, Germany
PeqGold Trifast	Peqlab Biotechnologie GmbH, Erlangen, Germany
Phosphomolybdic acid solution 10 %	Sigma-Aldrich Chemie GmbH, Munich, Germany
Phosphotungstic acid solution 10 %	Sigma-Aldrich Chemie GmbH, Munich, Germany
Picric acid solution	Sigma-Aldrich Chemie GmbH, Munich, Germany
Purified Rat Anti-Mouse CD335 (NKp46) Clone 29A1.4	BD Bioscience, San Jose, CA, USA
Recombinant Mouse IL-2 Protein	R&D Systems, Minneapolis, MN, USA
Roti-Histofix 4 %	Carl Roth GmbH + Co. KG, Karlsruhe, Germany
Roswell Park Memorial Institute (RPMI) 1640 Medium	Thermo Fisher Scientific, Waltham, MA, USA
Sodium pyruvate	Thermo Fisher Scientific, Waltham, MA, USA
Tris-acetate-EDTA (TAE) buffer (50X)	AppliChem GmbH Darmstadt, Germany
Tissue-Tek O.C.T. Compound	Sakura Finetek Germany GmbH, Staufen, Germany
Tween 20	Sigma-Aldrich Chemie GmbH, Munich, Germany
Weigert's iron hematoxylin solution	Merck KgaA, Darmstadt, Germany
Xylazine	WDT eG, Garbsen, Germany
Xylene	Sigma-Aldrich Chemie GmbH, Munich, Germany

4.1.6 Buffers and solutions

Table 6: Buffers, solutions and their composition

Buffer	**Composition**
1x Tris-acetate EDTA (TAE) buffer	50x TAE diluted in H_2O
Ammonium-Chloride-Potassium	150 mM NH_4Cl,

(ACK) lysing buffer	10 mM $KHCO_3$, 0.1 mM Na_2EDTA, pH 7.4
Aorta digestion cocktail	0.45 U/µL Collagenase I, 0.125 U/µL Collagenase XI, 0.06 U/µL Hyaluronidase I, 0.06 U/µL Deoxyribonuclease I, 20mM HEPES buffer in PBS
Blocking solution	1 % bovine serum albumin (BSA), 3 % fetal bovine serum (FBS) in PBS
Citrate buffer	1.4 mM citric acid, 5.74 mM sodium citrate tribasic dihydrate, 0.035 % Tween 20
FACS buffer	0.5 % albumin in PBS
HEPES Buffer	20 mM HEPES in HBSS
Macrophage culture medium	10 % FBS, 100 U/mL penicillin, 100 µg/mL streptomycin, 10% L929 cell-conditioned medium in RPMI 1640
MACS buffer	0.5 % BSA, 2 mM EDTA in PBS
Oil Red O (ORO) stock solution	0.5 % ORO in 99 % 2-propanol
Oil Red O working solution	5 % ORO stock solution in isopropanol
Posphomolybdic-phosphotungstic acid working solution	5 % equal parts posphotungstic and phosphomolybdic acid in distilled water
YAC-1 culture medium	10 % fetal bovine serum, 1 % penicillin/streptomycin, 1 % L-Glutamine, 1 % Non-Essential Amino Acids Solution (NEAA), 1 % sodium pyruvate in RPMI 1640

4.1.7 Murine antibodies for flow cytometry

Table 7: Murine antibodies used for flow cytometry

Antigen	Fluores-cence	Company	Clone	Isotype	Conc. in mg/mL	Staining dilution
CD3	FITC	BD Pharmingen	17A2	Rat IgG2b, κ	0.5	1:500
CD3e	PerCP/ Cy5.5	eBioscience	145-2C11	Armenian Hamster IgG	0.2	1:500
CD3	PB	BioLegend	17A2	Rat IgG2b, κ	0.5	1:500
CD4	APC/H7	BD Pharmingen	GK1.5	Rat IgG2b, κ	0.2	1:500
CD4	PerCP	BD Pharmingen	RM4-5	Rat IgG2a, κ	0.2	1:500

CD5	APC	BioLegend	53-7.3	Rat IgG2a, κ	0.2	1:200
CD8a	PE	BD Pharmingen	53-6.7	Rat IgG2a, κ	0.2	1:500
CD8a	PE/Cy7	eBioscience	53-6.7	Rat IgG2a, κ	0.2	1:500
CD11b	AF700	BioLegend	M1/70	Rat IgG2b, κ	0.5	1:500
CD11b	APC/Cy7	BioLegend	M1/70	Rat IgG2b, κ	0.2	1:500
CD11b	PB	BioLegend	M1/70	Rat IgG2b, κ	0.5	1:1000
CD11b	PerCP	BioLegend	M1/70	Rat IgG2b, κ	0.2	1:500
CD19	FITC	BioLegend	1D3	Rat IgG2a, κ	0.5	1:200
CD19	BUV737	BD Pharmingen	1D3	Rat IgG2a, κ	0.2	1:200
CD19	PE/Dazzle 594	BioLegend	6D5	Rat IgG2a, κ	0.2	1:200
CD23	PE	BioLegend	B3B4	Rat IgG2a, κ	0.2	1:200
CD25	PE	BD Pharmingen	PC61	Rat IgG1, λ	0.2	1:200
CD25	PerCp/ Cy5.5	eBioscience	PC61.5	Rat IgG1, λ	0.2	1:200
CD27	PE/Cy7	BioLegend	LG.3A10	Armenian Hamster IgG	0.2	1:300
CD44	BV570	BioLegend	IM7	Rat IgG2b, κ	0.1	1:10
CD45	PerCP/ Cy5.5	BioLegend	30-F11	Rat IgG2b, κ	0.2	1:500
CD45.2	APC	BD Pharmingen	104	Mouse (SJL) IgG2a, κ	0.2	1:500
CD45.2	BV510	BioLegend	104	Mouse (SJL) IgG2a, κ	Lot-specific	1:500
CD45.2	FITC	BD Pharmingen	104	Mouse (SJL) IgG2a, κ	0.5	1:500
CD45R B220	BUV395	BD Horizon	RA3-6B2	Rat IgG2a, κ	0.2	1:500
CD45R/ B220	PB	BioLegend	RA3-6B2	Rat IgG2a, κ	0.5	1:500
CD49b (DX5)	PE	BD Pharmingen	DX5	Rat IgM, κ	0.2	1:500
CD62L	FITC	BD Pharmingen	MEL-14	Rat IgG2a, κ	0.5	1:100
CD69	PerCP/ Cy5.5	BioLegend	H1.2F3	Armenian Hamster IgG	0.2	1:50
CD107a	BV421	BioLegend	1D4B	Rat IgG2a, κ	Lot-specific	1:500
CD115	APC	eBioscience	AFS98	Rat IgG2a, κ	0.2	1:500
CD127 (IL-7Rα)	BV510	BioLegend	A7R34	Rat IgG2a, κ	0.2	10 µg per 10^6 cells
CD138	PE/Dazzle	BioLegend	281-2	Rat IgG2a, κ	0.2	1:500
CD274	PerCP/ Cy5.5	BioLegend	10F.9G2	Rat IgG2b, κ	0.2	1:200

CXCR3	PE	R&D Systems	220803	Rat IgG2a, κ	-	10 µL per 10^6 cells
CCR4 (CD194)	APC	BioLegend	2G12	Armenian Hamster IgG	0.2	1:100
F4/80	PE	BioLegend	BM8	Rat IgG2a, κ	0.2	1:500
GL7	Biotin	eBioscience	GL-7	Rat IgM	0.5	1:200
IgD	BV605	BioLegend	11-26c.2a	Rat IgG2a, κ	0.2	1:200
IgM	PE/Cy7	BioLegend	RMM-1	Rat IgG2a, κ	0.2	1:200
Ly6C	PE/Cy7	BD Pharmingen	AL-21	Rat IgM, κ	0.2	1:500
Ly6G	APC/Cy7	BioLegend	1A8	Rat IgG2a, κ	0.2	1:500
NK-1.1	PerCP/ Cy5.5	BioLegend	PK136	Mouse IgG2a, κ	0.2	1:500
Nkp46	eFlour 450	eBioscience	29A1.4	Rat IgG2a, κ	0.2	1:200
PNA	FITC	Vector Laboratories	-	-	5	1:200
γδ TCR	APC	eBioscience	GL-3	Armenian Hamster IgG	0.2	1:100

4.1.8 Reagents for immunohistochemistry

4.1.8.1 Primary antibodies

Table 8: Primary antibodies used for immunohistochemistry

Antigen	Source and reactivity	Clone	Dilution	Company
MAC2	Rat	M3/38	1:400	Cedarlane, Burlington, Canada

4.1.8.2 Isotype controls

Table 9: Isotype controls

Immunoglobulin	Dilution	Company
Normal rat IgG	1:160	Santa Cruz Biotechnology, Dallas, TX, USA

4.1.8.3 Secondary antibodies

Table 10: Secondary antibodies used for immunohistochemistry

Antibody	Source	Conjugation	Dilution	Company
Anti-rat IgG	Donkey	Alexa Fluor 488	1:400	Jackson ImmunoResearch Europe Ltd., Ely, UK

4.1.9 Primers and probes for quantitative real-time PCR

4.1.9.1 Murine primers and probes from MWG

Table 11: Primers and probes used for quantitative real-time PCR ordered from MWG

Gene	Accession number	Primer sequence 5' → 3'
Abca1	NM_013454	Fwd: GGACCCGCTGTATGGAAGGAAA Rev: CCTCCCCAGCCAAGCAAGGG Probe: FAM-CCCAATCCCAGATAC-TAMRA
Ccl2	NM_009915	Fwd: GAGCATCCACGTGTTGGCT Ref: TGGTGAATGAGTAGCAGCAGGT Probe: FAM-AGCCAGATGCAGTTAACGCCCCACT-TAMRA
Hprt	NM_013556	Fwd: GACCGGTCCCGTCATGC Rev: TCATAACCTGGTTCATCATCGC Probe: VIC-ACCCGCAGTCCCAGCGTCGTG-TAMRA
Ifng	NM_008337	Fwd: TGAGTATTGCCAAGTTTGAGGTCA Rev: GTGGACCACTCGGATGAGCT Probe: FAM-CCACAGGTCCAGCGCCAAGCA-TAMRA
Il10	NM_010548	Fwd: TTTGAATTCCCTGGGTGAGAA Rev: ACAGGGGAGAAATCGATGACA Probe: FAM-CTGTGTCAATGCGGAGGGAAAG-TAMRA
Ym1	NM_009892.2	Fwd: GGAAGCCCTCCTAAGGACAAA Rev: GAATGTCTTTCTCCACAGATTCTT Probe: FAM-TGTTCTGGTGAAGGAAATGCGTAA-TAMRA

4.1.9.2 Murine primer-probe sets from Life Technologies

Table 12: Murine gene expression assays used for quantitative real-time PCR predesigned from Life Technologies

Gene	Accession number	Assay ID
Abcg1	NM_009593.2	Mm00437390_m1
Abcg5	NM_031884	Mm00446241_m1
Abcg8	NM_026180.3	Mm00445980_m1
Arg1	NM_007482	Mm00475988_m1
Ccl5	NM_013653.3	Mm01302427_m1
Cd36	NM_001159555	Mm01135198_m1
Cxcl10	NM_021274.2	Mm00445235_m1
Cyp7a1	NM_007824	Mm01135198_m1
Ddhd1	NM_001039106	Mm00616337_m1

Dhcr7	NM_007856	Mm00514571_m1
Gapdh	NM_001289726.1/ NM_008084.3	Mm99999915_g1
Gpr55	NM_001033290	Mm02621622_s1
Hmgcr	NM_008255	Mm01282499_m1
Il1b	NM_008361	Mm00434228_m1
Il6	NM_031168	Mm00446190_m1
Nos2	NM_010927	Mm00440502_m1
Ldlr	NM_001252658	Mm01177349_m1
Scarb1	NM_001205082	Mm00450234_m1
Tnf	NM_013693	Mm00443258_m1

4.2 Methods

4.2.1 Mice

4.2.1.1 Mouse strains and diet

In order to study the impact of GPR55 deficiency on atherosclerosis, *Gpr55*$^{-/-}$ mice (internal strain designation: B6; 129S5-Gpr55$^{tm1Lex/Ieg}$, C57BL/6J, EM:02355, European Mouse Mutant Archive) were crossed with *Apoe*$^{-/-}$ mice (homozygous Apoe^{tm1Unc} mutation, C57BL/6, Stock No. 002052, The Jackson Laboratory, Bar Harbor, ME, USA) to generate *Apoe*$^{-/-}$*Gpr55*$^{-/}$ double knockout mice. Age and sex-matched *Apoe*$^{-/-}$ mice served as a control group throughout all *in vivo* experiments. The animal experiments were approved by the local ethics committee (District Government of Upper Bavaria, Germany; License number: ROB-55.2-2532.Vet 02-13-111, Teilversuch 9) and performed in agreement with the institutional and national guidelines for the care and use of laboratory animals. Mice were housed in the laboratory animal facility (Zentrale Versuchstierhaltung, ZVH des Klinikums der Universität München). To induce atherosclerosis, 6 to 8-week-old mice were switched to a Western diet (21 % butterfat, 0.21 % cholesterol, TD.88137, ssniff Spezialdiäten GmbH, Soest, Germany) with access to food and water ad libitum. The mice were sacrificed after feeding a WD for either 4 or 16 weeks to assess the early and advanced stages of atherosclerosis development, respectively. Mice used for baseline characterization were fed a normal chow diet.

4.2.1.2 Genotyping

To ensure the correct genotypes of *Apoe* and *Gpr55* double knockouts (*Apoe*$^{-/-}$*Gpr55*$^{-/-}$), genotyping polymerase chain reaction (PCR) analysis was performed with tail biopsies collected from weened 21 days old mice. Tail samples of approximately 1-2 mm in length were collected in 1.5 mL microcentrifuge tubes and each mouse was given a specific identification number via ear notches.

To obtain genomic deoxyribonucleic acid (gDNA) from each tail biopsy, the ReliaPrep™ gDNA Tissue Miniprep System (Promega) was used. In brief, 100 µL of Tail Lysis Buffer and 20 µL Proteinase K were added to each tube and incubated at 56°C, 750 RPM for 1.5 h in a thermomixer. Subsequently, 300 µL Cell Lysis Buffer and 20 µL RNase A solution were added, mixed by vortexing and incubated for 10 min at 56°C. Next, 250 µL of Binding Buffer was added and the whole mixture was transferred to binding columns placed inside a collection tube. Following centrifugation at 12000 x g for 1 min, the flowthrough was discarded, and the columns were subsequently washed three times by adding 500 µL of Column Wash Solution to the column, centrifuging for 2 min at 12000 x g, and discarding the flowthrough. Elution was performed by adding 100 µL of nuclease-free water to the column after placing it in a clean microcentrifuge tube and centrifugation for 1 min at 12000 x g. The purified gDNA was stored at -20°C until further usage.

PCR was performed using GoTaq® Hot Start Master Mix, 2X (Promega) and specific primers for the wildtype and the mutated *Gpr55* allele. For the wildtype, a mixture of 5'-GCCATCCAGTACCCGATCC-3' and 5'-GTCCAAGATAAAGCGGTTCC-3' was used, generating a 441 bp amplicon. For the knockout allele, the sequences 5'-TCAAGCTACGTTTTGGGTT-3' and 5'-GCAGCGCATCGCCTTCTATC-3' were used to create a 301 bp amplicon.

The PCR mix was prepared according to the following table:

Table 13: PCR mix

Substance	Volume
Master Mix, 2X	7.5 µL
Fwd primer	0.75 µL
Rev primer	0.75 µL
Nuclease free water	3 µL

Twelve µL of the PCR mix and 5 µL of the isolated gDNA were pipetted into 8-well PCR tube strips and closed with the supplied lid. The PCR was then performed on a Primus 25 advanced® Thermocycler (Peqlab) according to the following protocol:

Table 14: PCR program

Temperature	Time	
95°C	3 min	
95°C	20 s	}35 cycles
59°C	20 s	
72°C	30 s	
72°C	7 min	
4°C	∞	

For agarose gel electrophoresis, a 2 % gel was prepared by mixing 80 mL of 1:50 diluted TAE buffer (Table 6) with 1.6 g agarose and carefully heating in the microwave for approximately 30 s at 1200 watts until the mixture appeared transparent. The bottle was cooled by rinsing the outside with cold tap water for 20-30 s and then 43 µL of ethidium bromide was added. The agarose gel was immediately filled onto a plate and a comb was placed on the left side. After the gel had polymerized, the comb was removed, and it was covered entirely with TAE buffer. Each pocket was loaded with 19 µL of amplified DNA and 13 µL of 1 kb DNA ladder standard were added to the first pocket. The currency was set to 90 V and run for 15 min. The gel was photographed under an ultraviolet light transilluminator to visualize the desired DNA fragments.

4.2.1.3 Mouse dissection

Mice were euthanized by intraperitoneal injection with a mixture of ketamine (80 mg/kg) and xylazine (12 mg/kg) adjusted to the individual body weight. Blood was extracted via cardiac puncture using a syringe flushed with 0.5 mM EDTA and immediately transferred into an EDTA microtube to avoid blood clotting. The mouse heart and vasculature were subsequently perfused with 10 mL of PBS to remove blood and non-adherent leukocytes. Then, the spleen, liver, heart, femurs, aorta and lymph nodes were harvested. To determine leukocyte subsets, platelet and red blood cell counts, 20 µL of full blood were analyzed with a hematology analyzer. Plasma was obtained by centrifugation of full blood for 10 min at 2500 x g and kept at -80°C until further use. Tissues were snap-frozen in liquid nitrogen and stored at -80°C until they were used for RNA extraction. Hearts were embedded in Tissue-tek, frozen using a methylbutane bath in liquid nitrogen and afterward stored at -20°C until sectioning and histological analysis were performed. Some of the tissues such as the spleen, lymph nodes, and aortas were kept in PBS on ice and evaluated by flow cytometry within the same day.

4.2.2 Flow cytometry

4.2.2.1 Tissue preparation for flow cytometry

Spleen:

Spleens were harvested, cut in half, weighed, and transferred into ice-cold PBS until further processing. All the following steps were carried out on ice. A single-cell suspension was prepared by mashing the spleen through a 70 µm cell strainer into a 50 mL tube using the plunger of a 2 mL syringe and rinsing with fluorescence-activated cell sorting (FACS) buffer (Table 6) to a total volume of 15 mL. The cell suspension was then centrifuged at 400 x g at 4°C for 5 min, the supernatant discarded, and the pellet was resuspended in 1 mL ACK buffer (Table 6) for red blood cell lysis. Immediately after, the cells were pelleted, the supernatant was discarded, and the cells were washed with 5 mL FACS buffer and filtered through a 50 µm filter into a 15 mL tube. The splenocytes were centrifuged again and resuspended in 3 mL FACS buffer, of which 200 µL were used for staining.

Blood:

A 50 µL aliquot of freshly collected whole blood was directly transferred into ice-cold FACS tubes. The blood was incubated with 1 mL ACK buffer for 15 min, centrifuged at 400 x g at 4° C for 5 min and washed with 1 mL of FACS buffer. After centrifugation and discarding the supernatant, the resulting cell pellet was used for staining.

Bone marrow:

The femurs were cleaned to remove all excess tissue. The condyles, patella, and epiphysis were removed to expose the metaphysis. With the metaphysis facing down, the prepared bones were placed into a 1 mL pipet tip that was cut to fit into a 1.5 mL microcentrifuge tube. After centrifuging at 10000 x g for 2 min, a bone marrow pellet was visible, while the femur appeared white. For the flow cytometry analysis, the pellet was resuspended in 1 mL ACK buffer and centrifuged immediately for 5 min at 500 x g. The supernatant was discarded, washed with PBS and after another 5 min centrifugation at 500 x g, resuspended in 500 µL FACS buffer. Then, 50 µL of the prepared cell suspension was used for staining.

Lymph nodes:

Two to three lumbar paraaortic lymph nodes were harvested and immediately placed into ice-cold PBS. For exact weight measurement, excess water was drained on a paper towel and all collected lymph nodes per animal were weighed. A single-cell suspension was prepared by mashing the lymph nodes through a 70 µm cell strainer into a 50 mL tube using the plunger of a 2 mL syringe and rinsing with FACS buffer to a total volume of 10 mL. The cell suspension was then centrifuged at 4°C for 5 min, the supernatant discarded, and the pellet resuspended in 1 mL FACS buffer before transferring into a flow cytometry tube through a cell strainer cap. After centrifuging and discarding the entire supernatant, the resulting pellet was ready for staining.

Aorta:

The enzymatic aorta digestion cocktail (Table 6) was prepared in PBS in a total volume of 500 µL per aorta. Aortas were incubated with the mixture for 1 h at 37°C and 400 RPM in a thermomixer. After 30 min, the aorta was further mechanically disrupted by pipetting up and down vigorously with a 1 mL pipette. Then, the incubation was continued for another 30 min. Subsequently, the lysate was filtered through a 35 µm snap cap cell strainer into a FACS tube, centrifuged and washed and the resulting cell pellet was used for staining.

4.2.2.2 General flow cytometry staining procedure

The staining procedure for cell surface antibodies was performed in a standardized manner for all cell types. After centrifuging and discarding the entire supernatant, 50 µL Fc block CD16/CD32 (dilution 1:1000) was added to the obtained cell pellet, gently vortexed and incubated for 5 min at room temperature. Subsequently, 50 µL of FACS staining antibody mix was added to each sample, vortexed and incubated for 30 min at 4°C in the dark. This step was followed by washing the cells by adding 1 mL of FACS buffer and centrifuging at 400 x g for 5 min. The resulting cell pellet was resuspended in 300-500 µL of FACS buffer, depending on the number of cells, and then kept in the dark at 4°C until analysis was performed.

4.2.2.3 General flow cytometry measurement procedure

A BD FACS Canto II Cell Analyzer was used to acquire cells that were stained with up to 8 different fluorochrome-conjugated antibodies. Stainings with more than 8 fluorochromes were measured with a BD LSRFortessa Flow Cytometer. Data were recorded with BD FACSDiva software and subsequently evaluated using FlowJo v10.2 software. Stained single-cell suspensions were always resuspended in a defined amount of buffer prior to measurement. The samples were measured at low, medium, or high flow rates for a predefined period of time. The exact volume recorded during one measurement was determined using a standard curve that was generated in advance, using a solution of CountBright absolute counting beads. The solution with a known concentration of counting beads was acquired at each flow rate for several periods to create the standard curve. This method enabled the calculation of total cell counts per µL of blood or mg of tissue, respectively, based on a known acquisition volume and sample size when generating the single-cell suspension.

4.2.2.4 Fluorescence-Activated Cell Sorting

Leukocyte subsets were isolated from full blood using FACS. Blood samples of female *Apoe*$^{-/-}$ mice were prepared and stained with fluorescence-labeled antibodies as described above for flow cytometry analysis. A BD FACS Aria III Cell Sorter was used to isolate 25000 cells of each cell population (Table 15). The cells were collected in 2 mL Rnase-free microcentrifuge tubes, snap-frozen in liquid nitrogen and stored at -20°C. The sorted cell subsets were then processed for RNA extraction and qPCR analysis.

Table 15: Leukocyte sorting scheme

Cell population	Surface markers
CD11b$^+$ cells	CD45$^+$CD11b$^+$
Monocytes	CD45$^+$CD11b$^+$CD115$^+$Ly6G$^-$
Neutrophils	CD45$^+$CD11b$^+$CD115$^-$Ly6G$^+$
NK cells	CD3$^-$CD49b(DX5)$^+$
B cells	CD3$^-$B220$^+$
CD3$^+$ T cells	CD3$^+$B220$^-$

4.2.3 Histology

4.2.3.1 Aorta en face preparation

After removing the perivascular fat, the aortas were harvested from the aortic arch to the iliac bifurcation, pinned onto rubber slides and incubated in a 10 % formalin solution overnight. Subsequently, the aortas were cut open longitudinally and pinned again onto the rubber slides with the intima facing downwards. The adventitia was carefully removed using microdissection instruments under a stereomicroscope.

4.2.3.2 Oil Red O staining of whole aortas

Cleaned aortas without adventitia were dipped ten times in 60 % isopropanol, incubated in Oil Red O (ORO) working solution (Table 6) for 15 min and dipped ten times again in 60 % isopropanol. Next, the vessels were rinsed in distilled water, placed flat onto a glass slide with the intima facing up and mounted with Kaiser's glycerin jelly. The mounting medium was prepared by mixing 4 g of gelatin with 21 mL of distilled water, to which 25 mL of glycerin were added and mixed for 15 min until dissolved. Images of the entire aorta were taken with a Leica DMRBE microscope at a 2.5x magnification and stitched together using AutoStich software. The plaque burden was quantified as the ratio of the ORO-stained plaque area relative to the total surface area of the aorta using LAS V4.3 software.

4.2.3.3 Oil Red O staining of aortic roots

Aortic root cross-sections were cut with a cryotome at a thickness of 5 µm. The sections were fixed in 4 % formalin for 10 min at room temperature, washed in PBS for 5 min and then dipped ten times in 60 % isopropanol. After incubating in ORO working solution for 15 min, dipping 10 times in 60 % isopropanol was repeated. Sections were rinsed in running tap water for 5 min and counterstained with Mayer's Hematoxylin solution for 3 min, followed by another 5 min tap water rinse and mounting with Immu-Mount. Using Las V4.3 software, images of 5-6 sections per heart, taken with a Leica DMRBE microscope at 5x magnification, were analyzed by calculating the whole plaque area per section, normalized to the length of the aortic internal elastic lamina (IEL).

4.2.3.4 Masson Trichrome staining

Cryosections of aortic roots were rehydrated in PBS for 5 min at room temperature. Bouin's solution was heated to approximately 60°C, and the slides were incubated in the solution for 20 min and then rinsed first in running tap water and subsequently in distilled water. The sections were stained in Weigert's iron hematoxylin for 12 min, followed by a running tap water rinse for 10 min and a brief 1 min rinse with distilled water. Afterward, the slides were stained in Biebrich scarlet-acid fuchsin for 1 min, then quickly dipped once in distilled water and immediately transferred to the phosphomolybdic-phosphotungstic acid working solution (Table 6) for 30 min. From there, the sections were directly transferred to Aniline Blue for 10 min, then dipped once in distilled water, once in 1 % acetic acid and placed in Xylene until mounted with Entellan. Images of individual lesions were taken with a Leica DMRBE microscope at 10x magnification. A threshold analysis for the blue-stained area was applied using LAS 4.3 software to calculate the ratio of collagen (blue) area to the total plaque area

4.2.4 Immunohistofluorescence

4.2.3.5 Macrophage staining

Macrophage content within each plaque of aortic roots was quantified by staining with Mac2 antibody. Five µm cryosections were fixed with 4 % formalin for storage until used for staining. These slides were immersed in PBS for 5 min before antigen retrieval was performed. Therefore, citrate buffer (Table 6) was heated in a microwave until boiling and the sections were added and incubated for 10 min at which time the microwave was adjusted to 90 watts. Slides were incubated for another 30 min in the buffer at room temperature. Sections were then washed in PBS for 5 min before encircling every section with a Pap-Pen. Then, 30 µL of blocking solution (Table 6) was added to each section and slides were incubated for 30 min at 4°C in a humid and dark incubation chamber. After discarding the blocking solution, the sections were stained overnight at 4 °C with the primary antibody Mac2 in a 1:400 dilution in blocking solution in the incubation chamber. For isotype control, a rat IgG antibody in the concentration of 1:200 was used. After incubation with the primary antibody, slides were washed in PBS three times for 5 min each, and a secondary anti-rat antibody was added and incubated for 1 h at room temperature. To counterstain the nuclei, Hoechst 33342 was prepared at a concentration of 1:1500 in PBS + Tween 20 at 0.1 % and a few drops were added to each section and incubated for 2 min. Subsequently, washing three times in PBS was repeated and the slides were mounted with Immu-Mount and kept in the dark at 4°C until microscopy analysis. Pictures of individual plaques were taken with a Leica DM6000 fluorescence microscope at 10x magnification. Similar to the Masson Trichrome analysis described above, a threshold analysis for the Mac2-positive area was applied and the result normalized to the total plaque area.

4.2.4 Cell culture and functional assays

All cells for *in vitro* studies were cultivated in media designed specifically to meet the requirements of each experiment and maintained in a CO_2 incubator, ensuring an optimal atmosphere at 37°C and humidified 5 % CO_2. Experiments were performed in a laminar flow hood under sterile conditions. For long-term storage, a defined number of cells were resuspended in a culture medium supplemented with 7.5 % DMSO, frozen in liquid nitrogen, and stored at -150°C.

4.2.4.1 Magnetic bead-based cell separation

To isolate specific target cells from spleens, a magnetic cell separation method (MACS, Miltenyi Biotec) based on negative isolation was used. In this method, a cocktail of primary antibodies binds to all unwanted cells, which are then labeled by a biotin-conjugated secondary antibody attached to a magnetic microbead. The labeled cells are depleted by binding to the column. The target cells stay untouched and

usable for further cell culture and flow cytometry experiments. This method was used to isolate NK cells that were used in cell culture experiments. All steps were carried out on ice with pre-cooled solutions and centrifuges used at 4°C. First, a MACS buffer solution was prepared (Table 6). A single-cell suspension from the whole spleen of a mouse was prepared as described above and the cell number was determined using an automated cell counter. The following liquid measurements were all calculated per 10^7 cells and the volumes needed to be adjusted to the total amount of sorted cells. After centrifuging at 300 x g for 10 min, the cell pellet was resuspended in 40 µL of MACS buffer and 10 µL of NK Cell Biotin-Antibody cocktail was added, followed by 5 min incubation in the dark. The cells were washed by adding 2 mL buffer solution and centrifuging at 300 x g for 10 min. The resulting pellet was resuspended in 80 µL of buffer and 20 µL of Anti-Biotin MicroBeads, again incubated in the dark for an additional 10 min. Magnetic separation was accomplished by placing LS-columns in the magnetic field of a MACS Separator and adding the cell suspension onto the column which was rinsed before and after adding the cells with 3 mL buffer. Bead-labeled non-target cells remained in the column and the flowthrough represented the enriched unlabeled cells of interest. The overall NK cell purity was determined by flow cytometry, staining a sample with CD49b (DX5), CD3, and CD45 antibodies. After excluding debris and dead cells, the ratio of $CD3^-$ CD49b $(DX5)^+$ to total $CD45^+$ cells was calculated.

4.2.4.2 Uptake of DiI-conjugated oxLDL by bone marrow-derived macrophages

Femurs were harvested and prepared as previously described for flow cytometry analysis. The single-cell suspension was diluted in macrophage culture medium (Table 6) supplemented with L929 cell supernatant, which is high in M-CSF to induce monocyte differentiation into macrophages. The supernatant was prepared according to a protocol provided by Tomida et al. and the medium was exchanged every three days[182].

Cells were cultured with 50 µg/mL fluorescence-labeled oxLDL for 24 h and then mechanically detached using a cell scraper, washed and stained with CD45, CD11b and F4/80 fluorescent antibodies. Cells were analyzed using a BD FACS Canto II and the uptake of oxLDL per macrophage was quantified as mean fluorescence intensity (MFI) of the $CD45^+$, $CD11b^+$ and $F4/80^+$ cell population.

4.2.4.3 NK cell cytotoxicity assay

To quantify the cytotoxic activity of NK cells *in vitro*, a colorimetric method based on the detection of lactate dehydrogenase (LDH) release was used. NK cells were isolated from spleens as described above, using a magnetic bead-based negative cell sorting method and, once isolated, were immediately used for this assay. YAC-1 cells, a T cell lymphoma cell line lacking the expression of MHC I molecules and

therefore being susceptible to the cytotoxic activity of NK cells, kindly provided by Prof. Dr. med. Sebastian Kobold, Division of Clinical Pharmacology, Department of Medicine IV, Klinikum der Ludwig-Maximimilians-Universität München, were used as target cells.

The assay was performed in a 96-well plate that was prepared according to the following table:

Table 16: Experimental design for the cytotoxicity assay

	Number of wells	**YAC-1**	**NK**	**Additives**
Low control	6	20000	-	-
High control	3	20000	-	100 µL Triton X-100 2 % in assay medium
Background control	6	-	-	Assay medium
	3 per specimen	20000	100000	
	3 per specimen	20000	50000	
	3 per specimen	20000	25000	

The 96-well plate was then incubated at 37°C in a CO_2 incubator for 5 h, 2 % Triton X-100 in assay medium was added to the wells acting as a high control with maximum LDH release after 4 h and 15 min. Spontaneous LDH release of YAC-1 cells was determined as well, acting as a low control. After incubation, the plates were centrifuged at 400 x g for 5 min and 100 µL supernatant of each well was transferred to a new 96-well plate. To quantify LDH release, 100 µL of reaction mix (Cytotoxicity Detection Kit, Roche), freshly prepared according to the manufacturer's instructions, were added to each well and incubated for 30 min at room temperature in the dark. Measurement of the 96-well plate was carried out in a Safire II microplate reader (Tecan) at 490 nm.

The percentage cytotoxicity was determined using the following equation after calculating the average absorbance values of the triplicates:

$$\text{Cytotoxicity (\%)} = \frac{\text{exp. value} - \text{low control}}{\text{high control} - \text{low control}} \times 100$$

4.2.4.4 NK cell stimulation assay

Cytokine treatment enhances the activity of NK cells[183]. The activity of IL-2 stimulated WT NK cells was compared to *Gpr55* knockout NK cells. After sterilizing flat-bottom 96-well half-area plates under UV light for 10 min, they were coated with NKp46 at a concentration of 0.5 µg per 100 µL overnight. A single-cell suspension from the spleens of WT and *Gpr55*$^{-/-}$ mice was prepared as described above, cells were counted, and 250000 splenocytes per well were seeded. The medium was

supplemented with IL-2 (conc. 100 U/well) and the monoclonal antibody CD107a (conc. 1:100), and cells were incubated for 5 h in a CO_2 incubator at 37°C. After collecting and washing the cells, they were stained with CD3 and CD49b (DX5) antibodies and measured in a FACS Canto II. To compare NK cell activity between the WT and the knockout group, the relative number of $CD107a^+$ NK cells was determined by flow cytometry.

4.2.5 Biomolecular methods

4.2.5.1 RNA isolation

Total ribonucleic acid (RNA) was extracted either from murine tissues previously harvested and stored at -80°C as described above or from isolated cells. Tissue lysis was performed mechanically by adding one steel bead (Quiagen Tissue Lyser steel bead) and 500 µL TRIzol™ Reagent to a 2 mL tube containing the frozen tissue. Homogenization was performed at 5 Hz for 2 min using a TissueLyzer (Quiagen). The resulting cell suspension was transferred to a new 1.5 mL tube and 125 µL of chloroform was added, followed by vortexing at maximum frequency for 30 s and centrifugation at 12000 x g for 10 min at 4°C. This resulted in the separation of the samples into three distinct phases. The bottom layer is the organic phase, red in color and containing proteins, followed by a small grey interphase containing DNA and on top an aqueous phase containing the RNA. All the next steps were performed using the peqGOLD Total RNA Kit (Peqlab Biotechnologie) according to the manufacturer's protocol. The top layer was gently transferred onto a DNA Removing Column placed into a supplied 2.0 mL Collection Tube without touching any of the other layers thus avoiding contamination. The column was centrifuged at 12000 x g for 1 min and the obtained flow-through was mixed with an equal amount of 70 % ethanol by vortexing briefly. The lysate was then added to a PerfectBind RNA Column which was placed into a new 2.0 mL Collection Tube. The column and tube assembly was centrifuged at 10000 x g for 1 min and the flow-through was discarded. The column now containing the RNA on its membrane was washed three times, first with 500 µL of RNA Wash Buffer I, then twice with 600 µL of RNA Wash Buffer II. During each washing step, the column and tube assembly was centrifuged at 10000 x g for 15 s and any flow-through was discarded. To remove any remaining ethanol, drying of the column was accomplished by centrifuging at 10000 x g for 2 min. Lastly, the PerfectBind RNA Column was placed into a fresh 1.5 mL tube, and 50 µL of nuclease-free water was added to the membrane and centrifuged for 1 min at 5000 x g to elute the RNA. The yield and purity of each RNA sample were determined spectrophotometrically at OD260/OD280 with a Nanodrop (Peqlab) and ratios lower than 1.7 were excluded from all experiments. Samples were stored at -20°C until further use.

4.2.5.2 Reverse transcription

Reverse transcription (RT) of RNA into complementary DNA (cDNA) was performed using the PrimeScript RT reagent kit (Takara) according to the manufacturer's instructions. All pipetting steps were carried out on ice. An RT reaction mix for each sample of 1 µg RNA was prepared according to the following table.

Table 17: RT reaction mix

Reagent	Amount
RNA (100 ng/µL)	0.2 µg
5x PrimeScript Buffer	2 µL
PrimeScript RT Enzyme mix I	0.5 µL
Oligo dt Primers (50 µM)	0.5 µL
Random hexamers (100 µM)	2 µL
Nuclease-free water	ad 10 µL

Reverse transcription was performed in a thermocycler using the following program:

Table 18: RT program

Temperature	Time
37°C	15 min
85°C	5 s
4°C	∞

The resulting cDNA was diluted with nuclease-free water to a concentration of 2 ng/µL.

4.2.5.3 Real-time polymerase chain reaction

Quantitative real-time PCR (qPCR) was performed using the KAPA PROBE FAST Universal qPCR kit and TaqMan® technology. Primers were either obtained pre-designed as a primer-probe mix from Life Technologies or primers and probes purchased individually from MWG (Tables 10 and 11). A 4x primer-probe mix was prepared according to the following table.

Table 19: qPCR primer-probe mix

MWG 4x primer-probe mix		Life Technologies 4x primer-probe mix	
Primer fwd (100µM)	4 µL	Primer-probe-Mix	0.5 µL
Primer rev (100 µM)	4 µL	Nuclease-free water	4.5 µL
Probe (100 µM)	1 µL		
Nuclease-free water	241 µL		

For a single qPCR reaction, the 4x primer-probe mix was combined with a Master mix (Promega), Reference dye high and cDNA to create the qPCR reaction master mix which was kept on ice in the dark (Table 20).

Table 20: qPCR reaction mix

Reagent	Amount
Master mix 2x	10 µL
4x primer-probe mix	5 µL
Reference dye high	0.4 µL
cDNA	5 µL

For each sample, duplicates of 15.4 µL qPCR reaction master mix combined with 5 µL of cDNA (2 ng/µL) were pipetted into a semi-skirted 96 well plate. Nuclease-free water served as a negative control. Hypoxanthineguaninphosphoribosyltransferase (*Hprt*) was considered as most stably expressed in the examined tissues and therefore used as a reference gene throughout all experiments. The qPCR was performed on a 7900HT Sequence Detection System according to the following program:

Table 21: qPCR program

Temperature	Time	
95°C	20 s	
95°C	1 s	}40 cycles
60°C	20 s	

Data obtained by real-time qPCR was analyzed using SDS2.4 software. The relative expression of the gene of interest to *Hprt* was calculated using the $2^{-\Delta\Delta CT}$ method[184]. For comparing *Gpr55* expression in sorted leukocytes, glyceraldehyde-3-phosphate dehydrogenase (*Gapdh*) was used as a complementary housekeeping gene.

4.2.5.4 Multiplex immunoassay

To determine the total amount of immunoglobulin isotypes in murine plasma samples, an immunoassay based on the Luminex xMAP technology (eBioscience)

was used. This method allowed for the simultaneous measurement of IgG1, IgG2a, IgG2b, IgG3, IgA, IgE, and IgM. In this assay, antibodies against the target proteins are conjugated to magnetic microsphere beads, which are additionally conjugated with different fluorophores for each antibody. This enables the simultaneous analysis of multiple proteins within one sample. Plasma samples were centrifuged at 10000 x g for 10 min at 4°C and transferred to new tubes prior to the analysis to reduce the plasma cholesterol content as a confounding factor for the multiplex measurement. Antigen standards were prepared as required by the manufacturer's instructions. A 3-fold serial dilution was used to prepare a standard curve. The Universal Assay Buffer without any additive served as a negative control. Using a multichannel pipette, 25 µL of Antibody Magnetic Beads were added to each well of the 96-well flat bottom plate included in the kit, which was placed on top of the magnetic plate holder. After 2 min, the beads had accumulated on the bottom of each well and the plate was inverted quickly to remove excess liquid. To wash the plate, 150 µL of 1X Wash Buffer was added to each well and after another 2 min, the plate was inverted again, making sure that it was always securely in contact with the magnetic plate holder. Now, 25 µL of previously diluted plasma or standards combined with 25 µL of Universal Assay Buffer were added to each well. The whole plate was sealed with adhesive, covered, and incubated at 500 rpm for 60 min at room temperature using a Thermomixer. Then, the plate was washed three times as described above before adding 12.5 µL of 1X Detection Antibody Mixture to each well. The plate was again covered and incubated at 500 rpm for 60 min at room temperature. After that, washing was repeated and 120 µL Reading Buffer was added to each well. The samples were then ready to measure with the Luminex MAGPIX instrument. Data analysis was performed by using ProcartaPlex Analyst software.

4.2.5.5 Cholesterol measurement in plasma

The plasma of mice was obtained after centrifuging full blood in EDTA-coated vials and diluted with 0.9 % NaCl to 1:9 after a WD and 1:3 after a chow diet, respectively. The calibrator reagent supplied by the kit was dissolved in 3 mL distilled water (cholesterol concentration 160 mg/dl). For generating a standard curve, calibrator fluid was used in a 2x, 1x, 1:2, 1:4, 1:8 and 1:16 concentration diluted with 0.9% NaCl. Five µL each per plasma sample or diluted calibrator solution were pipetted in duplicates into a 96-well flat-bottom microtiter plate. Then, 200 µL CHOL reagent was added to each well using a multichannel pipette. After incubation for 30 min at room temperature, the absorbance (505 nm) was measured in a 96-well plate reader (Tecan Infinite F200 Pro). Cholesterol levels of each sample were calculated based on a linear function derived from measuring the optical density of the calibrator solution.

$$Sample\ value\ (\frac{mg}{dL}) = (Optical\ density\ (sample) \times m + y) \times dilution\ factor$$

4.2.6 Plasma LPI measurement

The concentration of 20:4 LPI was measured in plasma samples obtained from full blood and stored at -80°C as described above. The analysis was performed by liquid chromatography-multiple reaction monitoring as described[185], carried out by Dr. Laura Bindila, at the Institute for Physiological Chemistry University Medical Center, Mainz, Germany.

4.2.7 Statistical analysis

Statistical analysis was performed using GraphPad Prism 8 software and data are presented as average ± standard error of the mean (SEM). Significant results were determined by Student's unpaired t test for normally distributed data. When comparing three or more data sets, one-way analysis of variance (ANOVA) followed by the Bonferroni post hoc test was used. P values < 0.05 were considered statistically significant.

5 RESULTS

5.1 Tissue and leukocyte-specific *Gpr55* expression

The impact of diet-induced hypercholesterolemia on the expression of *Gpr55* was determined by performing qPCR analysis in different tissues of *Apoe*$^{-/-}$ mice. Spleen and bone marrow were chosen because of their function as production sites and reservoirs of leukocytes. Second, the aorta was selected as a major site of murine atherosclerotic lesions development. The expression of *Gpr55* was calculated relative to the expression of *Hprt*, the reference gene used for all our qPCR studies. The *Apoe*$^{-/-}$ mice used for this analysis either received a normal chow diet (baseline) and were harvested at the age of 8 to 10 weeks before atherosclerotic lesions were established or were treated with a WD for 4 or 16 weeks, respectively. The *Gpr55* mRNA expression in the spleen increased significantly after 4 weeks of WD and declined to baseline levels after 16 weeks of WD. *Gpr55* expression in bone marrow cells decreased over the duration of WD treatment and was lower in the stage of late atherosclerosis compared to the initial values. Aortic *Gpr55* expression was only measured in tissue from hypercholesterolemic mice with plaques and diminished after the 16-week treatment period compared to 4 weeks (Figure 10).

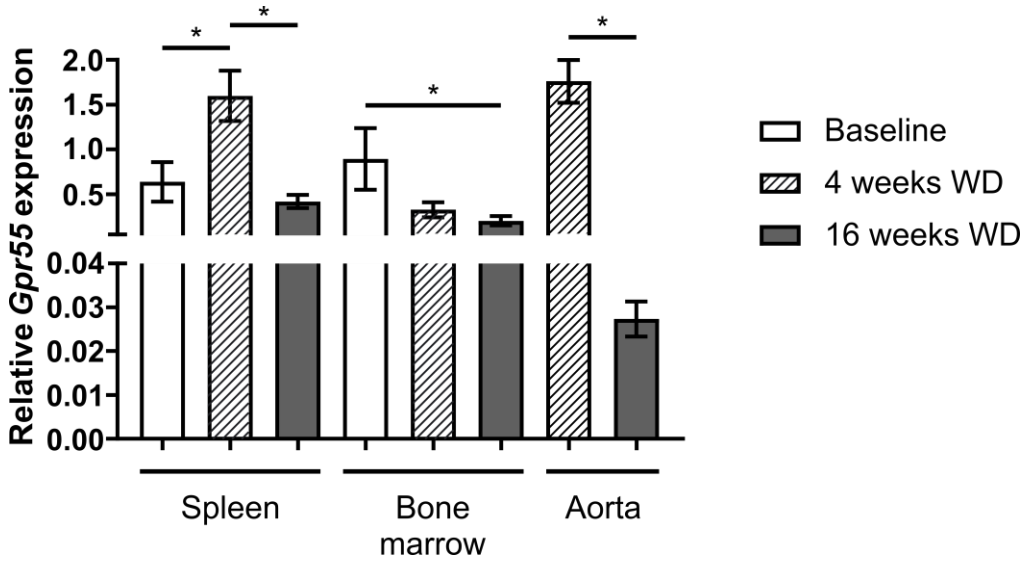

Figure 10: *Gpr55* mRNA expression in spleen, bone marrow, liver and aorta.
Tissue samples from organs that play a role in the chronic inflammatory processes involved in atherogenesis were harvested from male *Apoe*$^{-/-}$ mice. The expression of *Gpr55* mRNA was assessed without WD (baseline), after 4 and 16 weeks of WD normalized to the expression of *Hprt*. Data show mean ± SEM, n = 8-12. One-way ANOVA followed by Bonferroni multiple comparison test was used if 3 data sets were compared, Student's t-test to determine significant changes between two groups. *P<0.05.

As previously reported, *Gpr55* is highly expressed on leukocytes like neutrophils[134], monocytes, NK cells[135], and in particular, B cells[136]. The expression of *Gpr55* mRNA in FACS-sorted blood leukocyte subsets was confirmed by qPCR analysis, with the highest mRNA expression determined in B cells (Figure 11).

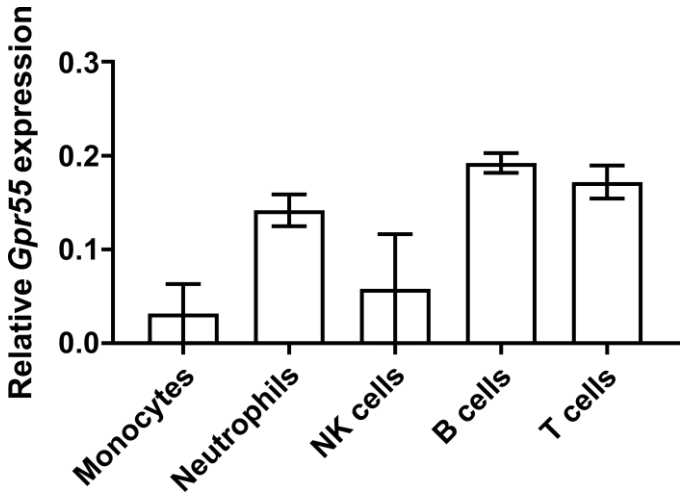

Figure 11: *Gpr55* mRNA expression in leukocyte cell subsets.
Gpr55 mRNA expression in FACS-sorted leukocyte subsets was determined in female *Apoe*$^{-/-}$ mice (n = 4) relative to the expression of *Hprt* and *Gapdh*.

5.2 The LPI/GPR55 axis is activated during early atherosclerosis

LPI is the endogenous ligand of GPR55, and DDHD1 is the main enzyme that catalyzes the generation of 2-arachidonoyl LPI. Hypercholesterolemia resulted in a higher relative mRNA expression of *Gpr55* in the spleen and aorta in the early stages of atherogenesis (Figure 10) in *Apoe*$^{-/-}$ mice. To assess whether the whole LPI/GPR55 axis is affected by hypercholesterolemia and atherogenesis, plasma samples were collected when the mice were sacrificed to measure the amount of circulating LPI by mass spectrometry. Additionally, the mRNA expression of *Ddhd1* was determined in the spleen. During the early stage of the disease, an increase in splenic and aortic *Gpr55* expression was associated with simultaneously elevated LPI plasma levels (Figure 12A) and an increased splenic *Ddhd1* mRNA expression (Figure 12B). Both plasma LPI concentration and *Ddhd1* mRNA expression declined below baseline levels, similar to the mRNA expression of *Gpr55* in various tissues (Figure 10).

These results show an activation of the LPI/GPR55 axis during early lesion formation, which declined during disease progression.

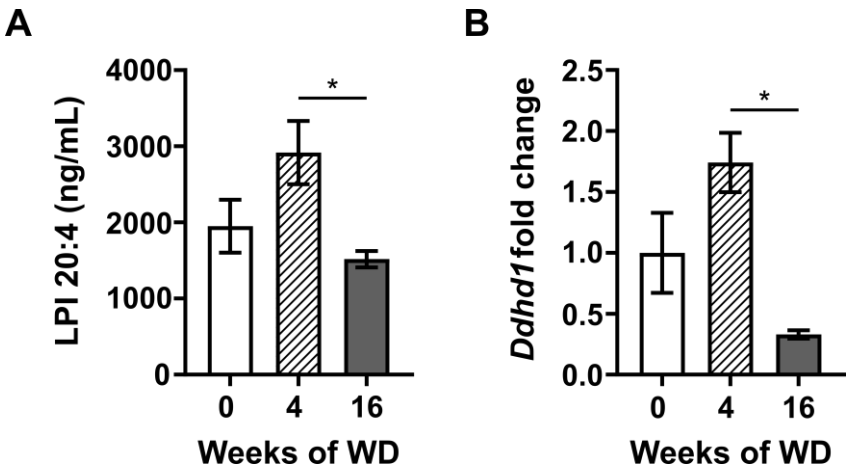

Figure 12: LPI generation peaks at the early stages of atherosclerotic lesion development.
(**A**) The concentration of 1-arachidonoyl LPI was measured in plasma samples of *Apoe*$^{-/-}$ mice at baseline conditions (0 weeks WD) and after 4 and 16 weeks of WD (n = 7-8). (**B**) *Ddhd1* mRNA expression in the spleen was analyzed as a fold change of 4 weeks WD and 16 weeks WD versus baseline (n = 7-12). All data were measured in female animals. One-way ANOVA followed by Bonferroni multiple comparison test was used to compare data sets. *P<0.05.

5.3 *Gpr55* knockout worsens metabolic parameters

Previous studies revealed an increase in body weight of *Gpr55*$^{-/-}$ mice compared to a WT control group[156,164]. To investigate metabolic effects due to GPR55 deficiency during WD treatment, parameters such as body weight and blood cholesterol were determined. Mice were weighed at the age of 6 to 8 weeks before receiving WD, and when sacrificed 4 or 16 weeks later. Total cholesterol was measured in plasma. Before starting the treatment, no differences in body weight were observed. However, the body weight in *Apoe*$^{-/-}$*Gpr55*$^{-/-}$ mice increased significantly more than in *Apoe*$^{-/-}$ control animals during the experiment period (Figures 13A and B).

Total cholesterol levels in plasma increased as a result of the WD in all treated mice. *Gpr55* knockout only influenced male cohorts to exhibit a more substantial increase in circulating cholesterol compared to the control groups (Figure 13C).

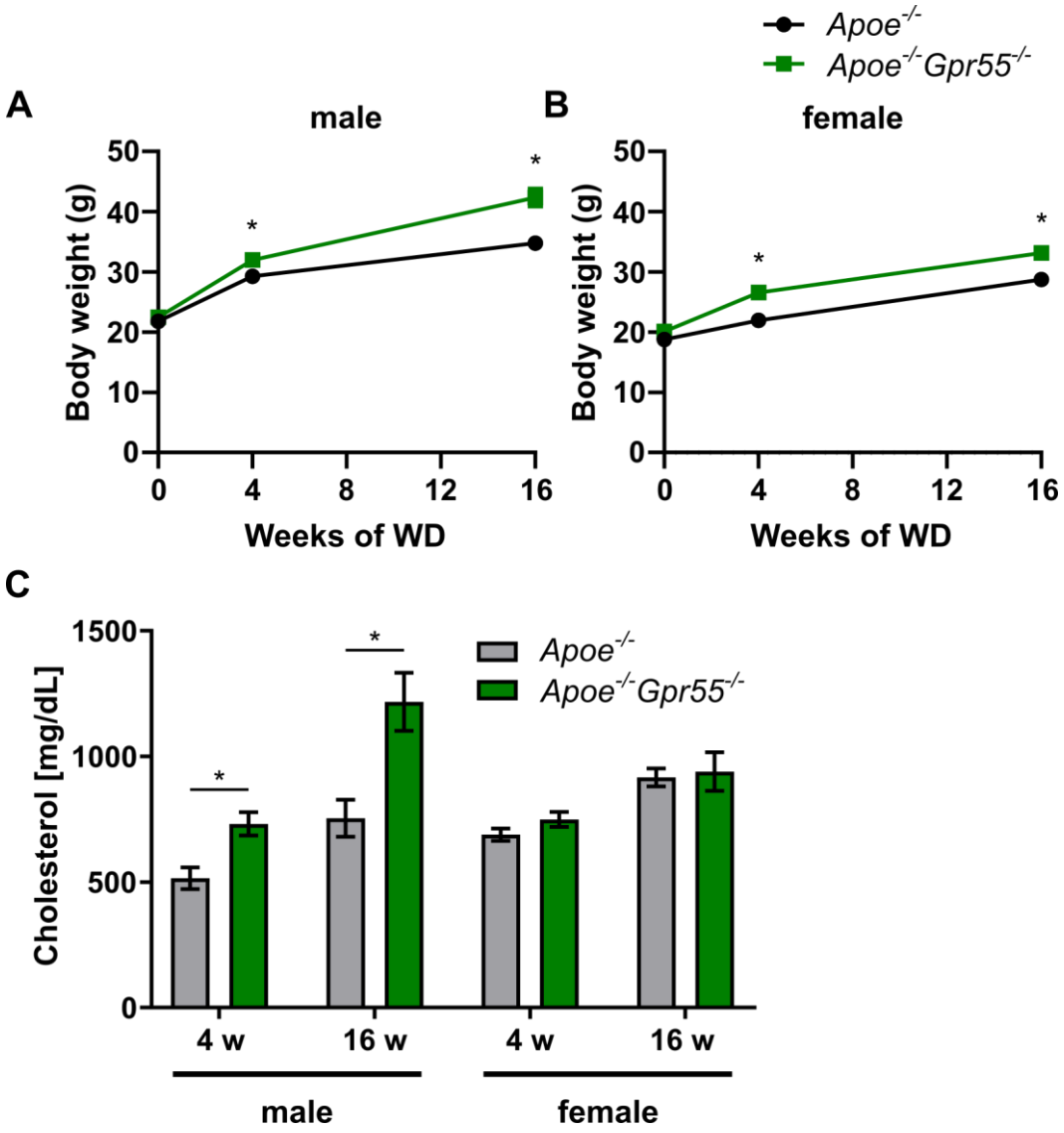

Figure 13: *Gpr55* knockout increases body weight and plasma cholesterol levels during WD. *Apoe*$^{-/-}$ and *Apoe*$^{-/-}$*Gpr55*$^{-/-}$ mice of both sexes were fed a WD. (**A**) Body weight was measured in male mice before treatment (n = 26 per group) and at the end of the experiment after either 4 weeks (4 w, n = 12-17) or 16 weeks (16 w, n = 15-22) of WD. (**B**) Body weight of female mice was measured accordingly. Before WD treatment (n = 30 per group), after 4 w (n = 17-22) and after 16 w (n = 14-18) of WD. (**C**) Total cholesterol levels of the animals treated for 4 and 16 weeks were measured in plasma. Data show mean ± SEM, Student's t-test: *P<0.05.

5.4 Lipid metabolism is more active in *Apoe*$^{-/-}$*Gpr55*$^{-/-}$ mice

Atherosclerosis is characterized by the accumulation of lipoproteins in the endothelium. Impaired lipid metabolism is among the main risk factors in the development of atherosclerosis. One of the most established therapies to reduce cardiovascular risk is to lower the amount of circulating LDL. The most common lipid-lowering drugs for primary and secondary prevention of CVDs are statins. They inhibit the key enzyme of the cholesterol biosynthetic pathway HMG-CoA reductase (HMGCR).

Male *Gpr55*$^{-/-}$ mice showed significantly higher plasma cholesterol levels compared to the control groups (Figure 13C). To further elucidate the influence of GPR55 on cholesterol and lipoprotein metabolism, the expression of several enzymes and transporters involved in lipid metabolism was analyzed in liver tissue. The mRNA expression of reverse cholesterol transporters (*Abca1, Abcg1*), enzymes involved in the biliary secretion of cholesterol (*Abcg5, Abcg8, Cyp7a*), receptors responsible for lipoprotein uptake (*Ldlr, SrbI, Cd36*), and of enzymes involved in cholesterol synthesis (*Dhcr7* and *Hmgcr*) was determined. Additionally, the expression of scavenger receptors (*SrbI* and *Cd36*) was assessed.

This experiment was carried out in males under baseline conditions in which 8 to 10 weeks old mice on a chow diet were sacrificed when atherosclerosis had not yet developed as well as after 4 weeks and after 16 weeks of WD. At baseline conditions, the expression of cholesterol synthesizing enzymes was increased in *Apoe*$^{-/-}$*Gpr55*$^{-/-}$ mice compared to the *Apoe*$^{-/-}$ control (Figure 14A). During the atherogenic diet, mice with the *Apoe*$^{-/-}$*Gpr55*$^{-/-}$ knockout exhibited an increase in the expression of enzymes responsible for reverse cholesterol transport, indicating an increased turnover of cholesterol (Figure 14B). At the advanced stage of atheroprogression, gene expression did not differ between the groups, except for a decrease in the expression of *Hmgcr* in the *Apoe*$^{-/-}$*Gpr55*$^{-/-}$ group (Figure 14C).

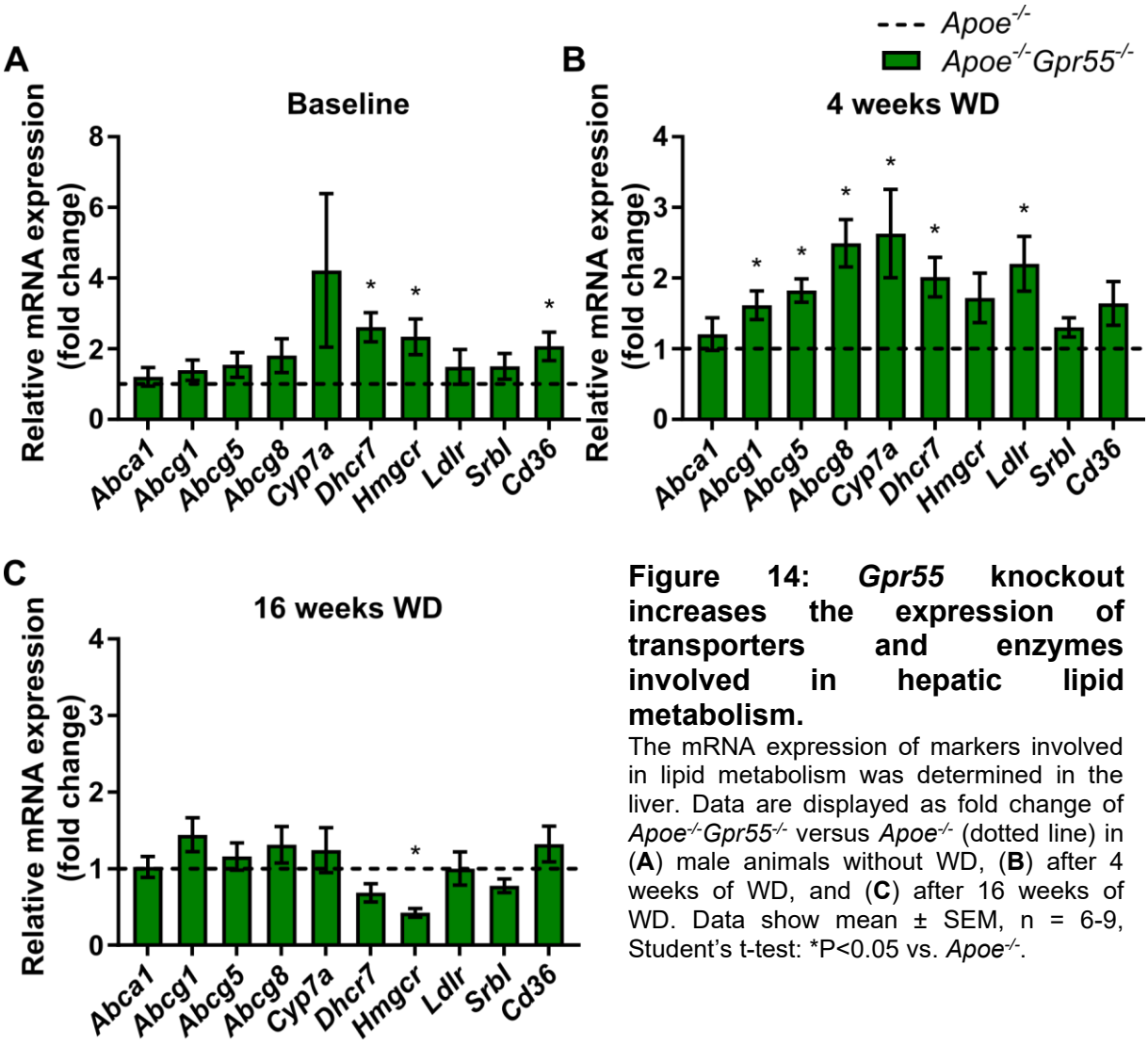

Figure 14: *Gpr55* knockout increases the expression of transporters and enzymes involved in hepatic lipid metabolism.
The mRNA expression of markers involved in lipid metabolism was determined in the liver. Data are displayed as fold change of *Apoe*$^{-/-}$*Gpr55*$^{-/-}$ versus *Apoe*$^{-/-}$ (dotted line) in (**A**) male animals without WD, (**B**) after 4 weeks of WD, and (**C**) after 16 weeks of WD. Data show mean ± SEM, n = 6-9, Student's t-test: *P<0.05 vs. *Apoe*$^{-/-}$.

5.5 *Gpr55* knockout aggravates atherosclerotic plaque burden

WD-fed *Apoe*$^{-/-}$ mice developed atherosclerotic lesions in the aortic root and other predilection sites like the aortic arch, the iliac bifurcation and branch points, increasing throughout the WD treatment. To analyze the effect of the *Gpr55* knockout on lesion development, two different time points were chosen. Mice were sacrificed after 4 weeks of WD during early lesion development and after 16 weeks of WD at an advanced stage. Lesion size was determined by quantifying the ORO-stained lesion area in the aortic root in 6-8 slides at a 50 µm distance from each other and calculating the average per animal (Figures 15 and 16). The total plaque area was then normalized to the length of the IEL to account for vessel size differences of the animals.

At the early stage, *Gpr55* knockout enhanced plaque progression compared to the *Apoe*$^{-/-}$ control group in both male and female mice (Figure 15).

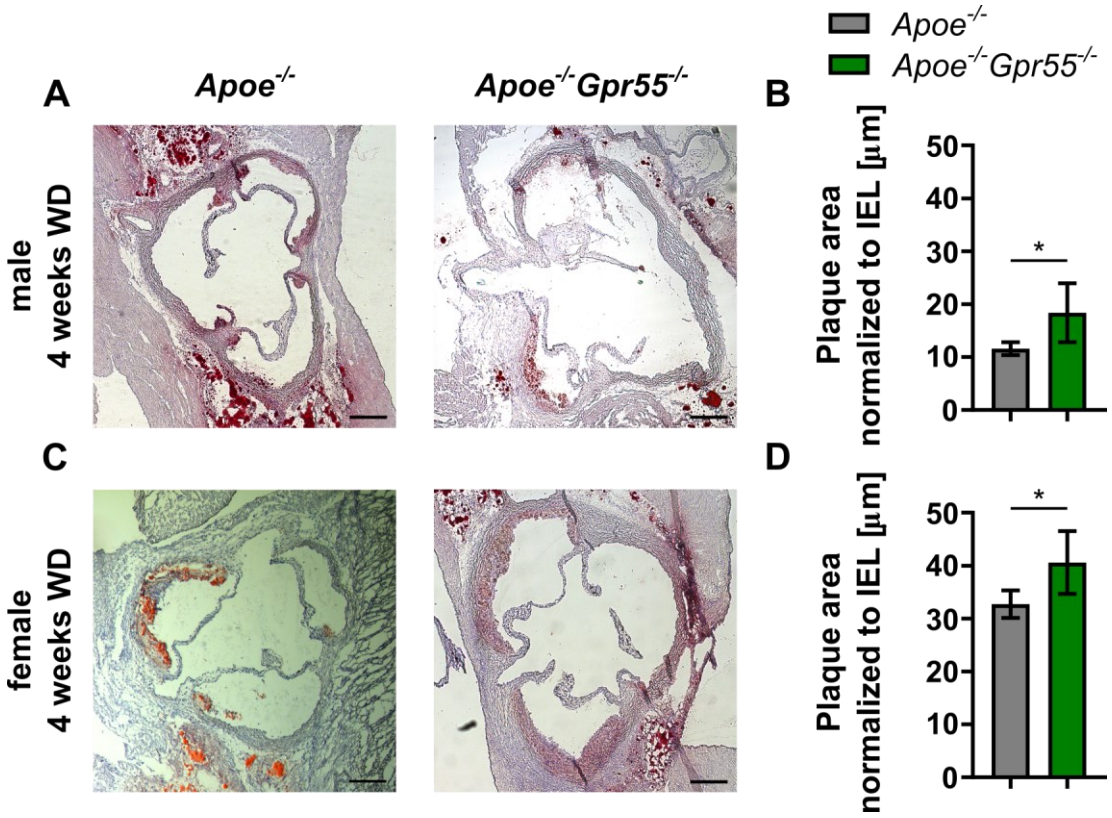

Figure 15 *Gpr55* knockout increases the size of early atherosclerotic lesions.
Plaque size quantification using ORO staining after a 4 week WD treatment period. Representative images of ORO-stained aortic root cross-sections in (**A**) male and (**C**) female animals, respectively. Graphs show quantification of atherosclerotic lesions as total plaque area normalized to the IEL in (**B**) males (n = 7-10) and (**D**) females (n = 11-13). All scale bars indicate 200 µm. Data show mean ± SEM, Student's t-test: *P<0.05 vs. *Apoe*$^{-/-}$.

After 16 weeks of WD treatment, the trend observed in male mice continued. Atherosclerotic plaques of male *Apoe*$^{-/-}$*Gpr55*$^{-/-}$ mice were 1.6-fold larger compared to controls (Figures 16A and B). Conversely, female *Apoe*$^{-/-}$*Gpr55*$^{-/-}$ mice exhibited slightly smaller lesions in the aortic root compared to the corresponding *Apoe*$^{-/-}$ littermates at this time point (Figures 16C and D).

In general, we noted that the aortic root plaques in female mice were larger than males on the same WD treatment regimen. Consistent with existing data[186], the disease seems to develop faster in female *Apoe*$^{-/-}$ mice.

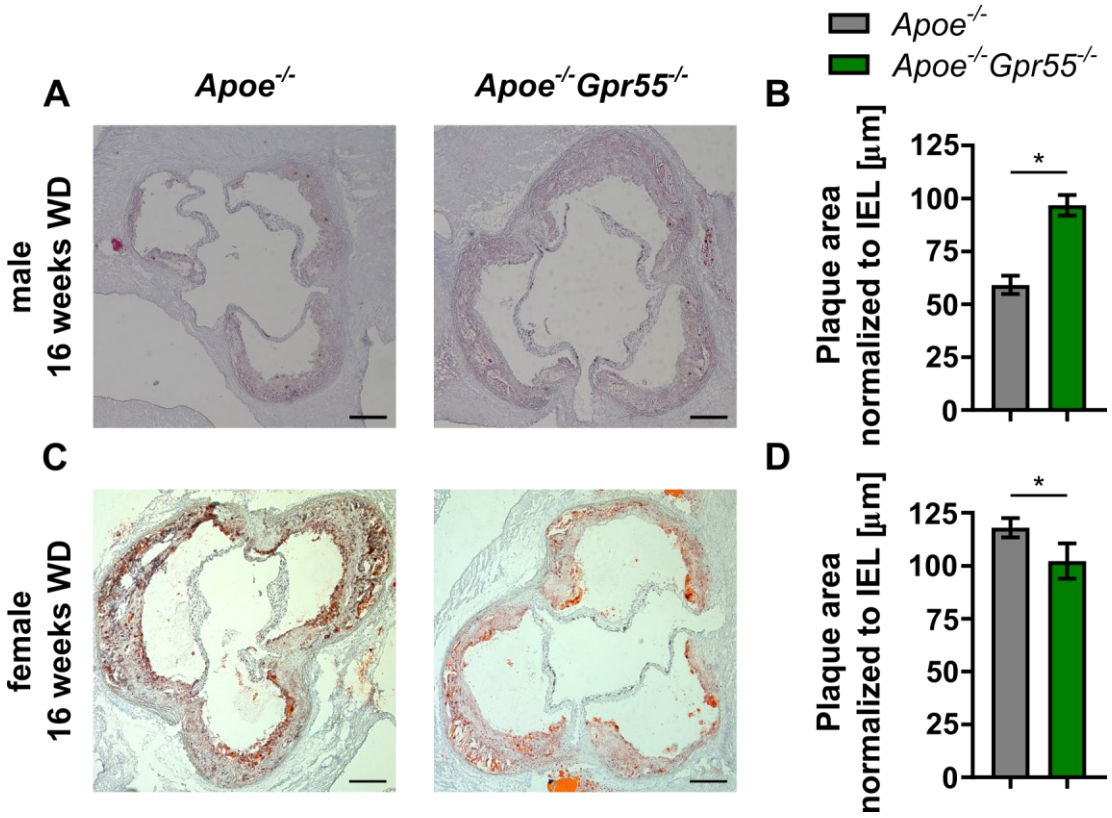

Figure 16: GPR55 influences atherosclerotic lesion size after 16 weeks of WD.
Plaque size quantification using ORO staining after a 16 week WD treatment period. Representative images of ORO-stained aortic root cross-sections in (**A**) male and (**C**) female animals, respectively. Graphs show quantification of atherosclerotic lesions as total plaque area normalized to the IEL in (**B**) males (n = 7-19) and (**D**) females (n = 12-23). All scale bars indicate 200 µm. Data show mean ± SEM, Student's t-test: *P<0.05 vs. *Apoe*$^{-/-}$.

Atherosclerotic lesions were also quantified in the entire descending aorta after en face preparation (Figure 17). This analysis was performed in female mice after the 16-week WD treatment period. There, *Gpr55* knockout resulted in a considerable increase in the number and size of lesions per animal compared to the *Apoe*$^{-/-}$ control group.

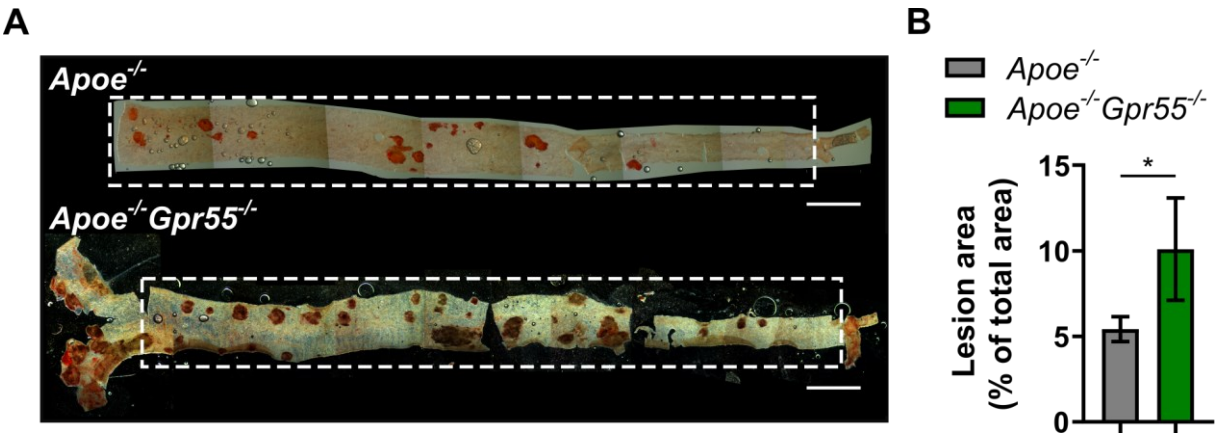

Figure 17: *Gpr55* deficiency aggravates plaque burden after 16 weeks of WD.
(**A**) Representative images of ORO-stained whole aortas of female mice after 16 weeks of WD treatment. The atheromas in the descending aorta up to the iliac bifurcation, here outlined by the dotted areas in white, were evaluated. Scale bars indicate 2 mm. (**B**) Quantitative analysis of ORO-positive lesion area relative to the area of the vessel. Data show mean ± SEM, n = 7-10, Student's t-test: *P<0.05 vs. *Apoe*$^{-/-}$.

5.6 GPR55 impacts atherosclerotic plaque composition

To gain a more detailed understanding of how GPR55 deficiency affected atherosclerotic lesion composition, several histological staining methods for the detection of different cell types and structures in the plaque were used.

Macrophages are the most abundant cell type in the early lesions. The onset of atherogenesis, in this thesis represented by the 4 week WD treatment groups, is primarily shaped by monocyte recruitment to the atheromata[10]. To quantify the lesional macrophage content, immunohistochemistry analysis using Mac2 antibody was performed. Mac2 is a cell surface protein of murine and human macrophages. When comparing aortic root plaques at the early stage of plaque progression, *Apoe*$^{-/-}$ *Gpr55*$^{-/-}$ animals showed more than two-fold higher relative macrophage content per lesion compared to *Apoe*$^{-/-}$ controls (Figure 18A and B). After 16 weeks WD, the relative macrophage content of advanced plaques was significantly lower in the *Apoe*$^{-/-}$*Gpr55*$^{-/-}$ group compared to control (Figure 18C and D). It should be noted, however, that these analyses were performed in female or male mice, respectively, likely representing different plaque maturation stages. It cannot be excluded that the relative macrophage content per plaque may differ depending on the sex of the mice.

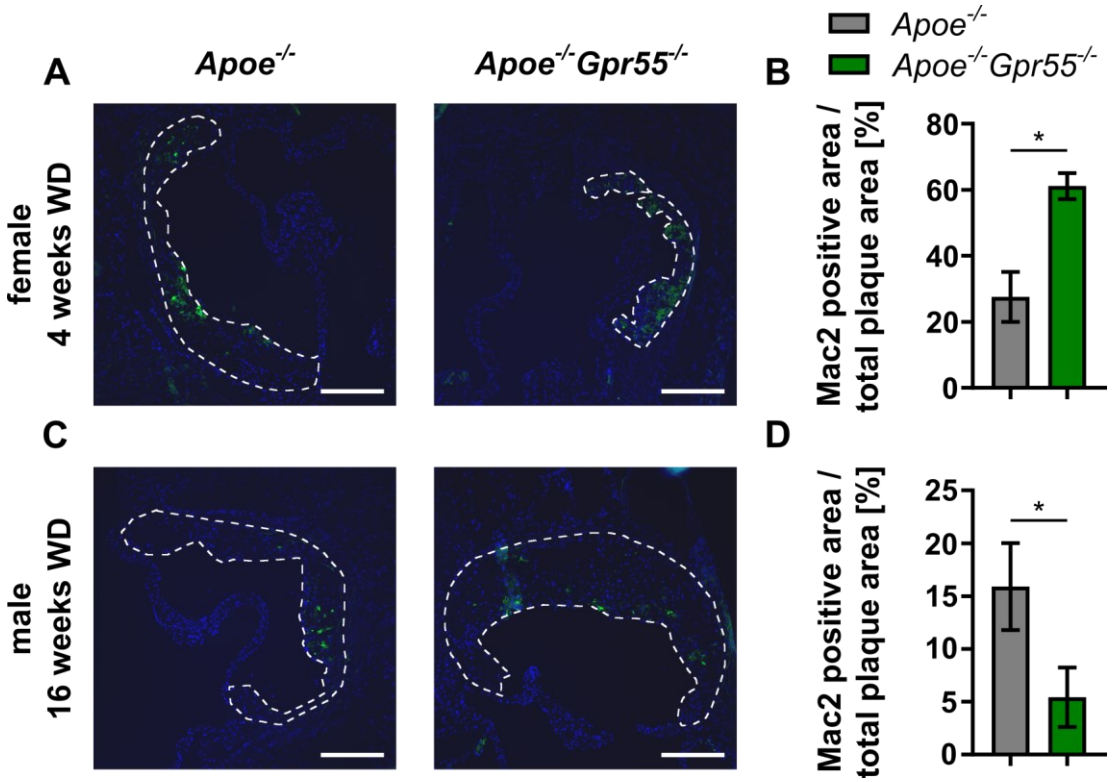

Figure 18: GPR55 affects macrophage content in early and advanced plaques. Relative macrophage content in plaques was determined by staining with Mac2 antibody. Representative Mac2 immunofluorescence-stained images of (**A**) female mice after 4 weeks WD and (**C**) male mice after 16 weeks WD. Quantification of the relative macrophage content after (**B**) 4 and (**D**) 16 weeks WD. The dotted line delineates the plaque area. Green staining corresponds to stained macrophages (Mac2 antibody) and nuclei were stained with Hoechst (blue). Scale bars indicate 200 µm. Data show mean ± SEM, n = 3-5, Student's t-test: *P<0.05 vs. *Apoe*$^{-/-}$.

Collagen fibers are produced by SMCs recruited to the intima and contribute to plaque stability. They play a crucial role in preventing plaque rupture, which leads to acute cardiovascular events. Besides, the stability of an atherosclerotic lesion is determined by destabilizing factors such as large necrotic cores. Collagen content was quantified by Masson trichrome staining only after 16 weeks of WD, as collagen production is a characteristic feature of advanced plaque stages. *Apoe*$^{-/-}$*Gpr55*$^{-/-}$ mice had significantly more collagen deposition in the lesions than the *Apoe*$^{-/-}$ control group (Figure 19).

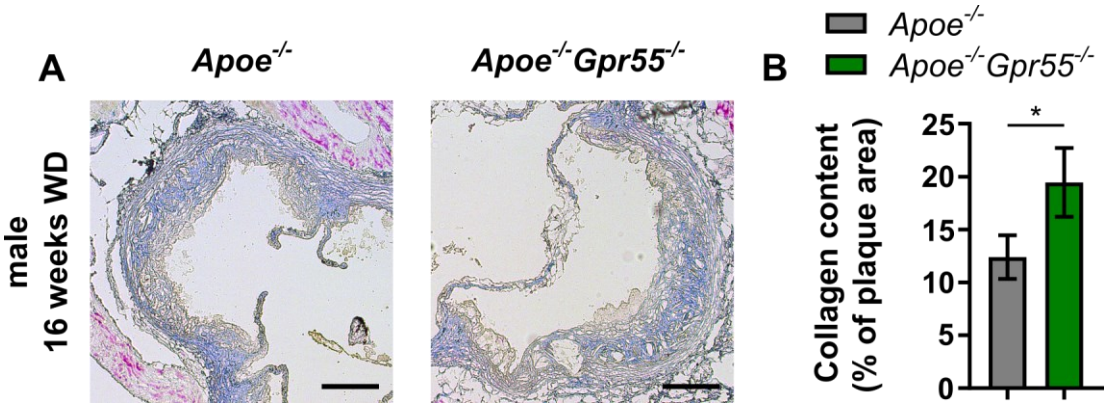

Figure 19: Plaque collagen content increases in *Apoe*$^{-/-}$*Gpr55*$^{-/-}$ animals.
The relative plaque collagen content was examined by staining aortic root cryosections with Masson trichrome. (**A**) Representative images of Masson-trichrome stained aortic root plaques after 16 weeks of WD. Blue staining visualizes collagen fibers. Scale bars indicate 200 µm. (**B**) Quantification of the relative collagen content. Data show mean ± SEM, n = 7-8, Student's t-test: *P<0.05 vs. *Apoe*$^{-/-}$.

Another attribute of large and developed atherosclerotic lesions is the establishment of a necrotic core. Impaired clearance of apoptotic cells, mainly macrophage-derived foam cells, leads to the accumulation of cell debris and cholesterol crystals, forming regions of necrosis within the plaque. In humans, large necrotic cores are associated with vulnerable plaques, which are more prone to rupture. When comparing lesions of *Apoe*$^{-/-}$*Gpr55*$^{-/-}$ animals to the *Apoe*$^{-/-}$ control group, necrotic cores were significantly larger in the *Gpr55* knockout animals (Figure 20). Collagen content, as well as necrotic core size, increased due to GPR55 deficiency, modifying both stabilizing and destabilizing factors, suggesting more advanced and developed plaques.

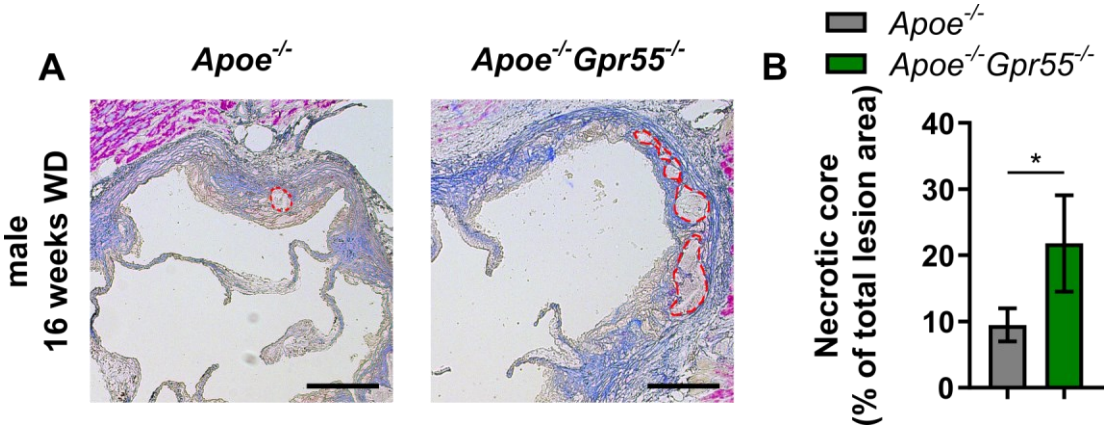

Figure 20: GPR55 deficiency leads to larger necrotic cores in aortic root lesions.
The necrotic core size of aortic sinus plaques was quantified after 16 weeks of WD by measuring the necrotic areas in Masson-trichrome stained sections. (**A**) Representative images of Masson-trichrome stained aortic root sections after 16 weeks WD. Dotted lines show acellular necrotic core area. Scale bars indicate 200 µm. (**B**) Quantification of necrosis relative to the total plaque area. Data show mean ± SEM, n = 6, Student's t-test: *P<0.05 vs. *Apoe*$^{-/-}$.

5.7 *Apoe*$^{-/-}$*Gpr55*$^{-/-}$ animals show enhanced inflammation

5.7.1 *Gpr55* depletion increases leukocyte counts and expression of proinflammatory cytokines in the aorta

Flow cytometry analysis and qPCR analysis of enzymatically digested murine aortas were performed to investigate further the impact of GPR55 deficiency on vascular inflammation linked to atherosclerosis (Figure 21). The number of total lymphocytes, $CD3^+$ T cells, macrophages and neutrophils was determined. Additionally, the relative mRNA expression of inflammatory markers was assessed by flow cytometry (Figure 21A). These results enabled a comparison of local inflammation in *Apoe*$^{-/-}$*GPR55*$^{-/-}$ and control mice. Atherosclerosis begins with the recruitment of leukocytes to the endothelium, which contributes to EC dysfunction and facilitates the inflammatory reaction. In the mouse model, most plaques form along the aorta and this analysis gives an insight into the inflammatory process in this tissue. *Apoe*$^{-/-}$*Gpr55*$^{-/-}$ animals showed increased numbers of lymphocytes, $CD3^+$ T cells and neutrophils after 4 weeks of WD compared to the *Apoe*$^{-/-}$ group (Figure 21B).

While gene expression for most pro-atherogenic cytokines and chemokines tested was unchanged by the *Gpr55* knockout in the early stages, there was a significant transcriptional upregulation of *Ccl5* as opposed to the control group (Figure 21C). Examining the later stages of atheroprogression, *Tnf-α*, *Il-1β*, *Il-6* and *Inos* expression was upregulated after 16 weeks of WD treatment (Figure 21D). These cytokines contribute to increased inflammation in the aorta and are typically secreted by proinflammatory (“M1-type”) macrophages. The anti-inflammatory cytokine IL-10, secreted by alternatively activated (“M2-type”) macrophages and T_H2 cells, plays a role in preventing an excessive immune response. Its gene expression was unchanged compared to the control group at both time points.

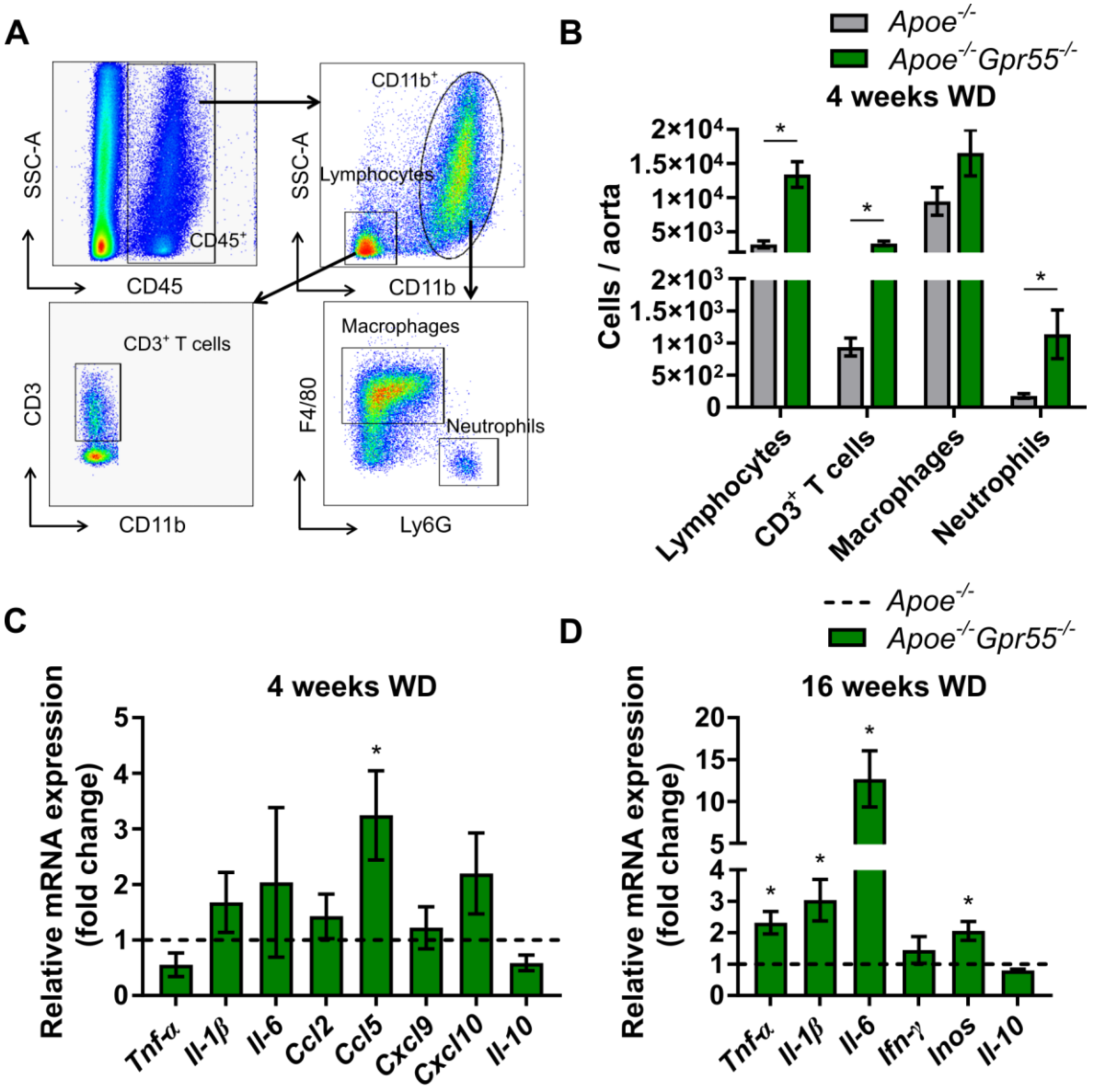

Figure 21: *Gpr55* deficiency increases vascular inflammation.
Flow cytometry analysis of fluorescence-stained aortic cells was used to evaluate the inflammatory processes during atherogenesis. (**A**) Representative gating strategy to identify leukocyte subsets in the aorta and (**B**) quantification after 4 weeks WD in female mice (n = 6-12). (**C, D**) Gene expression of pro- and anti-inflammatory cytokines and chemokines was determined by qPCR using *Hprt* as endogenous control. Data are displayed as fold change of *Apoe*$^{-/-}$*Gpr55*$^{-/-}$ versus *Apoe*$^{-/-}$ (dotted line) in male animals after 4 weeks WD and 16 weeks WD. Data show mean ± SEM, n = 5-11, Student's t-test: *P<0.05 vs. *Apoe*$^{-/-}$.

5.7.2 *Gpr55* knockout increases the number of circulating leukocytes in advanced atherosclerosis

After discovering changes in leukocyte populations in the aorta, leukocyte mobilization to the blood was analyzed. Flow cytometry analysis was performed according to the illustrated gating scheme (Figure 22). T cell populations in the early stages of atherosclerosis in male mice, except for the γδTCR$^+$ T cells, were not influenced (Figure 23A). However, *Gpr55* knockout led to an increase in the overall

number of CD3⁺ T cells in males after feeding a WD for 16 weeks (Figure 23B) and there was a significant rise in the number of circulating T cell subsets in female *Apoe*$^{-/-}$*Gpr55*$^{-/-}$ mice in contrast to their *Apoe*$^{-/-}$ controls at both time points (Figure 23C and D). Interestingly, the γδTCR⁺ population was increased in all *Apoe*$^{-/-}$*Gpr55*$^{-/-}$ regardless of gender or disease progression. The number of circulating B220⁺ B cells was unchanged between groups for the scenarios tested.

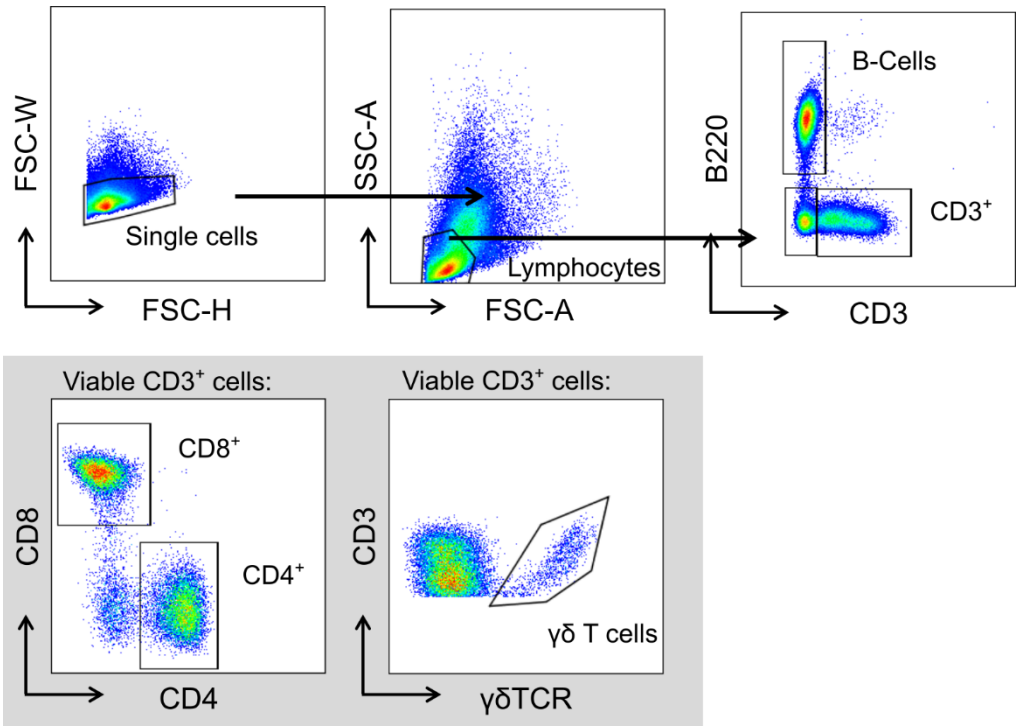

Figure 22: Gating strategy to identify leukocytes in blood samples
Representative flow cytometry gating strategy to identify leukocyte subsets in blood samples of *Apoe*$^{-/-}$ and *Apoe*$^{-/-}$*Gpr55*$^{-/-}$ mice after feeding a WD for 4 or 16 weeks.

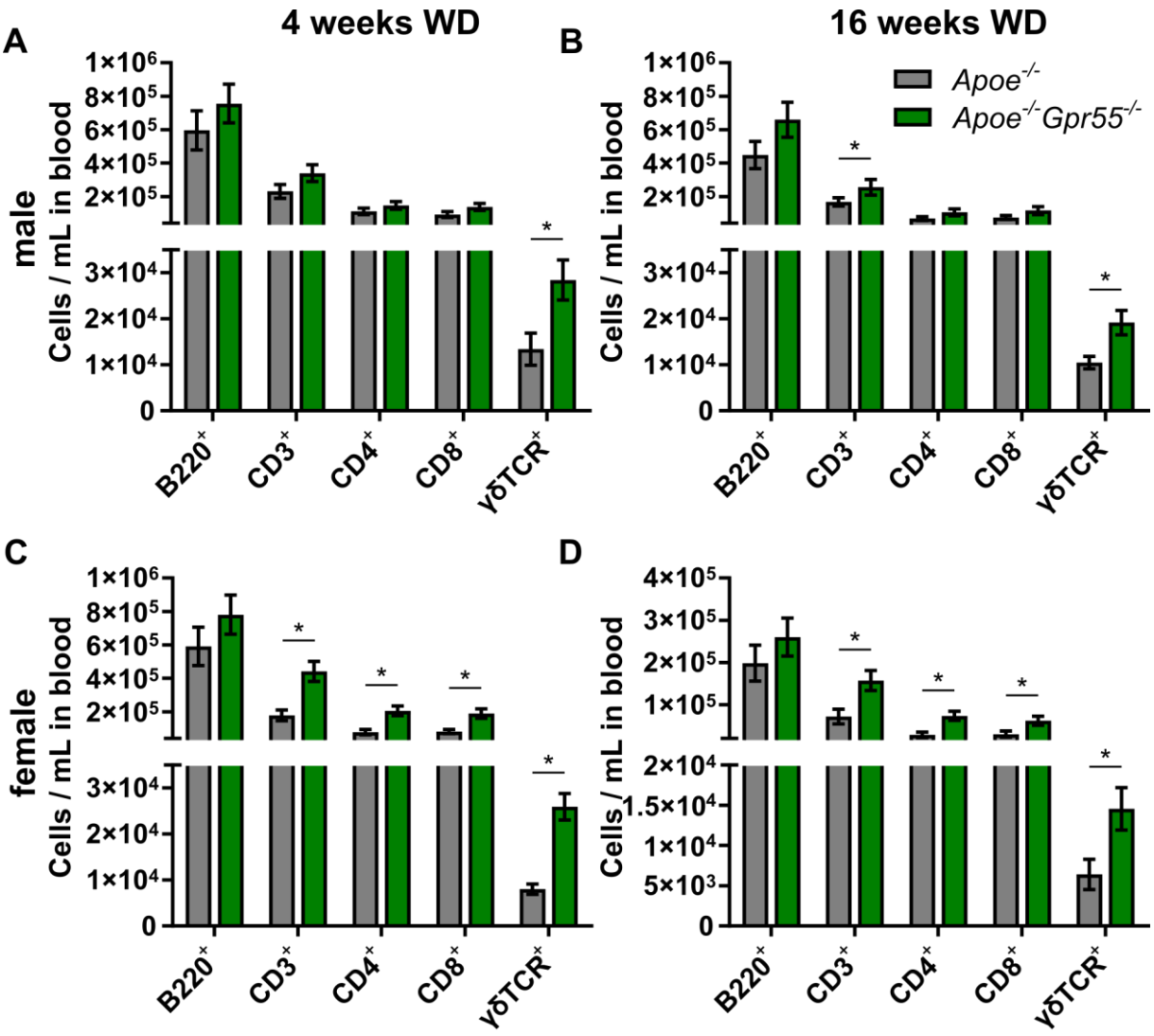

Figure 23: *Gpr55* knockout increases the levels of circulating leukocytes.
Flow cytometry analysis of fluorescence-stained blood samples was used to quantify the number of leukocytes in the circulation. Quantification in male mice after feeding a WD for (**A**) 4 or (**B**) 16 weeks (n = 9-17). (**C, D**) The same data were also collected in female animals (n = 11-16). Data show mean ± SEM, Student's t-test: *P<0.05 vs. *Apoe*$^{-/-}$.

5.7.3 GPR55 depletion increases T-cell numbers in secondary lymphoid organs

The spleen serves as a regulator of innate and adaptive immunity and is involved in the mobilization and redistribution of lymphocytes to non-lymphoid tissues. Because GPR55 is highly expressed on B and T cells (Figure 11), the distribution of lymphocyte subsets in the spleen and secondary lymphoid organs was investigated in depth. Flow cytometry analysis did not reveal changes in lymphocyte populations in early atherogenesis. However, *Gpr55* deficiency resulted in elevated cell counts of B and T cell subsets after 16 weeks of WD compared to control (Figure 24).

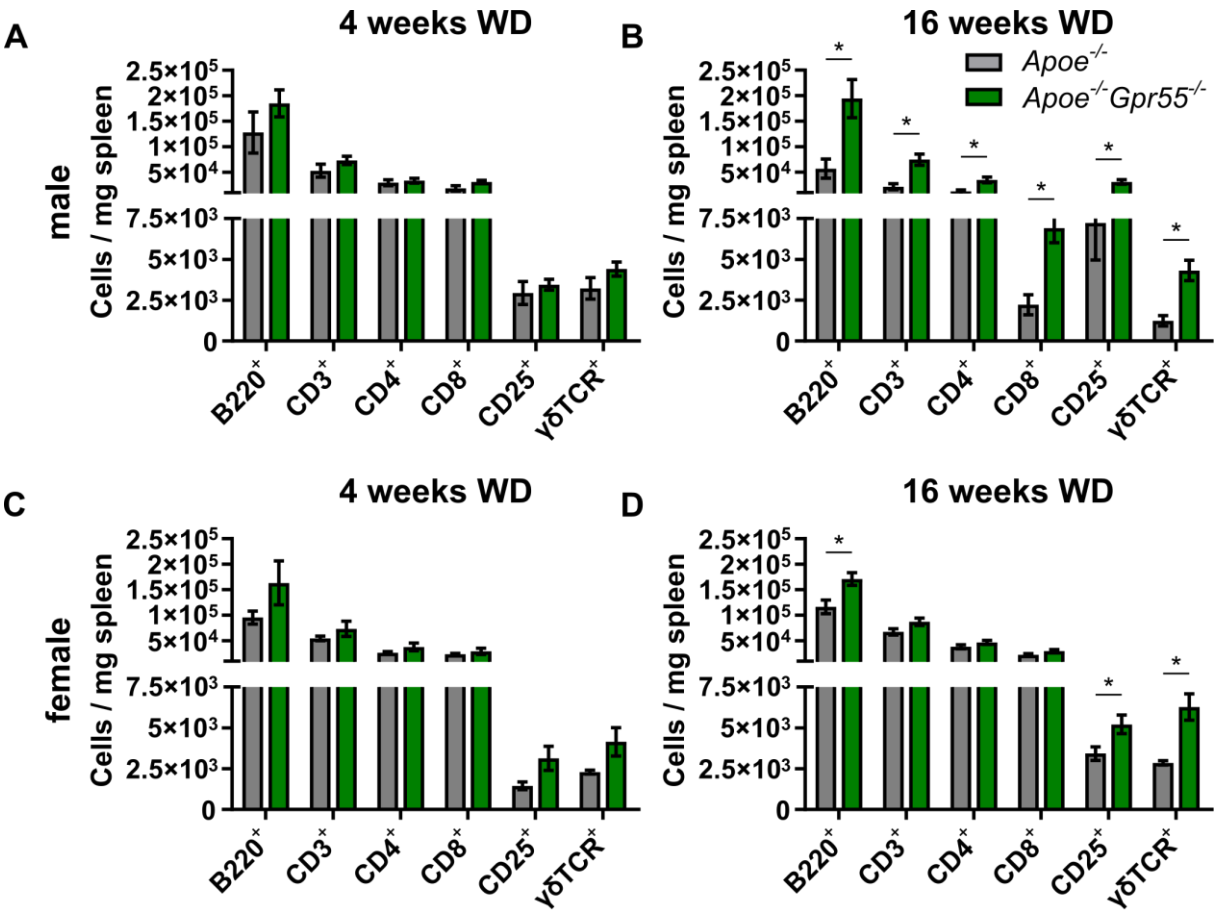

Figure 24: *Gpr55* deficiency increases splenic lymphocyte numbers in advanced atherosclerosis.
Mice were fed a WD for 4 or 16 weeks before different leukocyte subsets in the spleen were characterized using flow cytometry. Quantification of $B220^+$ B cells and different T cell subsets was performed in (**A, B**) male and (**C, D**) female mice after 4 and 16 weeks of WD, respectively. Data show mean ± SEM, n = 5-14, Student's t-test: *P<0.05 vs. *Apoe*$^{-/-}$.

Although *Apoe*$^{-/-}$*Gpr55*$^{-/-}$ mice presented with increased numbers of splenic lymphocytes, the expression pattern of pro- and anti-inflammatory genes was comparable between the groups (Figure 25).

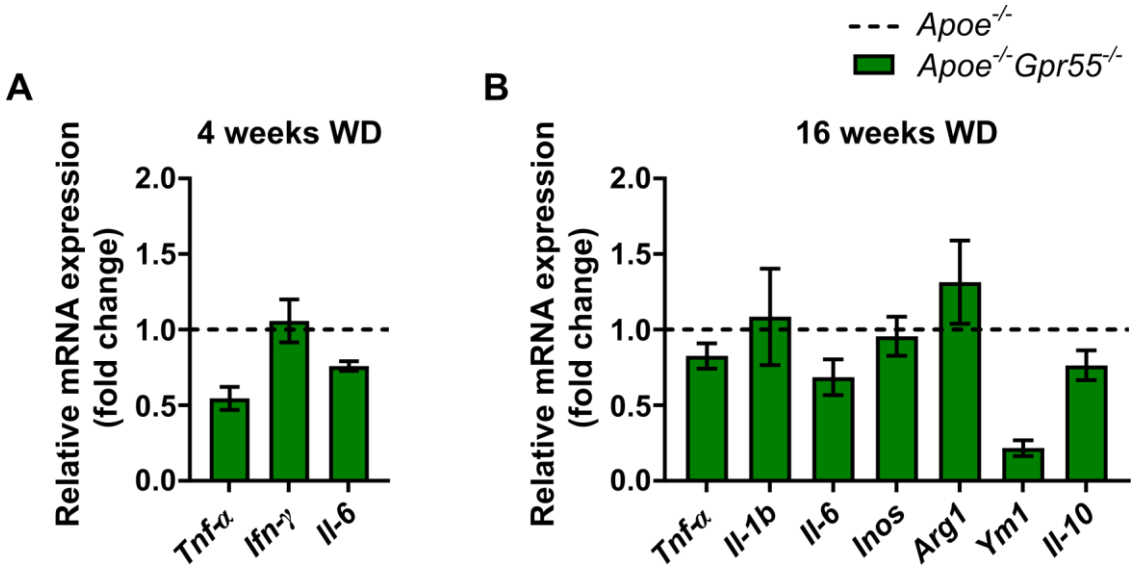

Figure 25: *Gpr55* deficiency does not significantly alter the expression of pro- and anti-inflammatory genes in the spleen.
The gene expression of pro- and anti-inflammatory markers in the spleen was determined by qPCR using *Hprt* as endogenous control. Data are displayed as fold change of *Apoe*$^{-/-}$*Gpr55*$^{-/-}$ versus *Apoe*$^{-/-}$ (dotted line) in male animals after (**A**) 4 weeks of WD and (**B**) 16 weeks of WD. Data show mean ± SEM, n = 6-12, Student's t-test: *P<0.05 vs. *Apoe*$^{-/-}$.

Lymph nodes are a site for adaptive immune responses involving antigen-specific lymphocyte reactions during inflammation. Since atherosclerosis is a chronic inflammatory process and mice develop plaques along the aorta, the number of leukocytes in paraaortic lymph nodes was analyzed (Figure 26). At the later stages of the disease, *Gpr55* knockout resulted in a significant increase in the overall number of T cells and the CD8$^+$ cytotoxic T cell subset in particular. The number of γδTCR$^+$ cells in the paraaortic lymph nodes of these animals was also higher than in the control animals.

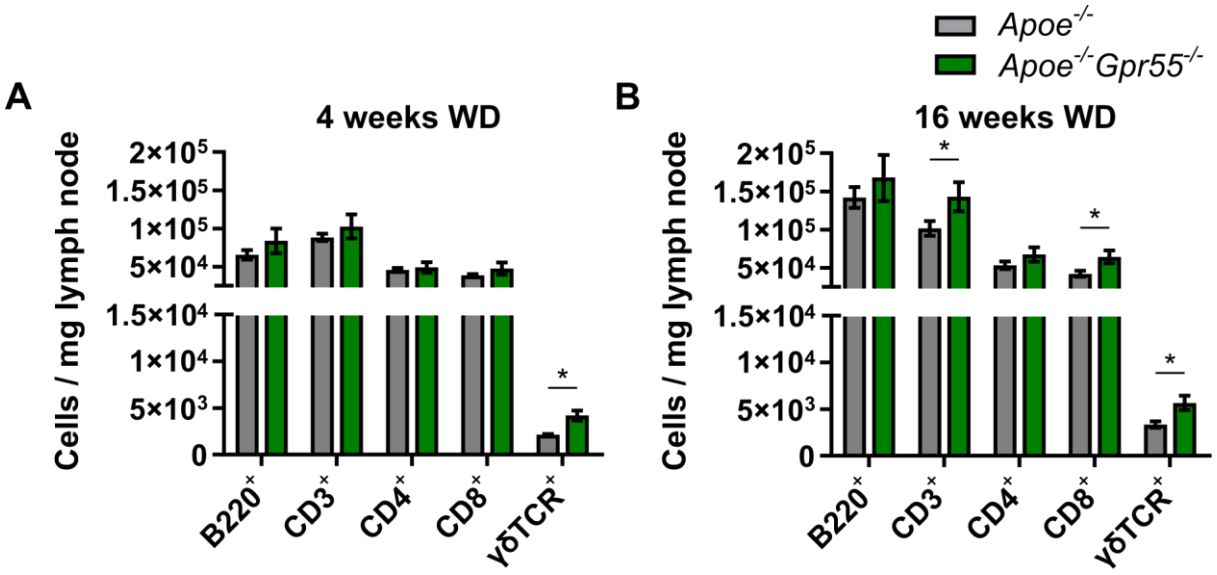

Figure 26: *Gpr55* depletion increases lymphocyte subsets in paraaortic lymph nodes.
Flow cytometry analysis of fluorescence-stained lymph nodes to quantify the number of leukocyte populations. (**A**) Quantification of leukocyte subsets after 4 and (**B**) 16 weeks of WD in female mice. Data show mean ± SEM, n = 7-12, Student's t-test: *P<0.05 vs. *Apoe*$^{-/-}$.

5.7.4 B cell polarization and immunoglobulin production is dependent on GPR55

To assess the impact of GPR55 in regulating B cell distribution in different compartments, flow cytometry analysis of B cell subsets was performed in the circulation and secondary lymphoid organs of the knockout mice (Figure 27). Having observed an upregulated gene expression of *Gpr55* during early atherogenesis but not in the later stages (Figure 10), the 4-week WD time point was chosen for further analysis.

B cell subsets derived from the spleen, paraaortic lymph nodes and the blood were analyzed by flow cytometry (Figure 27A). GPR55 deficiency reduced the number of atheroprotective B1a and B1b cells in the spleen compared to the control group (Figure 27B). *Apoe*$^{-/-}$*Gpr55*$^{-/-}$ animals displayed a significant shift in cell counts from follicular B2 cells (B2 FO) to marginal zone B2 (B2 MZ) cells in the spleen and lymph nodes (Figure 27C and D). In contrast, B cell subsets in the blood did not show significant differences between the groups (Figure 26E). When calculating the relative distribution among 1B cell subsets (Figure 28), *Gpr55* deficient mice showed a reduced B1a and increased pro-atherogenic B1b cell subset in the spleen. The relative proportion of B2 cell subsets within secondary lymphoid organs was altered towards a decreased frequency of FO B2 cells and a relative increase of pro-atherogenic MZ B2 cells during the onset of atherosclerosis.

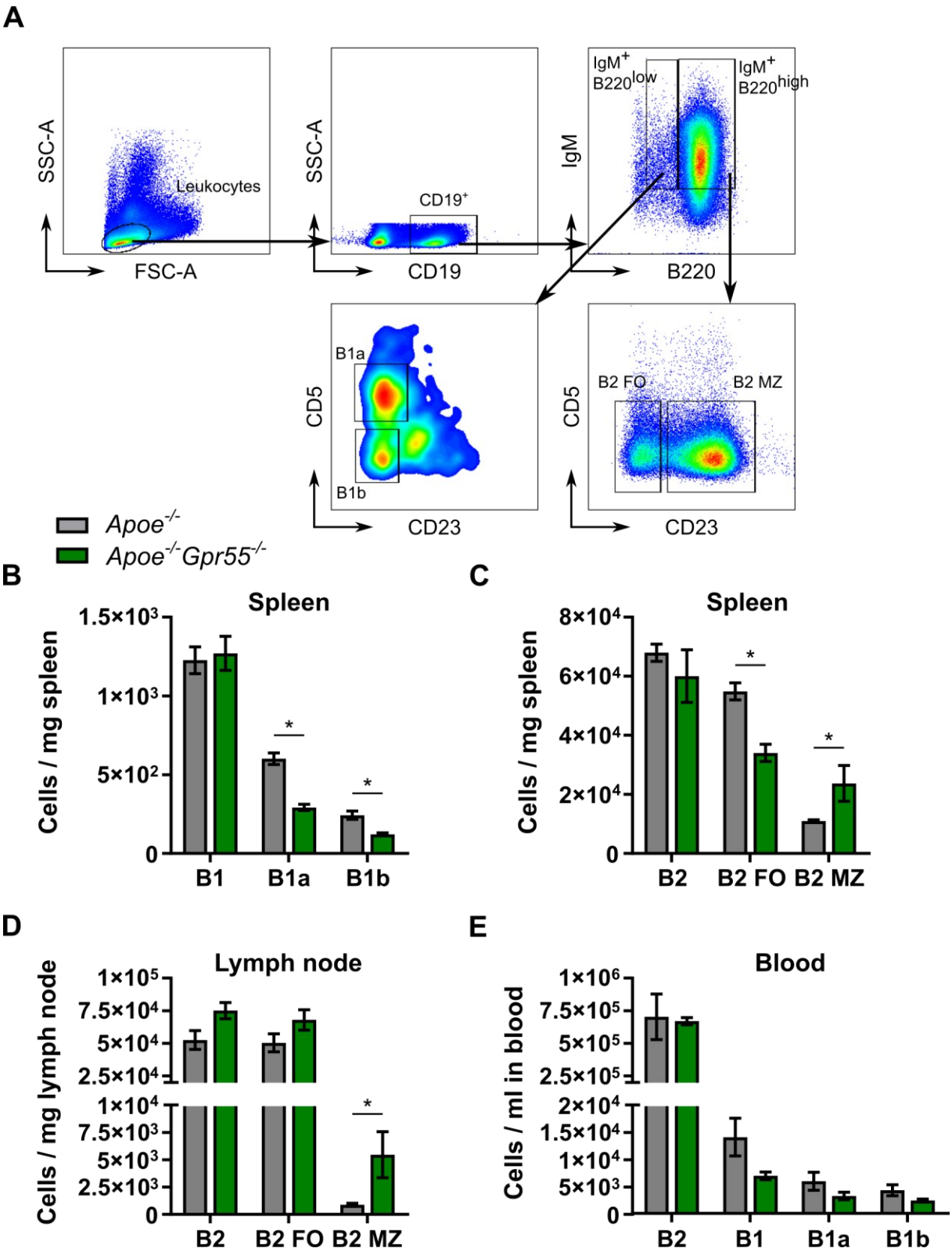

Figure 27: B cell subsets are altered by *Gpr55* knockout.
Flow cytometry analysis of antibody-stained splenocytes, lymph nodes and whole blood cells after 4 weeks WD in female mice was used to determine B cell subset distribution. (**A**) Representative gating strategy to identify B cell subsets in the spleen. B1a cells were defined as $CD19^{+}IgM^{+}B220^{low}CD5^{+}CD23^{-}$, B1b cells as $CD19^{+}IgM^{+}B220^{low}CD5^{-}CD23^{-}$, B2 FO were gated as $CD19^{+}IgM^{+}B220^{high}CD5^{-}CD23^{-}$, and B2 MZ as $CD19^{+}IgM^{-}B220^{high}CD5^{-}CD23^{+}$. (**B**) Quantification of B1 and (**C**) B2 cells in the spleen (n = 4-7). (**D**) B cell subsets in paraaortic lymph nodes and (**E**) blood (n = 4-6). Data show mean ± SEM, Student's t-test: *P<0.05 vs. *Apoe*$^{-/-}$.

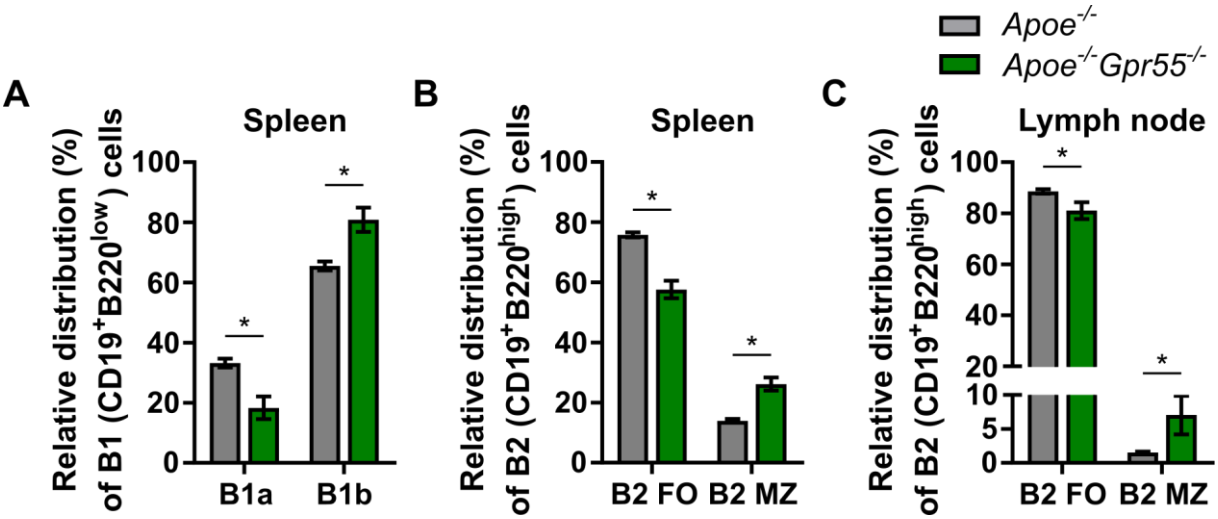

Figure 28: GPR55 deficiency alters the relative distribution of B cell subsets.
The relative distribution of B cell subsets was analyzed in secondary lymphoid organs of female mice after 4 weeks of WD. (**A**) Quantification of B1 cell subsets in the spleen (n = 5-7), (**B**) B2 cell subsets in the spleen (n = 5-7) and (**C**) in paraaortic lymph nodes (n = 4-6). Data show mean ± SEM, Student's t-test: *P<0.05 vs. *Apoe*$^{-/-}$.

When examining plasma immunoglobulins, it was found that even baseline *Gpr55* deficient mice without receiving the atherogenic diet already presented with remarkable differences. *Gpr55* depletion increased the amount of circulating IgG1 while reducing the number of IgA, IgE and IgG2b (Figure 29A). After early atherosclerotic lesions had formed, the antibody titers of IgA, IgG1 and IgG2c were still elevated in the *Apoe*$^{-/-}$*Gpr55*$^{-/-}$ group, while the other immunoglobulins remained at levels comparable to corresponding *Apoe*$^{-/-}$ controls (Figure 29B and C).

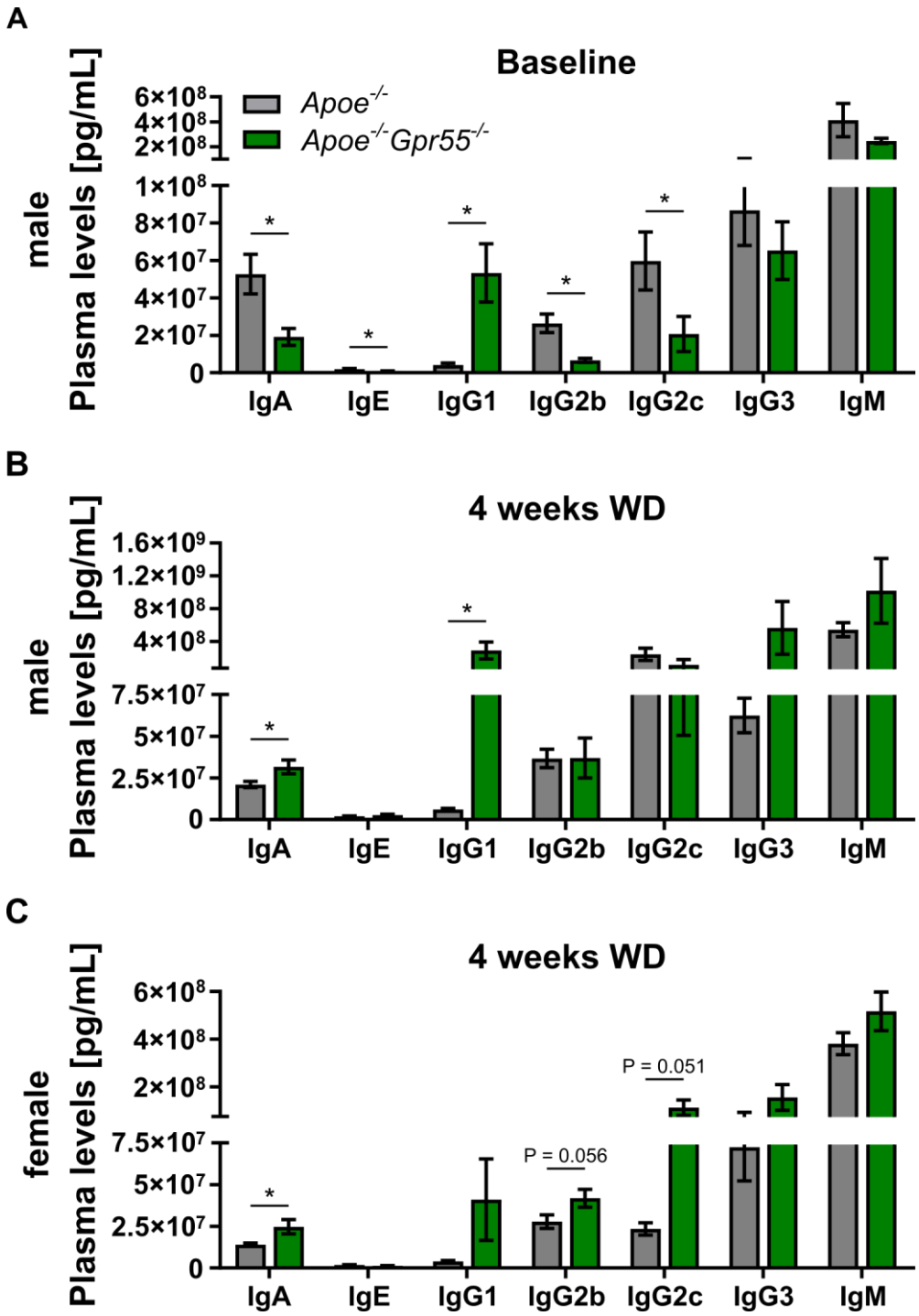

Figure 29: Specific immunoglobulin subsets in the circulation are elevated due to *Gpr55* knockout.

The graph shows a detailed analysis of immunoglobulins in plasma of *Apoe*$^{-/-}$ and *Apoe*$^{-/-}$*Gpr55*$^{-/-}$ mice in (**A**) males under baseline conditions, (**B**) in males and (**C**) females after 4 weeks of WD. Data show mean ± SEM, n = 7-10, Student's t-test: *P<0.05 vs. *Apoe*$^{-/-}$.

5.7.5 GPR55 deficiency enhances myeloid cell counts in early atherosclerosis

Furthermore, bone marrow was collected from murine femurs and analyzed by flow cytometry (Figure 30). The gating strategy to identify monocyte subsets in all samples is displayed in Figure 30A. This experiment revealed a significant increase in the number of monocytes in mice that lack GPR55 after feeding the WD for 4 weeks in both sexes (Figure 30B and D). Surprisingly, after 16 weeks of WD, there were no significant differences in myeloid cell counts observed between groups in males (Figure 30C). However, there was a reduction in the counts of monocytes detected in the bone marrow in female *Apoe*$^{-/-}$*Gpr55*$^{-/-}$ mice (Figure 30E). Despite neutrophils being more strongly recruited to the aortas of mice lacking GPR55 (Figure 21B), no alterations in neutrophil numbers in the bone marrow were found.

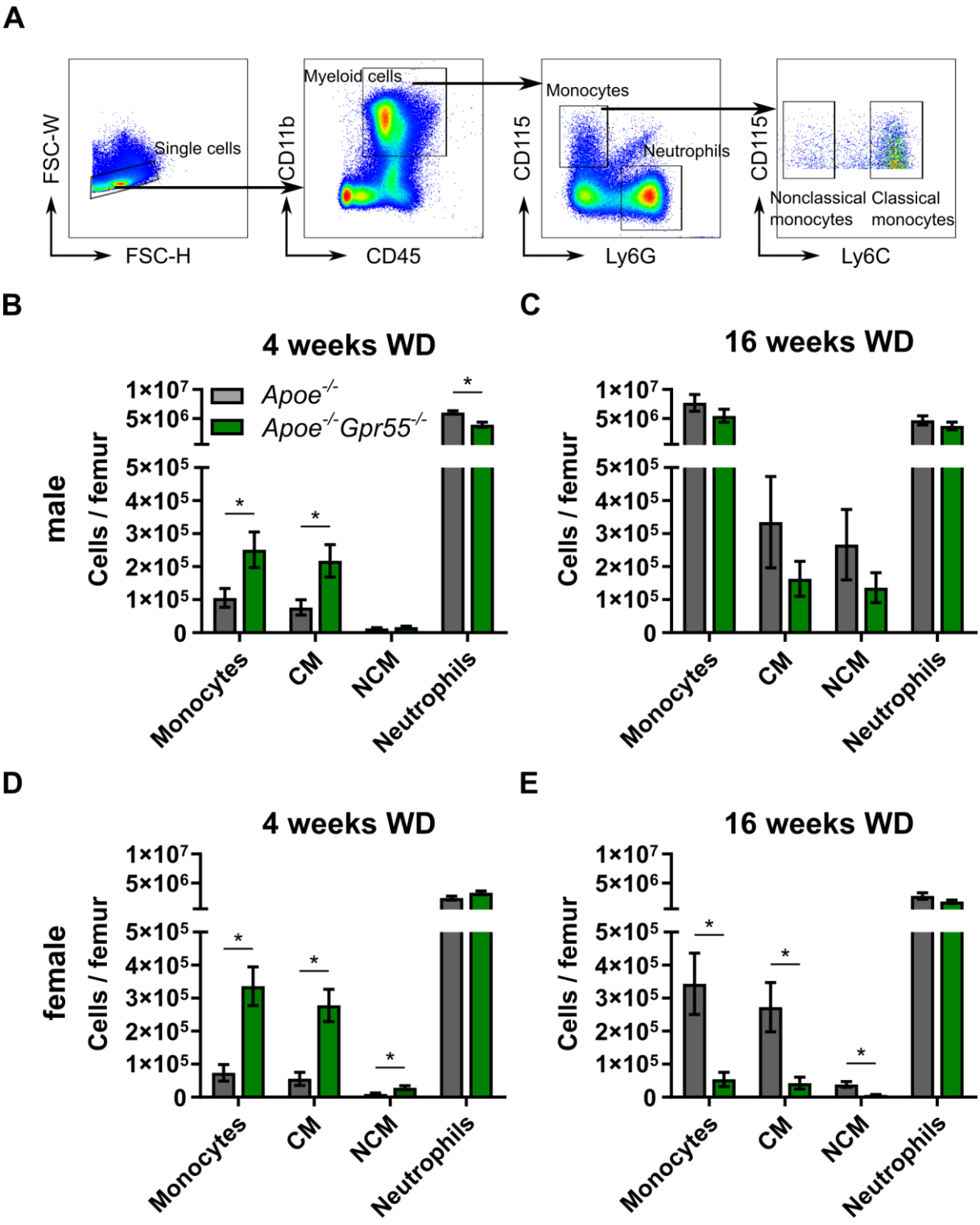

Figure 30 *Gpr55* knockout increases bone marrow monocyte cell counts during early atherosclerosis

Flow cytometry analysis of antibody-stained bone marrow cells after 4 and 16 weeks of WD was used to determine the number of myeloid cell subsets. (**A**) Representative gating strategy: myeloid cells were defined as $CD45^+CD11b^+$, classical monocytes (CM) as $CD45^+CD11b^+Ly6G^-Ly6C^{high}$ and nonclassical monocytes (NCM) as $CD45^+CD11b^+Ly6G^-Ly6C^{low}$. Neutrophils were determined as $CD45^+CD11b^+Ly6G^+$. Quantification of myeloid cell subsets in male mice after (**B**) 4 weeks and (**C**) 16 weeks of WD. Quantification of the myeloid cell subsets in female mice after (**D**) 4 or (**E**) 16 weeks of WD. Data show mean ± SEM, n = 7-14, Student's t-test: *P<0.05 vs. *Apoe*$^{-/-}$.

5.8 *In vitro* studies of leukocyte subsets

So far, the data show that the absence of GPR55 altered lesional macrophage content and increased monocyte counts in the bone marrow. To further understand the role of GPR55 in macrophages, additional *in vitro* experiments were conducted. Given the high *Gpr55* expression in NK cells, functional assays were also performed with this leukocyte subset.

5.8.1 *Gpr55* knockout increases the uptake of oxLDL by bone marrow-derived macrophages *in vitro*

After having determined increased recruitment of monocytes and macrophages to the atherosclerotic plaques in *Apoe*$^{-/-}$*Gpr55*$^{-/-}$ mice, an *in vitro* experiment with isolated macrophages was designed to clarify whether GPR55 changes the modified LDL uptake capacity. Therefore, cultured BMDM of *Apoe*$^{-/-}$ and *Apoe*$^{-/-}$*Gpr55*$^{-/-}$ mice were equally treated with fluorescence-labeled oxLDL for 24 h and subsequently analyzed by flow cytometry. This experiment was carried out three times with different donor mice. The amount of oxLDL was increased in *Apoe*$^{-/-}$*Gpr55*$^{-/-}$ BMDM compared to the control group (Figure 31).

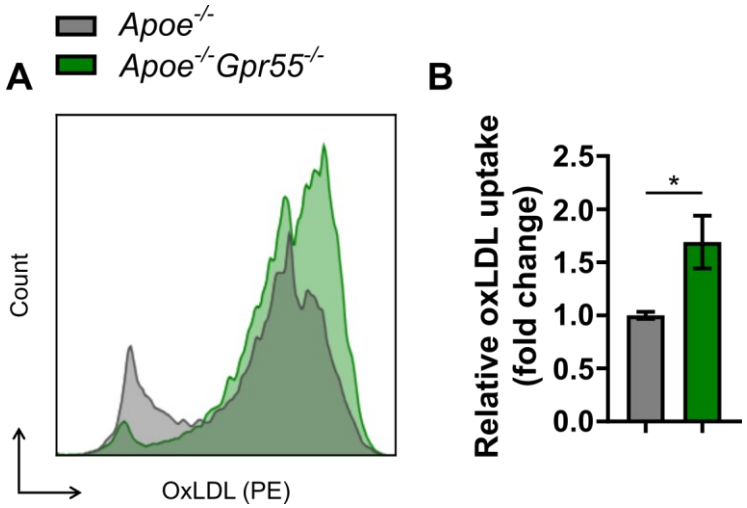

Figure 31: *Gpr55* knockout potentiates the uptake of oxLDL by macrophages *in vitro*.
The ability of cultured macrophages to engulf modified lipoproteins was assessed *in vitro*, measuring the uptake of fluorescence-labeled oxLDL by flow cytometry. The amount of oxLDL taken up was quantified via geometric MFI in macrophages derived from *Apoe*$^{-/-}$ and *Apoe*$^{-/-}$*Gpr55*$^{-/-}$ mice. The MFI of macrophages loaded with oxLDL was determined in three individual experiments. (**A**) Display of oxLDL uptake expressed as geometric MFI. (**B**) Quantification of oxLDL uptake in BMDM derived from *Apoe*$^{-/-}$*Gpr55*$^{-/-}$ mice, displayed as fold change vs. *Apoe*$^{-/-}$ control. Data show mean ± SEM, Student's test: *P<0.05.

5.8.2 NK cell activation and cytotoxicity are not affected by the lack of GPR55

GPR55 is expressed on NK cells and GPR55 agonist-stimulated NK cells showed increased cytotoxicity[135]. To assess whether *Gpr55* knockout affects NK cell activity, the surface expression of the NK cell activation marker CD107a was determined by flow cytometry after stimulating splenocytes of WT or *Gpr55*$^{-/-}$ mice with IL-2 *in vitro* (Figure 32). The expression of CD107a correlates with cytokine secretion as well as the cytotoxic activity of NK cells[187]. Splenocytes were chosen because of their relatively large number of resident NK cells. First, the stimulation was tested at different concentrations of IL-2 (10, 100, and 1000 U). As expected, IL-2 treatment resulted in the upregulation of CD107a surface expression on NK cells (Figure 32 A). However, stimulating isolated splenocytes of WT and *Gpr55*$^{-/-}$ mice with 100 U IL-2 revealed that the activation pattern did not differ significantly between the two groups (Figure 32B and C).

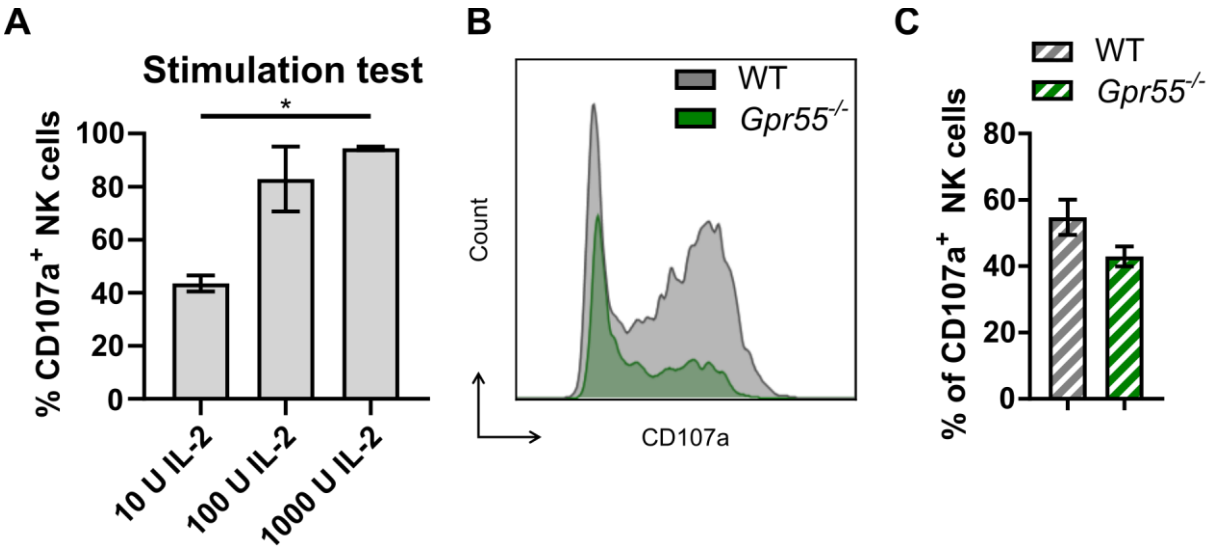

Figure 32: *Gpr55* knockout does not impact NK cell activation marker expression following IL-2 stimulation.
The impact of GPR55 on the activation of NK cells *in vitro* was determined by the relative expression of CD107a after stimulating the cells with IL-2. (**A**) Stimulatory effects of IL-2 on NK cells were determined at different concentrations. IL-2 was able to activate NK cells in a concentration-dependent manner. Data show mean ± SEM, n = 2. One-way ANOVA followed by Bonferroni multiple comparison test: *P<0.05. (**B**) Display of CD107a expression on NK cells after stimulation. (**C**) The difference in NK cell activation was quantified as the percentage of CD107a^{+} NK cells of all CD3^{-}CD49b (DX5)$^{+}$ NK cells. The experiment was carried out twice, n = 2 per group for each experiment. Data show mean ± SEM, Student's t-test: *P<0.05.

In addition, the cytotoxic properties of NK cells were analyzed *in vitro*. The murine lymphoma cell line YAC-1, which is sensitive to the cytotoxic action of NK cells, was incubated with NK cells isolated from WT or *Gpr55*$^{-/-}$ splenocytes. The amount of released LDH was determined as an indicator to calculate the cytotoxic NK cell

activity. In this experimental assay, *Gpr55* knockout had no impact on NK cell target cell lysis activity compared to the *Gpr55* WT expressing cells (Figure 33).

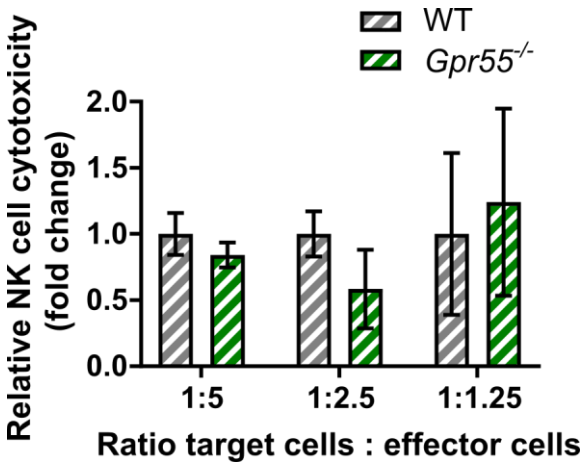

Figure 33: No differences in NK cell cytotoxic activity attributable to GPR55.
Cytotoxicity was calculated using a colorimetric assay quantifying LDH release that occurred due to NK cell-mediated lysis of YAC-1 target cells. The data are displayed as fold change vs. WT. The ratio of NK cells to target cells was 1:5, 1:2.5 and 1:1.25, respectively. The experiment was carried out twice, n = 2 per group for each experiment. Data show mean ± SEM.

Taken together, these *in vitro* experiments revealed no significant impact of GPR55 deficiency on the activity and cytotoxicity of NK cells.

6 DISCUSSION

Atherosclerosis is the leading cause of CVDs, and to date, treatment options are limited. There is no alternative to prevent or reduce atherosclerotic plaque burden other than using lipid-lowering drugs and living a healthy lifestyle. Previous studies identified GPR55 as a receptor that is expressed throughout the body and is involved in various physiological and pathophysiological processes. These include leukocyte subsets that play a role in atherosclerosis. So far, two studies have already suggested an effect of GPR55 signaling on atherosclerosis. However, this thesis goes further than the publications of Lee et al.[177] and Montecucco et al.[152] in terms of animal models and methods used to elucidate the possible influence of GPR55 signaling on the pathogenesis of atherosclerosis. This work primarily used a murine model of atherosclerosis with a constitutive GPR55 knockout.

6.1 Hypercholesterolemia activates the LPI/GPR55 axis

WD feeding of atherosclerosis-prone *Apoe*$^{-/-}$ mice for 4 weeks resulted in an increase in the amount of circulating LPI and an upregulated mRNA expression of splenic *Gpr55* and *Ddhd1*. Transcriptional *Gpr55* expression in the aorta behaved similarly and was highest in the initial stages of disease progression. This activation decreased to initial values when the disease proceeded to a later stage. These results hint towards GPR55 activation during the onset of atherosclerosis and being most impactful in this phase of the disease. We can speculate that the cell types releasing the ligand and expressing the receptor expand during early atherogenesis and subsequently decrease in number. Alternatively, the expression levels of *Ddhd1* and *Gpr55* are downregulated at the advanced stage. It remains to be investigated which cells mainly express LPI and how the generation of the endogenous ligand is regulated.

The effect of the GPR55 deficiency was then assessed at different stages of disease development by examining mice that received WD for 4 or 16 weeks, respectively, and young mice that were kept on chow diet as the baseline.

6.2 GPR55 is expressed in metabolically active tissues and influences body weight and lipid metabolism

Other studies have already demonstrated the importance and regulatory function of GPR55 in metabolism and body weight[156,164]. In this thesis, GPR55 deficiency resulted in distinct metabolic changes. The increase in body weight observed in mice lacking GPR55 was comparable to the data obtained by others[156,164]. In the male cohorts, *Gpr55* knockout resulted in higher plasma cholesterol levels compared to controls, implicating a greater risk for developing atherosclerotic lesions.

A more detailed analysis of hepatic mRNA expression of genes that play a role in lipid metabolism identified upregulation of metabolic markers during early atherogenesis in mice lacking GPR55. These results indicate enhanced cholesterol synthesis, resulting in increased plasma cholesterol levels, as well as enhanced hepatic free fatty acid uptake and efflux. In advanced atherosclerosis, however, the hepatic lipid metabolism appeared to be similar between the groups. In conclusion, GPR55 might protect against excessive cholesterol synthesis and free fatty acid uptake during the initial stages of lesion development. However, these results are controversial compared to recent outcomes of a study examining liver lipid accumulation in mice fed a high-fat diet and treated with GPR55 agonists and antagonists. Kang et al. found increased hepatic steatosis in response to activated GPR55 signaling[188]. The difference in results might be attributed to the different experimental models. While all mice in our experiment had an *Apoe*$^{-/-}$ background and *Gpr55* was knocked out globally, Kang et al. used WT mice in which GPR55 was influenced by pharmacological methods. Additional analysis should be performed in mice with functional Apoe receptors to distinguish between GPR55- and possible Apoe-mediated effects.

6.3 *Apoe*$^{-/-}$*Gpr55*$^{-/-}$ animals exhibit accelerated atherosclerotic lesion progression

To quantify disease severity, atherosclerotic plaques were examined in the aortic roots of all animals fed a WD. Moreover, plaque development in the whole aorta of female mice after 16 weeks of WD feeding was analyzed. Mice depleted in GPR55 showed significantly larger aortic root lesions compared to the *Apoe*$^{-/-}$ controls after 4 weeks of WD. Hence, the early activation of the GPR55/LPI axis could represent a protective effect during initial lesion development. It might be interesting to investigate a potential protective effect of LPI administration to WD-fed *Apoe*$^{-/-}$ mice, thereby specifying the role of GPR55/LPI activation. This could have a direct atheroprotective impact. However, the observed results could be a secondary effect of LPI with no affect on GPR55 signaling.

Analysis of more advanced plaques after 16 weeks of WD feeding demonstrated differences in plaque burden between both sexes. It is well described in the literature that the sex of *Apoe*$^{-/-}$ mice considerably impacts atherosclerosis development. Female mice present with more pronounced atherosclerosis development with increased lesion sizes compared to male littermates, despite having similar serum lipid levels[186]. Also, plaque development in the aortic root is generally faster compared to the descending aorta[189]. Analysis of the more rapidly developing plaques in the aortic valve revealed further progressed plaques in female mice compared to males of the same treatment groups. Slower-forming plaques in the descending aorta still showed the same differences in plaque burden after 16 weeks WD feeding as in the 4-week WD aortic root plaque analysis. These results may

reflect a stage-dependent effect of GPR55 in counterbalancing the development of early atherosclerotic lesions.

The cellular composition of atherosclerotic plaques provided additional information on how GPR55 affected atherogenesis. Different histological staining methods were used to quantify macrophages, collagen fibers and the necrotic core in all aortic root plaques. In the early disease stage, macrophages dominated the lesions of *Apoe*$^{-/-}$ *Gpr55*$^{-/-}$ mice. Without the protective effects of GPR55, there is a higher relative macrophage proportion in the plaques. Overall, GPR55 deficiency resulted in more advanced atherosclerotic lesions, implicating an inhibiting effect of GPR55 signaling to atherogenesis.

Assessing functional changes in macrophages due to the loss of GPR55 showed increased uptake of oxLDL *in vitro* compared to control cells. Taken together, these results suggest a role for GPR55 signaling in moderating macrophage localization to atherosclerotic lesions and reducing lesion growth by decreasing oxLDL uptake.

However, Lanuti et al. reported increased intracellular oxLDL accumulation mediated by CD36 and SRBI when treating a human monocytic cell line with GPR55 agonists like O-1602 and LPI[158]. Arguably, pharmacological activation might result in side effects mediated by other receptors also susceptible to these ligands. Additional effects resulting from the *Apoe* deficiency in BMDM used for the experiments in this study cannot be ruled out. In depth research using *in vitro* and *in vivo* techniques with a macrophage-specific depletion of *Gpr55* and a detailed analysis of cholesterol accumulation and efflux will be needed to clarify its role.

6.4 GPR55 is involved in leukocyte recruitment to atherosclerotic lesions

The recruitment of leukocytes to the arterial wall is a key pathophysiological process that enables lesion formation. Montecucco et al. saw increased neutrophil counts and a reduction in collagen content in plaques of GPR55 antagonist-treated mice by using a different approach to evaluate the role of GPR55 in atherogenesis[152]. They treated *Apoe*$^{-/-}$ mice with a GPR55 antagonist while either feeding chow diet or an atherogenic diet for 11 weeks. Pharmacological treatment was limited to 15 injections during the last 3 weeks of diet. They did not observe any differences in lesion size. While our experiments are not exactly comparable, we found higher neutrophil content in aortas in mice lacking GPR55 compared to the control group. Neutrophils play a role in early atherogenesis and these results show the proinflammatory phenotype of *Apoe*$^{-/-}$*Gpr55*$^{-/-}$ mice.

Lee et al. demonstrated a role for GPR55 in monocyte adhesion in an *in vitro* assay using human monocytic cells and a synthetic GPR55 agonist as well as a synthetic antagonist[177]. Increased GPR55 activation led to better adhesion, mediated by an

upregulation of *Mac1* gene expression. Additional *in vivo* data of a small cohort of *Apoe*$^{-/-}$ mice (n = 5-6) receiving a high-fat diet and a GPR55 antagonist treatment presented with a significant reduction in aortic root plaques size compared to feeding high-fat diet alone. Our results also showed significant changes in monocytes and macrophages due to the lack of *Gpr55*. In *Apoe*$^{-/-}$*Gpr55*$^{-/-}$ mice, the relative proportion of intraplaque macrophages was markedly increased after 4 weeks of WD and these animals presented with significantly higher monocyte counts in the bone marrow. Mechanistically, the higher macrophage content in the atherosclerotic lesions could be explained by their enhanced ability to engulf oxLDL, which we observed analyzing BMDM *in vitro*. However, the hypotheses of Lee et al. are dubious. *In vitro* data from a human cell line cannot readily be used to draw conclusions about pathophysiological processes *in vivo*. This experiment should have been at least repeated with isolated murine monocytes to be more transferable. The methodical workup of the atherosclerotic lesions in these mice is relatively superficial and does not conform to the American Heart Association's guidelines for experimental atherosclerosis studies[73]. There is no detailed information on plaque composition, which could be more relevant than lesion size. Also, treatment of the mice with a GPR55 agonist is lacking to understand the effects of the activated GPR55 receptor in this context. We postulate an atheroprotective role of GPR55, particularly during early atherogenesis, where the most substantial impact of the *Gpr55* knockout was observed. Our findings contrast with the postulated atheroprotective role of CID16020046 treatment by Lee et al. Nevertheless, they gather these results at a more advanced stage of atherosclerosis after 24 weeks of lesion development and do not cover the early phase of atherogenesis. Results of our study and the one done by Lee et al. imply a regulatory function of GPR55 on monocytes and macrophages. To evaluate the role of GPR55 in these cells, experiments with a monocyte-specific *Gpr55* knockout will be needed.

6.5 GPR55 modulates innate and adaptive immunity in the context of atherosclerosis

Gpr55 expression was confirmed in leukocyte subsets by qPCR analysis, comparable to data obtained by others[136]. Atherosclerosis is based on an ongoing and nonresolving inflammatory process. This study revealed an increase in inflammation in the aorta of *Apoe*$^{-/-}$*Gpr55*$^{-/-}$ mice. Especially at the beginning of lesion formation, neutrophilia and elevated T cell numbers were observed in aortic tissue. Analysis of aortas after the formation of advanced plaques showed higher expression of cytokines typically released by proinflammatory M1 macrophages. GPR55 seems to attenuate vascular inflammation since knocking out the receptor resulted in a hyper-inflammatory response to the atherogenic diet. The absence of *Gpr55* also increased the number of circulating T cells and T cells in the spleen and paraaortic lymph nodes. Phenotypes and functional properties of T cells deserve further analysis, for example, using cell type-specific deletion of GPR55. Unfortunately,

floxed GPR55 mice are not yet available, which may allow, for example, crossbreeding with T cell specific Cre-recombinase expressing transgenic mice for a more in-depth analysis.

To date, comprehensive data on the role of γδ T cells in atherosclerosis are lacking[55]. We observed increased numbers of γδTCR^{+} T in *Apoe*$^{-/-}$*Gpr55*$^{-/-}$ compared to *Apoe*$^{-/-}$ control mice. Upcoming studies examining the role of γδ T cells in atherosclerosis should include GPR55 signaling in their analysis, as there could be a potential impact.

6.5.1 GPR55 deficiency modifies B cell subsets and antigen production

B cells influence atherosclerosis development depending on specific subsets[68]. While B2 cells are generally considered to facilitate lesion development, B1 cells play an atheroprotective role. Mice depleted in GPR55 presented with more severe atherosclerosis and a shift from splenic FO B2 cells towards MZ B2 cells. Similar modulation of B2 cell subpopulations has been described in atherosclerotic mice before[69]. This effect might be caused by the lack of GPR55 in splenic B cells since there were elevated titers of pro-atherogenic IgG subsets measured in plasma samples of these mice. Subsequent analysis of our group revealed an essential role for GPR55-LPI signaling in the development of immunoglobulin-producing plasma cells. GPR55 depletion resulted in dysfunctional B cells, a dysregulated interaction with T cells and exaggerated antibody production[190].

6.5.2 *Gpr55* knockout did not significantly alter NK cell function *in vitro*

Previous studies illustrated a proinflammatory role for GPR55 in NK cells and monocytes, on which the receptor is highly expressed[135]. We demonstrated *Gpr55* mRNA expression in monocytes and NK cells as well, but in contrast to the results shown by Chiurchiù et al., the mRNA expression was not higher than in cell subsets of the adaptive immune system[135]. *In vitro* experiments with isolated NK cells were carried out to investigate the influence of GPR55 on NK cell activity and cytotoxicity. It was previously suggested that GPR55 might be a stimulatory receptor for NK cells. However, our experiments did not show a reduction in NK cell activity when *Gpr55* was knocked out. Cytotoxicity and NK cell activation were unaltered between the groups. However, the validity of the collected *in vitro* data is limited. The experiments showed a large variability of the data and the LDH release did not increase evenly when raising the ratio of NK cells to target cells. The experiments need to be repeated with a larger amount of specimen and perhaps NK cells should be purified using a method like FACS-sorting. Furthermore, during this ongoing thesis project, it was shown that NK cells do not contribute to lesion development. Hence, the absence of NK GPR55 signaling cannot explain the observed changes in atherogenesis caused by the *Gpr55* knockout, no more experiments were added[53].

6.6 Summary and outlook

GPR55 is involved in a multitude of physiological and pathophysiological processes throughout the whole body. This thesis is the first to elucidate its impact on the development of atherosclerosis in a genetic *Gpr55* knockout mouse model, providing experimental evidence of a substantial role of GPR55 signaling in this disease.

In mice, the GPR55/LPI axis is regulated in experimental hypercholesterolemia and atherogenesis. The influence of GPR55 on the initiation and development of atherosclerotic lesions is most substantial during early atherogenesis. GPR55 also plays a role in metabolic dysregulation as the transcriptional expression of key enzymes involved in lipid metabolism were upregulated in the liver and plasma cholesterol levels and body weight were elevated in mice globally lacking the receptor. However, additional studies will be needed to decipher the role of GPR55 in metabolically relevant cell types, such as hepatocytes and white and brown adipocytes.

In a variety of experiments, *Apoe*$^{-/-}$*Gpr55*$^{-/-}$ mice presented with a more proinflammatory phenotype and more severe atherosclerosis. Hypercholesterolemia-induced activation of GPR55 and downstream signaling during the onset of lesion formation potentially has protective effects on lesion development. The absence of GPR55 resulted in a proinflammatory state compared to control animals. When disease development was examined at a later time point, differences between the genotypes were generally less pronounced.

Early atherosclerotic lesions in mice lacking *Gpr55* presented with increased macrophage content and *in vitro* analyses showed enhanced phagocytic capacity of BMDM when treated with oxLDL. These results could explain why *Apoe*$^{-/-}$*Gpr55*$^{-/-}$ mice had more developed plaques at the onset of atherosclerosis. This advanced state was maintained during disease progression, as lesions from mice with later stage atherosclerosis were more matured with larger necrotic cores and more collagen deposition.

Results presented in this study show that B cell subset distribution and antibody production are severely altered in mice lacking GPR55. Circulating IgG titers were higher in *Apoe*$^{-/-}$*Gpr55*$^{-/-}$ mice and might be partially responsible for their pro-atherogenic phenotype.

In conclusion, the experimental data of this thesis identify a protective role for GPR55 signaling in the context of atherosclerosis in a mouse model. Several important leukocytes involved in atherosclerosis, mainly macrophages, T and B cells, were recognized as possibly directly regulated by GPR55. New studies with cell subset-specific GPR55 knockout models will be required to explore the underlying mechanisms and the possible protective function of pharmacological GPR55 activation. The bioactive lipid receptor GPR55 might be a therapeutic target for atherosclerosis and other inflammatory diseases.

7 REFERENCES

1. World health statistics 2020: monitoring health for the SDGs, sustainable development goals. Geneva: World Health Organization; 2020. Licence: CC BY-NC-SA 3.0 IGO.
2. James, S.L., Abate, D. & Abate, K.H. *et al.* Global, regional, and national incidence, prevalence, and years lived with disability for 354 diseases and injuries for 195 countries and territories, 1990–2017: a systematic analysis for the Global Burden of Disease Study 2017. *The Lancet* **392,** 1789–1858 (2018).
3. Global Burden of Disease Visualisations: Compare. Available at https://www.thelancet.com/lancet/visualisations/gbd-compare (2020).
4. Deaths due to coronary heart diseases in the EU. Available at https://ec.europa.eu/eurostat/web/products-eurostat-news/-/EDN-20200928-1 (2020).
5. Wafa, H.A., Wolfe, C.D.A., Emmett, E., Roth, G.A., Johnson, C.O. & Wang, Y. Burden of Stroke in Europe: Thirty-Year Projections of Incidence, Prevalence, Deaths, and Disability-Adjusted Life Years. *Stroke* **51,** 2418–2427 (2020).
6. Gisterå, A. & Hansson, G.K. The immunology of atherosclerosis. *Nature Reviews Nephrology* **13,** 368–380 (2017).
7. World Health Organization. *Prevention of Cardiovascular Disease. Guidelines for Assessment and Management of Cardiovascular Risk.* (World Health Organization, Geneva, 2007).
8. Piepoli, M.F., Hoes, A.W. & Agewall, S. *et al.* 2016 European Guidelines on cardiovascular disease prevention in clinical practice: The Sixth Joint Task Force of the European Society of Cardiology and Other Societies on Cardiovascular Disease Prevention in Clinical Practice (constituted by representatives of 10 societies and by invited experts) Developed with the special contribution of the European Association for Cardiovascular Prevention & Rehabilitation (EACPR). *European Heart Journal* **37,** 2315–2381 (2016).
9. Ross, R. Atherosclerosis — an inflammatory disease. *The New England Journal of Medicine* **340,** 115–126 (1999).
10. Libby, P., Ridker, P.M. & Hansson, G.K. Progress and challenges in translating the biology of atherosclerosis. *Nature* **473,** 317–325 (2011).
11. Chistiakov, D.A., Orekhov, A.N. & Bobryshev, Y.V. Endothelial Barrier and Its Abnormalities in Cardiovascular Disease. *Frontiers in Physiology* **6,** 365 (2015).
12. Wentzel, J.J., Chatzizisis, Y.S., Gijsen, F.J.H., Giannoglou, G.D., Feldman, C.L. & Stone, P.H. Endothelial shear stress in the evolution of coronary atherosclerotic plaque and vascular remodelling: current understanding and remaining questions. *Cardiovascular Research* **96,** 234–243 (2012).
13. Zhou, J., Li, Y.-S. & Chien, S. Shear stress-initiated signaling and its regulation of endothelial function. *Arteriosclerosis, Thrombosis, and Vascular Biology* **34,** 2191–2198 (2014).

14. Weber, C. & Noels H. Atherosclerosis: current pathogenesis and therapeutic options. *Nature Medicine* **17,** 1410–1422 (2011).
15. Kunjathoor, V.V., Febbraio, M., Podrez, E.A., Moore, K.J., Andersson, L., Koehn, S., Rhee, J.S., Silverstein, R., Hoff, H.F. & Freeman, M.W. Scavenger receptors class A-I/II and CD36 are the principal receptors responsible for the uptake of modified low density lipoprotein leading to lipid loading in macrophages. *The Journal of Biological Chemistry* **277,** 49982–49988 (2002).
16. Bäck, M., Ketelhuth, D.F.J. & Agewall, S. Matrix metalloproteinases in atherothrombosis. *Progress in Cardiovascular Diseases* **52,** 410–428 (2010).
17. Tabas, I. Macrophage death and defective inflammation resolution in atherosclerosis. *Nature Reviews Immunology* **10,** 36–46 (2010).
18. Libby, P. Molecular and cellular mechanisms of the thrombotic complications of atherosclerosis. *Journal of Lipid Research* **50,** S352-S357 (2009).
19. Silvestre-Roig, C., Winther, M.P. de, Weber, C., Daemen, M.J., Lutgens, E. & Soehnlein, O. Atherosclerotic plaque destabilization: mechanisms, models, and therapeutic strategies. *Circulation Research* **114,** 214–226 (2014).
20. Libby, P. The changing landscape of atherosclerosis. *Nature* **592,** 524–533 (2021).
21. Quillard, T., Franck, G., Mawson, T., Folco, E. & Libby, P. Mechanisms of erosion of atherosclerotic plaques. *Current Opinion in Lipidology* **28,** 434–441 (2017).
22. Libby, P. Inflammation in atherosclerosis. *Nature* **420,** 868–874 (2002).
23. Hansson, G.K. Inflammation, atherosclerosis, and coronary artery disease. *The New England Journal of Medicine* **352,** 1685–1695 (2005).
24. Mayadas, T.N., Cullere, X. & Lowell, C.A. The multifaceted functions of neutrophils. *Annual Review of Pathology* **9,** 181–218 (2014).
25. Silvestre-Roig C., Braster Q., Ortega-Gomez A. & Soehnlein O. Neutrophils as regulators of cardiovascular inflammation. *Nature Reviews Cardiology* **17,** 327–340 (2020).
26. Drechsler, M., Megens, R.T.A., van Zandvoort, M., Weber, C. & Soehnlein, O. Hyperlipidemia-triggered neutrophilia promotes early atherosclerosis. *Circulation* **122,** 1837–1845 (2010).
27. Soehnlein, O. Multiple roles for neutrophils in atherosclerosis. *Circulation Research* **110,** 875–888 (2012).
28. Silvestre-Roig, C., Braster, Q. & Wichapong, K. *et al.* Externalized histone H4 orchestrates chronic inflammation by inducing lytic cell death. *Nature* **569,** 236–240 (2019).
29. Moore, K.J., Sheedy, F.J. & Fisher, E.A. Macrophages in atherosclerosis. A dynamic balance. *Nature Reviews Immunology* **13,** 709–721 (2013).
30. Hettinger, J., Richards, D.M., Hansson, J., Barra, M.M., Joschko, A.-C., Krijgsveld, J. & Feuerer, M. Origin of monocytes and macrophages in a committed progenitor. *Nature Immunology* **14,** 821–830 (2013).

31. Robbins, C.S., Chudnovskiy, A. & Rauch, P.J. *et al.* Extramedullary hematopoiesis generates Ly-6C(high) monocytes that infiltrate atherosclerotic lesions. *Circulation* **125,** 364–374 (2012).
32. Mildner, A., Schönheit, J. & Giladi, A. *et al.* Genomic Characterization of Murine Monocytes Reveals C/EBPβ Transcription Factor Dependence of Ly6C- Cells. *Immunity* **46,** 849-862.e7 (2017).
33. Tahir, S. & Steffens, S. Non-classical monocytes in cardiovascular physiology and disease. *American journal of physiology. Cell physiology* (2021).
34. Woollard, K.J. & Geissmann, F. Monocytes in atherosclerosis: subsets and functions. *Nature Reviews Cardiology* **7,** 77–86 (2010).
35. Swirski, F.K., Libby, P., Aikawa, E., Alcaide, P., Luscinskas, F.W., Weissleder, R. & Pittet, M.J. Ly-6Chi monocytes dominate hypercholesterolemia-associated monocytosis and give rise to macrophages in atheromata. *The Journal of Clinical Investigation* **117,** 195–205 (2007).
36. Williams, H., Mack, C.D., Li, S.C.H., Fletcher, J.P. & Medbury, H.J. Nature versus Number: Monocytes in Cardiovascular Disease. *International journal of molecular sciences* **22** (2021).
37. Mestas, J. & Ley, K. Monocyte-endothelial cell interactions in the development of atherosclerosis. *Trends in cardiovascular medicine* **18,** 228–232 (2008).
38. Gerhardt, T. & Ley, K. Monocyte trafficking across the vessel wall. *Cardiovascular Research* **107,** 321–330 (2015).
39. Murray, P.J. & Wynn, T.A. Protective and pathogenic functions of macrophage subsets. *Nature Reviews Immunology* **11,** 723–737 (2011).
40. Tabas, I. & Bornfeldt, K.E. Macrophage Phenotype and Function in Different Stages of Atherosclerosis. *Circulation Research* **118,** 653–667 (2016).
41. Flynn, M.C., Pernes, G., Lee, M.K.S., Nagareddy, P.R. & Murphy, A.J. Monocytes, Macrophages, and Metabolic Disease in Atherosclerosis. *Frontiers in Pharmacology* **10,** 666 (2019).
42. Sinha, S.K., Miikeda, A. & Fouladian, Z. *et al.* Local M-CSF (Macrophage Colony-Stimulating Factor) Expression Regulates Macrophage Proliferation and Apoptosis in Atherosclerosis. *Arteriosclerosis, Thrombosis, and Vascular Biology* **41,** 220–233 (2021).
43. Lin, J.-D., Nishi, H. & Poles, J. *et al.* Single-cell analysis of fate-mapped macrophages reveals heterogeneity, including stem-like properties, during atherosclerosis progression and regression. *JCI insight* **4** (2019).
44. Robbins, C.S., Hilgendorf, I. & Weber, G.F. *et al.* Local proliferation dominates lesional macrophage accumulation in atherosclerosis. *Nature Medicine* **19,** 1166–1172 (2013).
45. Buono, C., Anzinger, J.J., Amar, M. & Kruth, H.S. Fluorescent pegylated nanoparticles demonstrate fluid-phase pinocytosis by macrophages in mouse atherosclerotic lesions. *The Journal of Clinical Investigation* **119,** 1373–1381 (2009).
46. Doran, A.C., Yurdagul, A. & Tabas, I. Efferocytosis in health and disease. *Nature reviews. Immunology* **20,** 254–267 (2020).

47. Gui, T., Shimokado, A., Sun, Y., Akasaka, T. & Muragaki, Y. Diverse roles of macrophages in atherosclerosis: from inflammatory biology to biomarker discovery. *Mediators of inflammation* **2012,** 693083 (2012).
48. Vivier, E., Raulet, D.H., Moretta, A., Caligiuri, M.A., Zitvogel, L., Lanier, L.L., Yokoyama, W.M. & Ugolini, S. Innate or adaptive immunity? The example of natural killer cells. *Science* **331,** 44–49 (2011).
49. Whitman, S.C., Rateri, D.L., Szilvassy, S.J., Yokoyama, W. & Daugherty, A. Depletion of natural killer cell function decreases atherosclerosis in low-density lipoprotein receptor null mice. *Arteriosclerosis, Thrombosis, and Vascular Biology* **24,** 1049–1054 (2004).
50. Bobryshev, Y.V. & Lord, R.S.A. Identification of natural killer cells in human atherosclerotic plaque. *Atherosclerosis* **180,** 423–427 (2005).
51. Selathurai, A., Deswaerte, V., Kanellakis, P., Tipping, P., Toh, B.-H., Bobik, A. & Kyaw, T. Natural killer (NK) cells augment atherosclerosis by cytotoxic-dependent mechanisms. *Cardiovascular Research* **102,** 128–137 (2014).
52. Kyaw, T., Tipping, P., Toh, B.-H. & Bobik, A. Killer cells in atherosclerosis. *European Journal of Pharmacology* **816,** 67–75 (2017).
53. Nour-Eldine, W., Joffre, J. & Zibara, K. *et al.* Genetic Depletion or Hyperresponsiveness of Natural Killer Cells Do Not Affect Atherosclerosis Development. *Circulation Research* **122,** 47–57 (2017).
54. Bruce Alberts, Alexander Johnson, Julian Lewis, Martin Raff, Keith Roberts & Peter Walter. in *Molecular Biology of the Cell. 4th edition,* edited by B. Alberts*, et al.* (Garland Science2002).
55. Saigusa, R., Winkels, H. & Ley, K. T cell subsets and functions in atherosclerosis. *Nature Reviews Cardiology* **17,** 387–401 (2020).
56. Zhou, X., Nicoletti, A., Elhage, R. & Hansson, G.K. Transfer of CD4(+) T cells aggravates atherosclerosis in immunodeficient apolipoprotein E knockout mice. *Circulation* **102,** 2919–2922 (2000).
57. Ketelhuth, D.F.J. & Hansson, G.K. Adaptive Response of T and B Cells in Atherosclerosis. *Circulation Research* **118,** 668–678 (2016).
58. Hansson, G.K. & Hermansson, A. The immune system in atherosclerosis. *Nature Immunology* **12,** 204–212 (2011).
59. Ait-Oufella H., Salomon BL. & Potteaux S. *et al.* Natural regulatory T cells control the development of atherosclerosis in mice. *Nature Medicine* **12,** 178-180 (2006).
60. Kita, T., Yamashita, T., Sasaki, N., Kasahara, K., Sasaki, Y., Yodoi, K., Takeda, M., Nakajima, K. & Hirata, K. Regression of atherosclerosis with anti-CD3 antibody via augmenting a regulatory T-cell response in mice. *Cardiovascular Research* **102,** 107–117 (2014).
61. Tsiantoulas, D., Sage, A.P., Mallat, Z. & Binder, C.J. Targeting B cells in atherosclerosis. Closing the gap from bench to bedside. *Arteriosclerosis, Thrombosis, and Vascular Biology* **35,** 296–302 (2015).
62. Perry, H.M., Bender, T.P. & McNamara, C.A. B cell subsets in atherosclerosis. *Frontiers in Immunology* **3,** 373 (2012).

63. Caligiuri, G., Nicoletti, A., Poirier, B. & Hansson, G.K. Protective immunity against atherosclerosis carried by B cells of hypercholesterolemic mice. *The Journal of Clinical Investigation* **109,** 745–753 (2002).
64. Major, A.S., Fazio, S. & Linton, M.F. B-lymphocyte deficiency increases atherosclerosis in LDL receptor-null mice. *Arteriosclerosis, Thrombosis, and Vascular Biology* **22,** 1892–1898 (2002).
65. Lewis, M.J., Malik, T.H., Ehrenstein, M.R., Boyle, J.J., Botto, M. & Haskard, D.O. Immunoglobulin M is required for protection against atherosclerosis in low-density lipoprotein receptor-deficient mice. *Circulation* **120,** 417–426 (2009).
66. Kyaw, T., Tay, C., Krishnamurthi, S., Kanellakis, P., Agrotis, A., Tipping, P., Bobik, A. & Toh, B.-H. B1a B lymphocytes are atheroprotective by secreting natural IgM that increases IgM deposits and reduces necrotic cores in atherosclerotic lesions. *Circulation Research* **109,** 830–840 (2011).
67. Rosenfeld, S.M., Perry, H.M. & Gonen, A. *et al.* B-1b Cells Secrete Atheroprotective IgM and Attenuate Atherosclerosis. *Circulation Research* **117,** e28-39 (2015).
68. Sage, A.P., Tsiantoulas, D., Binder, C.J. & Mallat, Z. The role of B cells in atherosclerosis. *Nature reviews. Cardiology* **16,** 180–196 (2019).
69. Ma, S.D., Mussbacher, M. & Galkina, E.V. Functional Role of B Cells in Atherosclerosis. *Cells* **10** (2021).
70. Nus, M., Sage, A.P. & Lu, Y. *et al.* Marginal zone B cells control the response of follicular helper T cells to a high-cholesterol diet. *Nature Medicine* **23,** 601–610 (2017).
71. Tay, C., Liu, Y.-H. & Kanellakis, P. *et al.* Follicular B Cells Promote Atherosclerosis via T Cell-Mediated Differentiation Into Plasma Cells and Secreting Pathogenic Immunoglobulin G. *Arteriosclerosis, Thrombosis, and Vascular Biology* **38,** e71-e84 (2018).
72. Hilgendorf, I., Theurl, I. & Gerhardt, L.M. *et al.* Innate Response Activator B Cells Aggravate Atherosclerosis by Stimulating TH1 Adaptive Immunity. *Circulation* **129,** 1677–1687 (2014).
73. Daugherty, A., Tall, A.R., Daemen, M.J.A.P., Falk, E., Fisher, E.A., García-Cardeña, G., Lusis, A.J., Owens, A.P., Rosenfeld, M.E. & Virmani, R. Recommendation on Design, Execution, and Reporting of Animal Atherosclerosis Studies: A Scientific Statement From the American Heart Association. *Arteriosclerosis, Thrombosis, and Vascular Biology* **37,** e131-e157 (2017).
74. Getz, G.S. & Reardon, C.A. Animal models of atherosclerosis. *Arteriosclerosis, Thrombosis, and Vascular Biology* **32,** 1104–1115 (2012).
75. Mahley, R.W. Apolipoprotein E: cholesterol transport protein with expanding role in cell biology. *Science* **240,** 622–630 (1988).
76. Piedrahita, J.A., Zhang, S.H., Hagaman, J.R., Oliver, P.M. & Maeda, N. Generation of mice carrying a mutant apolipoprotein E gene inactivated by

gene targeting in embryonic stem cells. *Proceedings of the National Academy of Sciences of the United States of America* **89,** 4471–4475 (1992).

77. Plump, A.S., Smith, J.D., Hayek, T., Aalto-Setälä, K., Walsh, A., Verstuyft, J.G., Rubin, E.M. & Breslow, J.L. Severe hypercholesterolemia and atherosclerosis in apolipoprotein E-deficient mice created by homologous recombination in ES cells. *Cell* **71,** 343–353 (1992).
78. Nakashima, Y., Plump, A.S., Raines, E.W., Breslow, J.L. & Ross, R. ApoE-deficient mice develop lesions of all phases of atherosclerosis throughout the arterial tree. *Arteriosclerosis and thrombosis : a journal of vascular biology* **14,** 133–140 (1994).
79. Sehayek, E., Shefer, S., Nguyen, L.B., Ono, J.G., Merkel, M. & Breslow, J.L. Apolipoprotein E regulates dietary cholesterol absorption and biliary cholesterol excretion: studies in C57BL/6 apolipoprotein E knockout mice. *Proceedings of the National Academy of Sciences of the United States of America* **97,** 3433–3437 (2000).
80. Baitsch, D., Bock, H.H. & Engel, T. *et al.* Apolipoprotein E induces antiinflammatory phenotype in macrophages. *Arteriosclerosis, Thrombosis, and Vascular Biology* **31,** 1160–1168 (2011).
81. Getz, G.S. & Reardon, C.A. Apoprotein E as a lipid transport and signaling protein in the blood, liver, and artery wall. *Journal of Lipid Research* **50,** S156-S161 (2009).
82. Ishibashi, S., Brown, M.S., Goldstein, J.L., Gerard, R.D., Hammer, R.E. & Herz, J. Hypercholesterolemia in low density lipoprotein receptor knockout mice and its reversal by adenovirus-mediated gene delivery. *The Journal of Clinical Investigation* **92,** 883–893 (1993).
83. Getz, G.S. & Reardon, C.A. Do the Apoe-/- and Ldlr-/- Mice Yield the Same Insight on Atherogenesis? *Arteriosclerosis, Thrombosis, and Vascular Biology* **36,** 1734–1741 (2016).
84. Bentzon, J.F. & Falk, E. Atherosclerotic lesions in mouse and man: is it the same disease? *Current Opinion in Lipidology* **21,** 434–440 (2010).
85. Andrew S. Plump and Jan L. Breslow. Apolipoprotein E and the Apolipoprotein E-Deficient Mouse. *Annual Review of Nutrition* **15,** 495–518 (1995).
86. Emini Veseli, B., Perrotta, P., Meyer, G.R.A. de, Roth, L., van der Donckt, C., Martinet, W. & Meyer, G.R.Y. de. Animal models of atherosclerosis. *European Journal of Pharmacology* **816,** 3–13 (2017).
87. Lagerström, M.C. & Schiöth, H.B. Structural diversity of G protein-coupled receptors and significance for drug discovery. *Nature Reviews Drug Discovery* **7,** 339–357 (2008).
88. Robert Fredriksson, Malin C. Lagerström, Lars-Gustav Lundin, and Helgi B. Schiöth. The G-Protein-Coupled Receptors in the Human Genome Form Five Main Families. Phylogenetic Analysis, Paralogon Groups, and Fingerprints. *Molecular Pharmacology* **63,** 1256–1272 (2003).
89. Berg, J.M., Tymoczko, J.L., Gatto, G.J. & Stryer, L. *Biochemistry* (W.H. Freeman & Company a Macmillan Education Imprint, New York, 2015).

90. Sawzdargo M., Nguyen T., Lee D.K., Lynch K.R., Cheng R., Heng H.H., George S.R., O'Dowd B.F. Identification and cloning of three novel human G protein-coupled receptor genes GPR52, CGPR53 and GPR55: GPR55 is extensively expressed in human brain. *Molecular Brain Research* **64,** 193–198 (1999).
91. National Center for Biotechnology Information, U.S. National Library of Medicine. BLAST: Basic Local Alignment Search Tool. Available at https://blast.ncbi.nlm.nih.gov/ (2020).
92. Baker, D., Pryce, G., Davies, W.L. & Hiley, C.R. In silico patent searching reveals a new cannabinoid receptor. *Trends in pharmacological sciences* **27,** 1–4 (2006).
93. Ryberg, E., Larsson, N., Sjögren, S., Hjorth, S., Hermansson, N.-O., Leonova, J., Elebring, T., Nilsson, K., Drmota, T. and Greasley, P.J. The orphan receptor GPR55 is a novel cannabinoid receptor. *British Journal of Pharmacology* **152,** 1092–1101 (2007).
94. Brown AJ, W.A. *Identification of modulators of GPR55 activity. Assignee: GlaxoSmithKline. Patent WO00186305.* (2001).
95. Drmota E, Greasley P, Groblewski T. *Drmota E, Greasley P, Groblewski T (2004). Screening assays for cannabinoid-ligand type modulators. Assignee AstraZeneca. Patent WO2004074844.* (2004).
96. Petitet, F., Donlan, M. & Michel, A. GPR55 as a new cannabinoid receptor: still a long way to prove it. *Chemical biology & drug design* **67,** 252–253 (2006).
97. Henstridge, C.M., Balenga, N.A.B., Kargl, J., Andradas, C., Brown, A.J., Irving, A., Sanchez, C. & Waldhoer, M. Minireview: recent developments in the physiology and pathology of the lysophosphatidylinositol-sensitive receptor GPR55. *Molecular Endocrinology* **25,** 1835–1848 (2011).
98. Tapio Nevalainen and Andrew J. Irving. GPR55, a Lysophosphatidylinositol Receptor with Cannabinoid Sensitivity? *Current Topics in Medicinal Chemistry* **10,** 799–813 (2010).
99. Keenan, R.W. & Hokin, L.E. The identification of lysophosphatidylinositol and its enzymic conversion to phosphatidylinositol. *Biochimica et Biophysica Acta* **60,** 428–430 (1962).
100. Oka, S., Nakajima, K., Yamashita, A., Kishimoto, S. & Sugiura, T. Identification of GPR55 as a lysophosphatidylinositol receptor. *Biochemical and Biophysical Research Communications* **362,** 928–934 (2007).
101. Kotsikorou, E., Madrigal, K.E. & Hurst, D.P. *et al.* Identification of the GPR55 agonist binding site using a novel set of high-potency GPR55 selective ligands. *Biochemistry* **50,** 5633–5647 (2011).
102. Alhouayek, M., Masquelier, J. & Muccioli, G.G. Lysophosphatidylinositols, from Cell Membrane Constituents to GPR55 Ligands. *Trends in pharmacological sciences* **39,** 586–604 (2018).
103. Aoki, J., Inoue, A., Makide, K., Saiki, N. & Arai, H. Structure and function of extracellular phospholipase A1 belonging to the pancreatic lipase gene family. *Biochimie* **89,** 197–204 (2007).

104. Mariggiò, S., Sebastià, J., Filippi, B.M., Iurisci, C., Volonté, C., Amadio, S., Falco, V. de, Santoro, M. & Corda, D. A novel pathway of cell growth regulation mediated by a PLA2α-derived phosphoinositide metabolite. *The FASEB Journal* **20,** 2567–2569 (2006).
105. Piñeiro, R., Maffucci, T. & Falasca, M. The putative cannabinoid receptor GPR55 defines a novel autocrine loop in cancer cell proliferation. *Oncogene* **30,** 142–152 (2011).
106. Yamashita, A., Oka, S., Tanikawa, T., Hayashi, Y., Nemoto-Sasaki, Y. & Sugiura, T. The actions and metabolism of lysophosphatidylinositol, an endogenous agonist for GPR55. *Prostaglandins & other lipid mediators* **107,** 103–116 (2013).
107. Yamashita, A., Kumazawa, T., Koga, H., Suzuki, N., Oka, S. & Sugiura, T. Generation of lysophosphatidylinositol by DDHD domain containing 1 (DDHD1): Possible involvement of phospholipase D/phosphatidic acid in the activation of DDHD1. *Biochimica et Biophysica Acta* **1801,** 711–720 (2010).
108. Oka, S., Toshida, T., Maruyama, K., Nakajima, K., Yamashita, A. & Sugiura, T. 2-Arachidonoyl-sn-glycero-3-phosphoinositol: a possible natural ligand for GPR55. *The Journal of Biochemistry* **145,** 13–20 (2009).
109. Ueda, H., Kobayashi, T., Kishimoto, M., Tsutsumi, T. & Okuyama, H. EDTA-insensitive deacylation of phosphatidylinositol in porcine platelet membranes. *Life Sciences* **53,** 629–634 (1993).
110. Murase, S. & Okuyama, H. A membrane-bound phospholipase C with an apparent specificity for lysophosphatidylinositol in porcine platelets. *The Journal of Biological Chemistry* **260,** 262–265 (1985).
111. Tsutsumi, T., Kobayashi, T., Ueda, H., Yamauchi, E., Watanabe, S. & Okuyama, H. Lysophosphoinositide-specific phospholipase C in rat brain synaptic plasma membranes. *Neurochemical Research* **19,** 399–406 (1994).
112. Oka, S., Ota, R., Shima, M., Yamashita, A. & Sugiura, T. GPR35 is a novel lysophosphatidic acid receptor. *Biochemical and Biophysical Research Communications* **395,** 232–237 (2010).
113. Aoki, J., Taira, A., Takanezawa, Y., Kishi, Y., Hama, K., Kishimoto, T., Mizuno, K., Saku, K., Taguchi, R. & Arai, H. Serum lysophosphatidic acid is produced through diverse phospholipase pathways. *The Journal of Biological Chemistry* **277,** 48737–48744 (2002).
114. Umezu-Goto, M., Kishi, Y. & Taira, A. *et al.* Autotaxin has lysophospholipase D activity leading to tumor cell growth and motility by lysophosphatidic acid production. *The Journal of Cell Biology* **158,** 227–233 (2002).
115. McMahon, H.T. & Boucrot, E. Membrane curvature at a glance. *Journal of Cell Science* **128,** 1065–1070 (2015).
116. Arifin, S.A. & Falasca, M. Lysophosphatidylinositol Signalling and Metabolic Diseases. *Metabolites* **6,** 6 (2016).
117. Piñeiro, R. & Falasca, M. Lysophosphatidylinositol signalling: new wine from an old bottle. *Biochimica et Biophysica Acta* **1821,** 694–705 (2012).

118. Ailte, I., Lingelem, A.B.D., Kvalvaag, A.S., Kavaliauskiene, S., Brech, A., Koster, G., Dommersnes, P.G., Bergan, J., Skotland, T. & Sandvig, K. Exogenous lysophospholipids with large head groups perturb clathrin-mediated endocytosis. *Traffic* **18,** 176–191 (2017).
119. Bondarenko, A.I., Malli, R. & Graier, W.F. The GPR55 agonist lysophosphatidylinositol directly activates intermediate-conductance Ca2+ -activated K+ channels. *Pflugers Archiv: European Journal of Physiology* **462,** 245–255 (2011).
120. Maingret, F., Patel, A.J., Lesage, F., Lazdunski, M. & Honoré, E. Lysophospholipids open the two-pore domain mechano-gated K(+) channels TREK-1 and TRAAK. *The Journal of Biological Chemistry* **275,** 10128–10133 (2000).
121. Harada, K., Kitaguchi, T., Kamiya, T., Aung, K.H., Nakamura, K., Ohta, K. & Tsuboi, T. Lysophosphatidylinositol-induced activation of the cation channel TRPV2 triggers glucagon-like peptide-1 secretion in enteroendocrine L cells. *The Journal of Biological Chemistry* **292,** 10855–10864 (2017).
122. Andersson, D.A., Nash, M. & Bevan, S. Modulation of the cold-activated channel TRPM8 by lysophospholipids and polyunsaturated fatty acids. *Journal of Neuroscience* **27,** 3347–3355 (2007).
123. Wu, C.-S., Chen, H. & Sun, H. *et al.* GPR55, a G-protein coupled receptor for lysophosphatidylinositol, plays a role in motor coordination. *PloS one* **8,** e60314 (2013).
124. Pietr, M., Kozela, E., Levy, R., Rimmerman, N., Lin, Y.H., Stella, N., Vogel, Z. & Juknat, A. Differential changes in GPR55 during microglial cell activation. *FEBS letters* **583,** 2071–2076 (2009).
125. Lauckner, J.E., Jensen, J.B., Chen, H.-Y., Lu, H.-C., Hille, B. & Mackie, K. GPR55 is a cannabinoid receptor that increases intracellular calcium and inhibits M current. *Proceedings of the National Academy of Sciences of the United States of America* **105,** 2699–2704 (2008).
126. Deliu, E., Sperow, M. & Console-Bram, L. *et al.* The Lysophosphatidylinositol Receptor GPR55 Modulates Pain Perception in the Periaqueductal Gray. *Molecular Pharmacology* **88,** 265–272 (2015).
127. Schicho, R., Bashashati, M. & Bawa, M. *et al.* The atypical cannabinoid O-1602 protects against experimental colitis and inhibits neutrophil recruitment. *Inflammatory Bowel Diseases* **17,** 1651–1664 (2011).
128. Li, K., Fichna, J. & Schicho, R. *et al.* A role for O-1602 and G protein-coupled receptor GPR55 in the control of colonic motility in mice. *Neuropharmacology* **71,** 255–263 (2013).
129. Lin, X.-H., Yuece, B., Li, Y.-Y., Feng, Y.-J., Feng, J.-Y., Yu, L.-Y., Li, K., Li, Y.-N. & Storr, M. A novel CB receptor GPR55 and its ligands are involved in regulation of gut movement in rodents. *Neurogastroenterology & Motility* **23,** 862-e342 (2011).

130. Romero-Zerbo, S.Y., Rafacho, A. & Díaz-Arteaga, A. *et al.* A role for the putative cannabinoid receptor GPR55 in the islets of Langerhans. *Journal of Endocrinology* **211,** 177–185 (2011).
131. Liu, B., Song, S., Ruz-Maldonado, I., Pingitore, A., Huang, G.C., Baker, D., Jones, P.M. & Persaud, S.J. GPR55-dependent stimulation of insulin secretion from isolated mouse and human islets of Langerhans. *Diabetes, Obesity and Metabolism* **18,** 1263–1273 (2016).
132. Moreno-Navarrete, J.M., Catalán, V. & Whyte, L. *et al.* The L-α-lysophosphatidylinositol/GPR55 system and its potential role in human obesity. *Diabetes* **61,** 281–291 (2012).
133. Oka, S., Kimura, S., Toshida, T., Ota, R., Yamashita, A. & Sugiura, T. Lysophosphatidylinositol induces rapid phosphorylation of p38 mitogen-activated protein kinase and activating transcription factor 2 in HEK293 cells expressing GPR55 and IM-9 lymphoblastoid cells. *The Journal of Biochemistry* **147,** 671–678 (2010).
134. Balenga, N.A.B., Aflaki, E., Kargl, J., Platzer, W., Schröder, R., Blättermann, S., Kostenis, E., Brown, A.J., Heinemann, A. & Waldhoer, M. GPR55 regulates cannabinoid 2 receptor-mediated responses in human neutrophils. *Cell Research* **21,** 1452–1469 (2011).
135. Chiurchiu, V., Lanuti, M., Bardi, M. de, Battistini, L. & Maccarrone, M. The differential characterization of GPR55 receptor in human peripheral blood reveals a distinctive expression in monocytes and NK cells and a proinflammatory role in these innate cells. *International Immunology* **27,** 153–160 (2015).
136. Immunological Genome Project. Gene Skyline. Available at http://rstats.immgen.org/Skyline_microarray/skyline.html (2020).
137. Whyte, L.S., Ryberg, E., Sims, N.A., Ridge, S.A., Mackie, K., Greasley, P.J., Ross, R.A. & Rogers, M.J. The putative cannabinoid receptor GPR55 affects osteoclast function in vitro and bone mass in vivo. *Proceedings of the National Academy of Sciences of the United States of America* **106,** 16511–16516 (2009).
138. Waldeck-Weiermair, M., Zoratti, C., Osibow, K., Balenga, N., Goessnitzer, E., Waldhoer, M., Malli, R. & Graier, W.F. Integrin clustering enables anandamide-induced Ca2+ signaling in endothelial cells via GPR55 by protection against CB1-receptor-triggered repression. *Journal of Cell Science* **121,** 1704–1717 (2008).
139. Daly, C.J., Ross, R.A., Whyte, J., Henstridge, C.M., Irving, A.J. & McGrath, J.C. Fluorescent ligand binding reveals heterogeneous distribution of adrenoceptors and 'cannabinoid-like' receptors in small arteries. *British Journal of Pharmacology* **159,** 787–796 (2010).
140. Walsh, S.K., Hector, E.E., Andréasson, A.-C., Jönsson-Rylander, A.-C. & Wainwright, C.L. GPR55 deletion in mice leads to age-related ventricular dysfunction and impaired adrenoceptor-mediated inotropic responses. *PloS one* **9,** e108999 (2014).

141. Yu, J., Deliu, E. & Zhang, X.-Q. *et al.* Differential activation of cultured neonatal cardiomyocytes by plasmalemmal versus intracellular G protein-coupled receptor 55. *The Journal of Biological Chemistry* **288,** 22481–22492 (2013).
142. Andradas, C., Caffarel, M.M., Pérez-Gómez, E., Salazar, M., Lorente, M., Velasco, G., Guzmán, M. & Sánchez, C. The orphan G protein-coupled receptor GPR55 promotes cancer cell proliferation via ERK. *Oncogene* **30,** 245–252 (2011).
143. Ford, L.A., Roelofs, A.J., Anavi-Goffer, S., Mowat, L., Simpson, D.G., Irving, A.J., Rogers, M.J., Rajnicek, A.M. & Ross, R.A. A role for L-alpha-lysophosphatidylinositol and GPR55 in the modulation of migration, orientation and polarization of human breast cancer cells. *British Journal of Pharmacology* **160,** 762–771 (2010).
144. Huang, L., Ramirez, J.C., Frampton, G.A., Golden, L.E., Quinn, M.A., Pae, H.Y., Horvat, D., Liang, L. & DeMorrow, S. Anandamide exerts its antiproliferative actions on cholangiocarcinoma by activation of the GPR55 receptor. *Laboratory Investigation* **91,** 1007–1017 (2011).
145. Henstridge, C.M., Balenga, N.A.B., Ford, L.A., Ross, R.A., Waldhoer, M. & Irving, A.J. The GPR55 ligand L-alpha-lysophosphatidylinositol promotes RhoA-dependent Ca2+ signaling and NFAT activation. *The FASEB Journal* **23,** 183–193 (2009).
146. Kargl, J., Balenga, N.A., Platzer, W., Martini, L., Whistler, J.L. & Waldhoer, M. The GPCR-associated sorting protein 1 regulates ligand-induced down-regulation of GPR55. *British Journal of Pharmacology* **165,** 2611–2619 (2012).
147. Henstridge CM, Balenga NA, Schröder R, Kargl JK, Platzer W, Martini L, Arthur S, Penman J, Whistler JL, Kostenis E, Waldhoer M, Irving AJ. GPR55 ligands promote receptor coupling to multiple signalling pathways. *British Journal of Pharmacology* **160,** 421–422 (2010).
148. Kapur, A., Zhao, P., Sharir, H., Bai, Y., Caron, M.G., Barak, L.S. & Abood, M.E. Atypical responsiveness of the orphan receptor GPR55 to cannabinoid ligands. *The Journal of Biological Chemistry* **284,** 29817–29827 (2009).
149. Staton, P.C., Hatcher, J.P. & Walker, D.J. *et al.* The putative cannabinoid receptor GPR55 plays a role in mechanical hyperalgesia associated with inflammatory and neuropathic pain. *Pain* **139,** 225–236 (2008).
150. Schuelert, N. & McDougall, J.J. The abnormal cannabidiol analogue O-1602 reduces nociception in a rat model of acute arthritis via the putative cannabinoid receptor GPR55. *Neuroscience Letters* **500,** 72–76 (2011).
151. Ishiguro, H., Onaivi, E.S. & Horiuchi, Y. *et al.* Functional polymorphism in the GPR55 gene is associated with anorexia nervosa. *Synapse* **65,** 103–108 (2011).
152. Montecucco, F., Bondarenko, A.I. & Lenglet, S. *et al.* Treatment with the GPR55 antagonist CID16020046 increases neutrophil activation in mouse atherogenesis. *Thrombosis and Haemostasis* **116,** 987–997 (2016).

153. Robertson-Gray, O.J., Walsh, S.K., Ryberg, E., Jönsson-Rylander, A.-C., Lipina, C. & Wainwright, C.L. l-α-Lysophosphatidylinositol (LPI) aggravates myocardial ischemia/reperfusion injury via a GPR55/ROCK-dependent pathway. *Pharmacology Research & Perspectives* **7,** e00487 (2019).
154. Puhl, S.-L., Hilby, M., Kohlhaas, M., Keidel, L.M., Jansen, Y., Hristov, M., Schindler, J., Maack, C. & Steffens, S. Haematopoietic and cardiac GPR55 synchronize post-myocardial infarction remodelling. *Scientific Reports* **11** (2021).
155. McKillop, A.M., Moran, B.M., Abdel-Wahab, Y.H.A. & Flatt, P.R. Evaluation of the insulin releasing and antihyperglycaemic activities of GPR55 lipid agonists using clonal beta-cells, isolated pancreatic islets and mice. *British Journal of Pharmacology* **170,** 978–990 (2013).
156. Meadows, A., Lee, J.H., Wu, C.-S., Wei, Q., Pradhan, G., Yafi, M., Lu, H.-C. & Sun, Y. Deletion of G-protein-coupled receptor 55 promotes obesity by reducing physical activity. *International Journal of Obesity* **40,** 417–424 (2016).
157. Pérez-Gómez, E., Andradas, C., Flores, J.M., Quintanilla, M., Paramio, J.M., Guzmán, M. & Sánchez, C. The orphan receptor GPR55 drives skin carcinogenesis and is upregulated in human squamous cell carcinomas. *Oncogene* **32,** 2534–2542 (2013).
158. Lanuti, M., Talamonti, E., Maccarrone, M. & Chiurchiu, V. Activation of GPR55 Receptors Exacerbates oxLDL-Induced Lipid Accumulation and Inflammatory Responses, while Reducing Cholesterol Efflux from Human Macrophages. *PloS one* **10,** e0126839 (2015).
159. Stančić, A., Jandl, K., Hasenöhrl, C., Reichmann, F., Marsche, G., Schuligoi, R., Heinemann, A., Storr, M. & Schicho, R. The GPR55 antagonist CID16020046 protects against intestinal inflammation. *Neurogastroenterology & Motility* **27,** 1432–1445 (2015).
160. Hayakazu Sumida, Erick Lu, Hsin Chen, Qiyun Yang, Ken Mackie, Jason G. Cyster. GPR55 regulates intraepithelial lymphocyte migration dynamics and susceptibility to intestinal damage. *Science Immunology* **18,** eaao1135 (2017).
161. Metz, S.A. Lysophosphatidylinositol, but not lysophosphatidic acid, stimulates insulin release. *Biochemical and Biophysical Research Communications* **138,** 720–727 (1986).
162. Metz, S.A. Mobilization of cellular Ca2+ by lysophospholipids in rat islets of Langerhans. *Biochimica et Biophysica Acta (BBA) - Molecular Cell Research* **968,** 239–252 (1988).
163. McCloskey, A.G., Miskelly, M.G., Moore, C.B.T., Nesbit, M.A., Christie, K.A., Owolabi, A.I., Flatt, P.R. & McKillop, A.M. CRISPR/Cas9 gene editing demonstrates metabolic importance of GPR55 in the modulation of GIP release and pancreatic beta cell function. *Peptides* **125,** 170251 (2020).
164. Lipina, C., Walsh, S.K., Mitchell, S.E., Speakman, J.R., Wainwright, C.L. & Hundal, H.S. GPR55 deficiency is associated with increased adiposity and impaired insulin signaling in peripheral metabolic tissues. *The FASEB Journal* **33,** 1299–1312 (2019).

165. Imbernon, M., Whyte, L. & Diaz-Arteaga, A. *et al.* Regulation of GPR55 in rat white adipose tissue and serum LPI by nutritional status, gestation, gender and pituitary factors. *Molecular and Cellular Endocrinology* **383,** 159–169 (2014).
166. Schmuhl, E., Ramer, R., Salamon, A., Peters, K. & Hinz, B. Increase of mesenchymal stem cell migration by cannabidiol via activation of p42/44 MAPK. *Biochemical Pharmacology* **87,** 489–501 (2014).
167. Breen, C., Brownjohn, P.W. & Ashton, J.C. The atypical cannabinoid O-1602 increases hind paw sensitisation in the chronic constriction injury model of neuropathic pain. *Neuroscience Letters* **508,** 119–122 (2012).
168. Carey, L.M., Gutierrez, T., Deng, L., Lee, W.-H., Mackie, K. & Hohmann, A.G. Inflammatory and Neuropathic Nociception is Preserved in GPR55 Knockout Mice. *Scientific Reports* **7,** 944 (2017).
169. Gangadharan, V., Selvaraj, D. & Kurejova, M. *et al.* A novel biological role for the phospholipid lysophosphatidylinositol in nociceptive sensitization via activation of diverse G-protein signalling pathways in sensory nerves in vivo. *Pain* **154,** 2801–2812 (2013).
170. McHugh, D., Tanner, C., Mechoulam, R., Pertwee, R.G. & Ross, R.A. Inhibition of human neutrophil chemotaxis by endogenous cannabinoids and phytocannabinoids: evidence for a site distinct from CB1 and CB2. *Molecular Pharmacology* **73,** 441–450 (2008).
171. Cantarella, G., Scollo, M., Lempereur, L., Saccani-Jotti, G., Basile, F. & Bernardini, R. Endocannabinoids inhibit release of nerve growth factor by inflammation-activated mast cells. *Biochemical Pharmacology* **82,** 380–388 (2011).
172. Falasca, M., Iurisci, C., Carvelli, A., Sacchetti, A. & Corda, D. Release of the mitogen lysophosphatidylinositol from H-Ras-transformed fibroblasts; a possible mechanism of autocrine control of cell proliferation. *Oncogene* **16,** 2357–2365 (1998).
173. Falasca, M., Silletta, M.G., Carvelli, A., Di Francesco, A.L., Fusco, A., Ramakrishna, V. & Corda, D. Signalling pathways involved in the mitogenic action of lysophosphatidylinositol. *Oncogene* **10,** 2113–2124 (1995).
174. Falasca, M. & Corda, D. Elevated levels and mitogenic activity of lysophosphatidylinositol in k-ras-transformed epithelial cells. *European Journal of Biochemistry* **221,** 383–389 (1994).
175. Xiao, Y., Chen, Y., Kennedy, A.W., Belinson, J. & Xu, Y. Evaluation of plasma lysophospholipids for diagnostic significance using electrospray ionization mass spectrometry (ESI-MS) analyses. *Annals of the New York Academy of Sciences* **905,** 242–259 (2000).
176. Sutphen, R., Xu, Y. & Wilbanks, G.D. *et al.* Lysophospholipids are potential biomarkers of ovarian cancer. *Cancer Epidemiology, Biomarkers & Prevention* **13,** 1185–1191 (2004).

177. Lee, S.-J. & Im, D.-S. GPR55 Antagonist CID16020046 Protects against Atherosclerosis Development in Mice by Inhibiting Monocyte Adhesion and Mac-1 Expression. *International journal of molecular sciences* **22** (2021).
178. Rinne, P., Guillamat-Prats, R. & Rami, M. *et al.* Palmitoylethanolamide Promotes a Proresolving Macrophage Phenotype and Attenuates Atherosclerotic Plaque Formation. *Arteriosclerosis, Thrombosis, and Vascular Biology* **38,** 2562–2575 (2018).
179. Walsh, S.K., Hepburn, C.Y., Kane, K.A. & Wainwright, C.L. Acute administration of cannabidiol in vivo suppresses ischaemia-induced cardiac arrhythmias and reduces infarct size when given at reperfusion. *British Journal of Pharmacology* **160,** 1234–1242 (2010).
180. Kim, J., Yin, T., Shinozaki, K., Lampe, J.W. & Becker, L.B. Potential of lysophosphatidylinositol as a prognostic indicator of cardiac arrest using a rat model. *Biomarkers* **22,** 755–763 (2017).
181. Kurano, M., Suzuki, A. & Inoue, A. *et al.* Possible involvement of minor lysophospholipids in the increase in plasma lysophosphatidic acid in acute coronary syndrome. *Arteriosclerosis, Thrombosis, and Vascular Biology* **35,** 463–470 (2015).
182. Tomida, M., Yamamoto-Yamaguchi, Y. & Hozumi, M. Purification of a factor inducing differentiation of mouse myeloid leukemic M1 cells from conditioned medium of mouse fibroblast L929 cells. *Journal of Biological Chemistry* **259,** 10978–10982 (1984).
183. Ardolino, M., Azimi, C.S. & Iannello, A. *et al.* Cytokine therapy reverses NK cell anergy in MHC-deficient tumors. *The Journal of Clinical Investigation* **124,** 4781–4794 (2014).
184. Livak, K.J. & Schmittgen, T.D. Analysis of Relative Gene Expression Data Using Real-Time Quantitative PCR and the 2−ΔΔCT Method. *Methods* **25,** 402–408 (2001).
185. Bindila, L. & Lutz, B. Extraction and Simultaneous Quantification of Endocannabinoids and Endocannabinoid-Like Lipids in Biological Tissues. *Methods in molecular biology (Clifton, N.J.)* **1412,** 9–18 (2016).
186. Marek, I., Canu, M., Cordasic, N., Rauh, M., Volkert, G., Fahlbusch, F.B., Rascher, W., Hilgers, K.F., Hartner, A. & Menendez-Castro, C. Sex differences in the development of vascular and renal lesions in mice with a simultaneous deficiency of Apoe and the integrin chain Itga8. *Biology of Sex Differences* **8** (2017).
187. Alter, G., Malenfant, J.M. & Altfeld, M. CD107a as a functional marker for the identification of natural killer cell activity. *Journal of Immunological Methods* **294,** 15–22 (2004).
188. Kang, S., Lee, A.-Y., Park, S.-Y., Liu, K.-H. & Im, D.-S. O-1602 Promotes Hepatic Steatosis through GPR55 and PI3 Kinase/Akt/SREBP-1c Signaling in Mice. *International journal of molecular sciences* **22** (2021).
189. Veillard, N.R., Steffens, S., Burger, F., Pelli, G. & Mach, F. Differential expression patterns of proinflammatory and antiinflammatory mediators during

atherogenesis in mice. *Arteriosclerosis, Thrombosis, and Vascular Biology* **24,** 2339–2344 (2004).

190. Guillamat-Prats, R., Hering, D. & Rami, M. *et al. GPR55 in B cells limits atherosclerosis development and regulates plasma cell maturation* (2021).

8 ACKNOWLEDGEMENTS

Meine Zeit im Labor ist in Windeseile vergangen. Dabei durfte ich viele großartige, inspirierende und liebenswerte Menschen kennenlernen, ohne die diese Dissertation niemals möglich gewesen wäre. Ich möchte mich bei allen bedanken, die mich bei meinen ersten Schritten in der Wissenschaft begleitet und unterstützt haben.

Ich danke Herrn Univ.-Prof. Dr. med. Christian Weber für die Möglichkeit, am Institut für Prophylaxe und Epidemiologie der Kreislaufkrankheiten promovieren und aus der Fülle der Ressourcen, die dieses Institut bereithält, schöpfen zu dürfen.

Ich danke meiner Doktormutter Frau Univ.-Prof. Dr. rer. nat. Sabine Steffens für die exzellente Betreuung und Förderung während der Promotion. Du hast dir stets für Fragen Zeit genommen, und das Projekt immer wieder in neue Richtungen gelenkt. Danke auch für dein Vertrauen, dass du mir so ein wichtiges Thema überlassen hast. Besonders habe ich die äußerst unterstützende Atmosphäre in der Arbeitsgruppe geschätzt. Auch uneindeutige Ergebnisse konnten wir in unseren wöchentlichen Besprechungen diskutieren, einordnen und oft habe ich auf diese Weise neue Impulse bekommen. Natürlich kam der Spaß auch nicht zu kurz. Wir hatten tolle Partys und schöne Ausflüge mit dem ganzen Team. Du hast es mir außerdem ermöglicht, unsere Forschungsergebnisse bei nationalen und internationalen Kongressen vorzustellen. Ohne deine Unterstützung hätte ich nie diese prägenden Erfahrungen machen können.

Dear Raquel, thank you for being the best supervisor a student could wish for! You were a patient teacher and never tired of explaining everything over and over again. We did a lot of exciting experiments, laughed a lot together and I enjoyed working with you every day. Even if we sometimes ran quite late (usually being the last ones still in the lab reading samples at the FACS machine), we always managed to have fun without stress. I won’t forget our parties on the second floor. You always did a great job providing everybody with snacks, beer and good vibes. Thank you for sharing your knowledge. Not only did you teach science, but I learned a lot from you personally. I developed a lot during my time in the lab and you played a big part in it.

Lieber Mario, danke für die unvergesslichen und oft witzigen Momente im Labor und unsere Freundschaft, während wir beide unter Raquels Anleitung Schritt für Schritt die Methodik wissenschaftlichen Arbeitens gelernt haben. Es war sehr beruhigend, dass wir uns manchmal gleichermaßen ungeschickt angestellt haben. Aber letztlich sind die meisten Experimente doch geglückt! Es war eine tolle Zeit! Danke für deine Freundschaft und Unterstützung.

Liebe Martina, deine lebensfrohe und lustige Art hat viel dazu beigetragen, dass ich mich in der AG Steffens vom ersten Tag an wohl gefühlt habe. Danke für die Laborführung bei meiner ersten Vorstellung. Du hast mir sofort das Gefühl gegeben, dass ich in der AG Steffens mit meiner Doktorarbeit gut aufgehoben bin. Zudem hattest du jederzeit ein offenes Ohr für mich und wertvolle Ratschläge, wenn es mal

nicht nach Plan lief. Ich möchte mich auch für deine unermüdliche Hilfe bei den vielen Mouse-Harvests bedanken. Auf dich war einfach immer Verlass!

Liebe Sarah, vielen Dank, dass du mich unter deine Fittiche genommen hast, als ich auf den ersten Kongressen meine Arbeit vorstellen durfte. Ich erinnere mich noch sehr lebhaft an unsere nie enden wollende Odyssee nach Rostock-Warnemünde an dem Tag, als Air Berlin nicht mehr flog und ein Orkan über Norddeutschland fegte. Deine ganzen Tipps und Ratschläge und die vielen netten Gespräche werden mir besonders in Erinnerung bleiben.

Lieber Michi, ohne dich hätte ich meine Promotion in der AG Steffens niemals angefangen. Danke, dass du mir den Kontakt ermöglicht hast und mich am Anfang in das Team integriert hast.

Danke Yvonne für deine tolle Unterstützung bei den ganzen Aorta-Präparationen, deine unermüdliche Geduld und die vielen Kniffe rund um die Histologie.

Ich möchte mich auch bei Sascha, Cornelia, Philipp, Amin, Mariaelvy, Donato und allen anderen Mitarbeitern am IPEK bedanken. Es hat mich sehr gefreut, euch kennengelernt zu haben und bin dankbar, dass ihr mich bei meinem „Abenteuer Doktorarbeit“ begleitet habt.

Ganz besonders möchte ich meinen Eltern danken, die mich immer bedingungslos bei allen Vorhaben unterstützen. Ihr habt mich stets ermutigt, mich jeder Herausforderung zu stellen, und mich dabei bestärkt, meinen Weg zu finden. Danke für eure aufmunternden und motivierenden Worte während der ganzen letzten Jahre. Ich möchte mich auch bei Laura bedanken. Danke, dass du mich mit viel Verständnis und Geduld über die Monate der Manuskripterstellung aufgebaut hast und für mich da warst.